

DEVELOPMENT OF TEMPERATURE AND
FLOW SENSORS FOR MICROFLUIDIC
APPLICATIONS

DEVELOPMENT OF TEMPERATURE AND
FLOW SENSORS FOR MICROFLUIDIC
APPLICATIONS

By

Simon Loane, B.A. BAI

A Thesis

Submitted to the School of Graduate Studies

in Partial Fulfillment of the Requirements

for the Degree

Master of Applied Science

McMaster University

© Copyright by Simon Loane, July 2009

MASTER OF APPLIED SCIENCE (2009)
(Department of Mechanical Engineering)

McMaster University
Hamilton, Ontario, Canada

TITLE: The Development of Microfluidic Temperature and Flow Sensors

AUTHOR: Simon Loane, B.A. BAI (Trinity College, Dublin)

SUPERVISOR: Dr. C.Y. Ching, Dr. Ravi Selvananagathy

NUMBER OF PAGES: xvi, 155

Abstract

There is currently a lack of quality sensing techniques that can provide the required spatial and temporal resolution for use in microfluidic devices. The development of such micro sensors will allow real time monitoring and control of many processes at the micro level, and play a crucial role in expanding microfluidics to novel applications. For example, integration of sensors within the microfluidic device itself will allow active control of processes within these devices. The overall objective of this study was to develop a micro temperature and micro flow sensor for use in microfluidic devices. The specific objectives were to develop, design and micro fabricate a micro thermocouple and micro heater, and integrate these within a microchannel to show proof of concept of a micro thermal pulse flow sensor. A platinum-constantan (PT-NiCu) micro thermocouple was developed and fabricated using a three mask process. The microfabrication protocols and procedures were developed for potentiostatically electroplating the constantan leg of the micro thermocouple. The thermocouples were characterized and the Seebeck coefficient (sensitivity) was found to be $39.04 \mu\text{V}/^\circ\text{C}$ and $41.75 \mu\text{V}/^\circ\text{C}$ for non compensated and a compensated thermocouple arrangement respectively.

A meandering resistive type micro heater was developed. The power consumption for the 400 \AA thick gold micro heaters on the silicon oxide and on the glass substrates was compared. The power required for the glass substrate was 46mW , 112mW and 160mW for 5V , 8V , 10V respectively, while for the silicon oxide was 499.5 mW , 1.27 W and 1.943 W respectively.

The thermal flow sensor was developed by integrating the micro heater and micro thermocouple within a microchannel to show proof of concept of the sensor. The flow sensor was operated in three modes; time of flight, temperature difference and pulsed thermotransfer calibration mode.

Essentially the thermotransfer principle occurs as the heat loss from the micro heater source to the fluid will increase with the flow rate, thereby giving greater voltage amplitude of the thermocouple response with increasing flow velocities.

The flow sensor performance was characterized using methanol/water as the working fluid for mass flow rate in the range of no flow to 0.7 ml/min. The device has several unique operating and physical characteristics, including the novel pulsing scheme developed that compensates against temperature drift, resulting in high repeatability.

The flow sensor was calibrated using the thermotransfer principle for three pulse modes; single, multiple pulses with change in input voltage and multiple pulses with change in pulse duration.

The comparative results showed that the multiple pulse modes generated a more detectable signal than the single pulse mode. The multiple pulse regimes allowed for a larger dynamic flow range. The flow sensor can be duplicated relatively easily so that multiple sensors can be distributed within a microfluidic device to allow simultaneous flow measurements at different locations within the device.

Acknowledgements

I would like to express my appreciation to my co supervisors Dr. Chan Ching and Dr Ravi Selvananagathy for their guidance, encouragement and support, not only as my supervisor in graduate school, but throughout my time in Canada and while I was writing my thesis abroad. They contributed much time in the development of this project, their knowledge and advice have helped me develop both academically and as an individual. Their diligent supervision has made my time as a masters student a truly enjoyable experience.

I would like to thank the CEDT for affording me the opportunity to work with its excellent facilities. In particular I would like to thank Doris Stevanovic, Zhilin Peng and Graham Pearson for their training and advice concerning the micro machining process within the clean room. I would like to thank Steve Koprach, for his help with SEM and EDS analysis.

Special acknowledgment to the technicians of the mechanical engineering department, Joe Verhaeghe, Ron Lodewyks, Jim McLaren, Mark McKenzie and JP Talon for their advice, assistance and technical support that was extended throughout my time at McMaster.

I would also like to thank both TRML and CAMEF research group for their many discussions and insights concerning my project. The support and friendship of these groups has meant a great deal to me over the past years.

I would particularly like to thank Youseff Ziada who has always come to my aid and acted as my sounding board, helped me many times to get over the final hurdle, you are truly a friend.

I am grateful to my friends and family for supporting me, their involvement has enhanced the quality of the time spent at McMaster University, making it both socially and academically

rewarding. I am particularly grateful to my mother and father for not only financially supporting my academic endeavors, but encouragement, understanding and for being my editor in chief. None of this would have been possible without the loving support, inspiration and motivation of my wife Leticia. Yes sweetheart its finally done and I thank you ;)

Table of Contents

Chapter 1: Introduction	1
1.1 Introduction.....	1
1.2 Research Objectives.....	3
1.2.1 Micro Thermocouple.....	4
1.2.2 Micro Heater.....	4
1.2.3 Micro Flow Sensor.....	4
1.3 Scope and Organisation of this Work.....	4
Chapter 2: Micro Thermocouples	7
2.1 Introduction.....	7
2.2 Fundamentals & Governing Equations.....	12
2.2.1 Empirical ‘Laws’ of Thermocouples.....	14
2.2.2 Transient Temperature Measurement.....	15
2.2.3 Thermocouples Noise.....	16
2.3 Literature Review.....	17
2.4 Materials.....	20
2.5 Electroplating.....	21
2.5.1 Constantan Alloy.....	30
2.6 Secondary Junctions and Lead Wire Attachment.....	41
2.7 Thermocouple Fabrication.....	43
2.8 Thermocouple Experimental Setup.....	45
2.8.1 Effect of Seed Layer on the Underlining Micro Thermocouple.....	48

2.9	Micro Thermocouple Results.....	51
2.10	Summary.....	56
Chapter 3:	Micro Heaters.....	57
3.1	Introduction.....	58
3.2	Fundamentals and Governing Equations.....	59
3.3	Literature Review.....	60
3.4	Materials.....	63
3.5	Microfabrication Process.....	64
3.6	Experimental Setup.....	66
3.7	Micro Heater Characterization.....	68
3.8	Summary.....	71
Chapter 4:	Micro Flow Sensor.....	72
4.1	Introduction.....	72
4.1.1	Flow Sensor Design.....	77
4.2	Literature Review.....	78
4.2.1	Thermal Flow Sensors.....	78
4.2.2	Electrochemical Flow Sensors.....	87
4.2.3	Other Techniques.....	88
4.3	Fundamentals and Governing Equations.....	88
4.3.1	Modes of Operation.....	96
4.3.2	Time of Flight.....	96

4.3.3	Pulsed Thermotransfer Calibration.....	98
4.4	Materials and Working Fluid.....	100
4.4.1	Working Fluid.....	100
4.5	Microfabrication Process.....	103
4.5.1	Fabrication Process.....	103
4.5.2	Fabrication of Micro Channel.....	106
4.5.3	System Integration.....	107
4.6	Experimental Setup.....	108
4.6.1	Signal Conditioning.....	110
4.7	Experimental Results.....	114
4.7.1	Introduction.....	114
4.7.2	Low Duty Cycle.....	115
4.7.3	Time of Flight.....	115
4.7.4	Single Pulse Operating Mode.....	118
4.7.5	Change in Pulse Width Operation Mode.....	124
4.7.6	Change in Pulse Amplitude Operation Mode.....	128
4.7.7	Temperature Drift.....	132
4.7.8	Advantages.....	133
4.8	Summary.....	134
Chapter 5:	Conclusions and Future Work.....	135
5.1	Introduction.....	135

5.2	Overview and Conclusions.....	135
5.3	Recommendation.....	138
	Reference.....	140
	Appendix A – Manufacturing Process.....	148
	Appendix B –RTD Calibration Curve.....	153
	Appendix C – Design Masks.....	154
	Appendix D – Labview Programs.....	155

List of Figures

Figure 2-1: Classification scheme of contacting thermal sensors.....	11
Figure 2-2: Basic thermocouple temperature/X diagram, and equivalent electrical circuit.....	11
Figure 2-3: Schematic of basic electroplating cell.....	29
Figure 2-4: Polarization curves for copper (M_2) and nickel (M_1) alloy deposition.....	29
Figure 2-5: Electroplated potentiostatically setup in a three electrode cell,.....	34
Figure 2-6: Experimental setup.....	34
Figure 2-7: I-t curves of different potentials of - 0.8, -1, -1.2 and - 1.4 V's Ag/AgCl.....	37
Figure 2-8: EDS results the percentage nickel v's deposition voltage.....	37
Figure 2-9: a) SEM picture of typical constantan thin film, b.) Non-homogenous film caused due hydrogen evolution.....	40
Figure 2-10: Picture of the leads attached with the silver conductive epoxy paste.....	40
Figure 2-11: Process flow of micro thermocouple.....	40
Figure 2-12: (a) First mould of positive photoresist (b) Constantan electroplated.....	47
Figure 2-13: Completed fabricated micro thermocouple.....	47
Figure 2-14: Schematic of characterization of micro thermocouples.....	47
Figure 2-15: Picture of the test section used in calibration micro thermocouples.....	50
Figure 2-16: Calibration curve for micro thermocouples consisting of 16.31% Ni & 83.69 % Cu. The lower curve represents when an ice bath was used and has a slope of 39.04 $\mu\text{V}/^\circ\text{C}$.	

The upper curve is where the no compensation was used and has a slope of 41.75 $\mu\text{V}/^\circ\text{C}$	50
Figure 2-17: Plot represents the consistence between different thermocouples in devices.....	51
Figure 2-18: Plots of the Johnson noise with temperature for the three different thermocouples.....	51
Figure 3-1: Heater fabrication process flow.....	65
Figure 3-2: Micro heater.....	65
Figure 3-3: Calibration curve of resistance surface temperature of the heater.....	67
Figure 3-4: Micro heater maximum temperature verse electrical power input.....	67
Figure 4-1: Classification scheme of physical principles of flow sensors.....	74
Figure 4-2: The three signal domains and signal transport of a thermal flow sensor.....	74
Figure 4-3: Conceptual schematic of a thermal micro pulse film flow sensor.....	80
Figure 4-4: The first macro thermal flow meter proposed by C.C Thomas in 1911.....	80
Figure 4-5: Boundary layer for micro channel where the fluidic boundary layer is fully developed and the thermal boundary layer is developing after the heater.....	92
Figure 4-6: a.) Thermal boundary layer with distance from the heater is reducing with increase flow rate, b.) Nusselt number with distance from the heater, the Nusselt number is increasing with flow rate.....	92
Figure 4-7: Schematic of time of flight sensor, thermal pulse introduced, and detected downstream by two sensors.....	99

Figure 4-8: Schematic of thermotransfer calibration technique, thermal pulse introduced, and detected downstream, where the amplitude of the responses are correlated with mass flow rate.....	99
Figure 4-9: Molecular structure of FC 70.....	99
Figure 4-10: Fabrication process flow for the integrated micro pulse film.....	105
Figure 4-11: Completed fabricated pulse film flow measurement device on SiO ₂ substrate.....	105
Figure 4-12: Su-8 100 PDMS microchannel fabrication and integration on the time of flight sensor.....	112
Figure 4-13: Schematic of characterization of micro flow sensor.....	112
Figure 4-14: Typical voltage signal for the input of the micro heater, for 5, 8, & 10 Volts..	113
Figure 4-15: Measured voltages for mass flow rate of 0.3 ml/min, a) is single pulse operation at 10 V, b) is multiple pulse operation with changing amplitude 5,8 and 10V. c) is multiple pulse operation with changing pulse times 50, 100, and 150 ms.....	113
Figure 4-16: T-type thermocouple embedded at the top of the micro channel, its minimal junction size has limited effect on the flow.....	117
Figure 4-17: Shift of response curve to determine time of flight information. Single pulse regime, with input 10 V, for velocities of 3.33×10^{-2} m/s, 5.56×10^{-2} m/s and 7.78×10^{-2} m/s.....	117
Figure 4-18: The effect of pulse detection with change in flow rates, for an input pulse of 10 V with a duty cycle of 2.5%, period 4 seconds.....	120
Figure 4-19: Correlation curves for the single pulse mode of the signal amplitude to velocity for different input powers.....	120
Figure 4-20: Signal response of thermocouple with different voltage inputs, for a flow rate of 0.1 ml/min and duty cycle of 2.5%, period of 4 seconds.....	122

Figure 4-21: Correlation curves for near and far thermocouples for single pulse operation with a 10 V input.....122

Figure 4-22: Is the response of the thermocouple to change in pulse width of 50, 100 and 150 ms for a 10 V input at flow rate of 0.5 ml/min.....127

Figure 4-23: The difference in voltage amplitude for change pulse widths with time between pulses a.) thermocouple located 0.5 mm from micro heater, b.) thermocouple located 1.5 mm.....127

Figure 4-24: Correlation of velocity with slopes of thermocouple response for change in pulse width 50, 100, and 150 ms.....127

Figure 4-25: Response of the thermocouple to change in pulse amplitude 5V, 8V and 10V at flow rate of 0.5 ml/min.....130

Figure 4-26: The difference in pulse amplitude (5, 8 & 10 V) with time between pulses a.) thermocouple located 0.5 mm from micro heater, b.) Thermocouple located 1.5 mm.....130

Figure 4-27: Calibration of mass flow rate with slopes of thermocouple response for change in pulse width 50, 100, and 150 ms.....131

Figure 4-28: Plots of voltage response highlighting the effect of temperature drift for flow rate of 0.5 ml/min, period 4, seconds duty cycle 25%, a.) Single pulse 10 V input b.) Pulse width 10 V 0.5s, 1s and 1.5s c.) Change in amplitude 5 V, 8V and 10V.....131

List of Tables

Table 1: Relative performance of common electrical micro sensors.....	10
Table 2: Thermoelectric EMF and Seebeck coefficient of various metals at 200 °C relative to platinum at 0 °C.....	14
Table 3: Standard reduction electrode potentials.....	24
Table 4: Electroplating receipt.....	33
Table 5: Thermal conductivity and thickness of materials used for 1-d thermal resistance model.....	60
Table 6: Overview of experimental and modeling of micro flow sensors.....	83
Table 7: The ratio of time taken for heat pulse to be detected due to effect of convection only, to the time taken for the heat to diffuse through the substrate to reach sensor at known distance downstream for a silicon substrate.....	95
Table 8: The ratio of time taken for heat pulse to be detected due to effect of convection only, to the time taken for the heat to diffuse through the substrate to reach sensor at known distance downstream for a silicon substrate.....	96
Table 9: Physical properties of different fluids under standard ambient temperature and pressure conditions.....	102

Chapter 1: Introduction

1.1 Introduction

Modern developments in the design and utilization of microfluidic devices have found many applications, ranging from the life sciences for pharmaceuticals and biomedicine (drug design, delivery and detection, diagnostic devices) to industrial applications of combinatorial synthesis (rapid chemical analyses and high throughput screening) and in micro electronics cooling.

For example, in the micro electronics applications, the increase in miniaturization with high density transistor formations has resulted in a significantly greater heat flux generated by these devices. Such heat flux densities cannot be handled with current conventional cooling methods and are the limiting factor that prevents rapid advances in the microelectronics sector. Innovative micro fabricated liquid based micro-scale cooling technologies have been developed to overcome these thermal problems [1]. These devices take advantage of their fast response time, small length scales and can selectively address localized areas with greater control. In micro electronics, small areas of very high temperature occur periodically, known as hot spots. By integrating micro sensors into these devices, active control can be achieved in cooling these hotspots quickly and efficiently which will make heat removal of these devices more efficient and with lower power consumption. The integration of micro sensors within these devices will give crucial information, allowing more flexible thermal management solutions.

The absence of quality micro sensing techniques that provide the necessary spatial and temporal (continuous data feedback) resolution at critical paths and positions in many microfluidic devices has been the main difficulty in achieving real-time monitoring of many processes [1]. Information gathered with micro sensors allows fast response manipulations that increase the efficiency and performance of the overall device with minimal disturbance to the devices. The three main micro sensors that are currently being developed are for temperature, flow and pressure. This study focussed on developing a temperature and flow sensor at the microscale.

Micro temperature sensors can be categorized into two groups:

- I. Electrical (e.g. Thermocouples, Thermistors).
- II. Non-Electrical (e.g. SAW, fiber optics, Infrared, Temperature sensitive fluorescents).

In this study a micro thermocouple was chosen because it can achieve high spatial resolution, microfabricated relatively inexpensively and is more durable than resistance thermometers (due to their fabricated structure). Micro thermocouples have several advantages: (i) they can be extremely small in size, (ii) have a fast time response, (iii) integrate with minimal disturbance, (iv) are capable of highly precise temperature measurements and (v) are self generating (no not require a external power source).

Flow measurement at the microscale is particularly difficult due to diversity of medium, condition and performance criteria, and the fact that it is not a scalar quantity. However, there is a need for precise micro flow measurement and control. Existing commercial

sensors are inadequate because of their large size and difficulties in integrating with microfluidic devices. Micro flow sensors can be categorized into eight different groups:

- I. Mechanical (e.g. Volume, Force)
- II. Nuclear Physics (e.g. Nuclear Resonance, Isotope Injection)
- III. Optics (e.g. Laser Anemometry, μ PIV)
- IV. Electrodynamics (e.g. Induction, Conduction)
- V. Hydrodynamics (e.g. Thrust, Pressure Difference)
- VI. Thermodynamics (e.g. Heat Conduction and Convection)
- VII. Acoustics (e.g. Doppler Effect, Time of Flight)
- VIII. Stochastic (e.g. Correlations)

The focus of the micro flow measurement was to research and develop a reliable flow sensor with a novel correlation technique. A micro thermal pulse film flow sensor was chosen because of its applicability to microfluidic applications, in particular for operation in both harsh micro electronics and temperature sensitive biological environments. The micro pulse film flow sensor has several advantages, as it can be fabricated using standard microfabrication techniques and can measure a wide range of flow rates, with minimal disturbance to the flow.

1.2 Research Objectives

The overall goal of the research was to develop, manufacture and characterize micro sensor devices that could measure temperature and flow. The specific objectives are:

1.2.1 Micro Thermocouple

To develop an array of micro thermocouples that can be used to monitor temperature information. The micro thermocouples were designed, fabricated and characterized in this study. The micro thermocouples were fabricated using an electroplating process with junction sizes in the range 50 μm to 500 μm . The junction resolution lower limit was restricted by resolution of printed masks.

1.2.2 Micro Heater

To develop a micro heater that would provide sufficient heat in a short duration of time to cause a localized change in the fluid temperature. A micro heater was designed, fabricated and characterized. The power to the micro heater and the corresponding increase in local temperature was characterized.

1.2.3 Micro Flow Sensor

To develop a micro thermal pulse film prototype flow sensor. The feasibility of the device was determined and the performance characterized. The effects of novel thermal pulse patterns were investigated and the data reduction algorithms to measure the flow rate developed.

1.3 Scope and Organisation of This Work

This thesis consists of five chapters, including this introductory chapter. The work is primarily intended to be a building block for developing future generations of micro sensors, and in situ measurements in micro fluidic devices.

The three main chapters of the thesis are:

Chapter 2 – Micro Thermocouples

Chapter 3 – Micro Heaters

Chapter 4 – Micro Flow Sensor

Fundamentals of thermal measurements and the basic governing equations are presented in Chapter 2. This chapter also includes an overview of the literature pertaining to micro thermocouples. Design consideration, fabrication process and novel fabrication techniques relating to micro thermocouple are presented. Fundamentals of electroplating and characterization results of the electroplated alloy are included. A summary of the experimental setup to characterize the thermocouples is presented. The experimental results for the thermocouples are presented and discussed. Finally, the effect of signal to noise is investigated.

Chapter 3 presents the design considerations and fabrication process of the micro heater. An overview of the literature related to resistance micro heaters is presented. The experimental results for the micro heater are presented and discussed. The power input requirements for detection of the heat pulse are evaluated.

Chapter 4 presents the fundamentals of flow sensing and its governing principles for application at the micro-scale. The experimental setup is introduced and the limitations of the system are discussed. The experimental results are presented, with the novel pulse schemes used in this study.

Finally, chapter 5 provides an overview and conclusions from this work. Key experimental findings of the current investigation are summarized, and recommendations for future studies are presented.

Chapter 2. Micro Thermocouples

2.1 Introduction

There is a need to develop reliable techniques that will measure and control temperature in microfluidic devices. If the thermal data can be acquired continuously it has the capacity to reduce in operating costs with faster response times and improved quality control in many microfluidic devices. Proper effective spatial and temporal resolution of temperature sensors in many micro- processes, such as micro coolers and micro reactors, is required to achieve real time monitoring and control of these processes.

In micro electronics, small areas of very high temperature occur periodically, known as hot spots. By integrating micro sensors into these devices, active control can be achieved in cooling these hotspots quickly and efficiently, that will make heat removal of these devices more efficient and with lower power consumption.

Thermal sensing methods are classified into two broad categories: namely (i) contacting and (ii) non-contacting. In thermal contacting sensors there is physical contact between the heat source and sensor, and the energy transfer to the sensor is by conduction. In thermal non-contacting sensors, there is no physical interaction between the sensor and heat source, and the sensors operate by means of radiation [1]. For contact thermal temperature sensors, the heat source generates a thermal signal that is detected by the sensor that either generates or modulates an electrical signal. Figure 2-1 shows a classification scheme for the family of contacting thermal sensors. Thermal contacting

heat sensors can be subsequently divided into either electrically or non electrically operated. Electrical thermal sensors either operate by the principle of modulation or self generation. A modulating sensor requires an input signal that is used to generate the electrical power of the output signal. Self generating sensors do not require an external power source. All but two of the electrical based thermal sensors are modulating rather than self generating. The two self generating sensors in this scheme are thermocouples and noise sensors. Noise sensor technique compares the thermal noise of a reference resistor with the unknown noise of the measurement resistor. They require extensive post hardware, software and were considered unsuitable there was a high possibility of interference in measurements when operated in a micro electronics environment. Thermocouples are based on the Seebeck effect, where an electromotive force (EMF) is generated across a junction between two different metals that are held at different temperatures.

All other thermal electrical sensors require external power source. Other non contact methods, include infrared which is limited to measuring surface temperatures (all objects emitting electromagnetic radiation), liquid crystal imaging based on the optical properties of the material, indicators are temperature sensitive materials that are added to the surface/fluid that change colour with changes in temperature and finally temperature sensitive fluorescents (e.g. Rhodamine B).

Table 1 compares some of the most common micro thermal sensors. Thermistors are small, thermally dependent semiconducting resistors. They have a high degree of sensitivity, however this sensitivity is non linear and may vary within a batch of samples,

due to the fabrication process. Therefore thermistors require individual calibration that is not very simple. The resistance temperature device (RTD) operates on the principle that a conductive material resistance changes as a function of its temperature. They are highly accurate and have a linear output over a wide temperature range; however, they are relatively large and can be easily damaged. A thermistor works on the same principle as a RTD and is cheaper; however, it is not as accurate and has a non linear output.

Micro thermocouples were chosen for this study because they can achieve high spatial resolution (50 - 500 μ m junction sizes), and they can be micro fabricated inexpensively and more durably than resistance thermometers. They have no offset and need not be biased. Thin film thermocouples (TFTCs) have several advantages over conventional bulk temperature sensors as they are extremely small in size with fast response times (3 ms [3]), have minimal disturbance characteristics and are capable of highly precise temperature measurements (as can be located directly at the point of measurement). When combined in an array TFTCs can measure temperature at multiple locations over an area with an extremely high spatial resolution. In this study, micro thermocouples are developed that can be used in a range of applications.

Table 1: Relative performance of common electrical micro sensors, (adapted from [1]).

Type	Range [°C]	Resolution [°C]	Response Times [s]	Output	Sensitivity [$\mu\text{V}/^\circ\text{C}$]	Device	Comments
Thermocouple (T-type)	-160 to 370	± 0.3	0.005	Approx. Linear, Difference	~ 50	Thin Foil	Rapid response foil construction.
Thermopile (T-type)	0 to 70	± 0.2	<1	Linear, Difference	40	Micro	Research very stable
Noise	-200 to 100	± 1	<1	Non- Linear, Absolute	~ 0.01	Resistor	Difficult to use, low sensitivity. Electrical circuit must be well designed
Platinum Resistance Temperature	200 to 1000	± 2	$1/\Delta f$	Linear, Absolute	$0.4 \Omega/^\circ\text{C}$ @100 Ω	Wire wound	Commercially standard, stable and precise
Thermistor	-270 to 450	± 0.1	~ 1	Non- Linear, Absolute	Variable as NTC,PTC	Mini bead	Commercially lower cost the PRT, but non linear
Spreading resistor	-50 to 150	$\pm 3\%$	5	\sim Linear, Absolute	$7 \Omega/\text{K}$ @1k Ω	Silicon	Cheap general purpose sensor of moderate accuracy.
Thermodiodes	-50 to 200	± 1	10	Linear, Absolute	-2mV/K	Silicon	Cheap general purpose sensor of moderate accuracy. Thermistors better characteristics (+TCT)
Thermotransistor	-50 to 200	± 1	10	Linear, Absolute	$1 \mu\text{A}/\text{K}$ @300 μA	Silicon	Low cost with integrated IC are good general purpose sensors

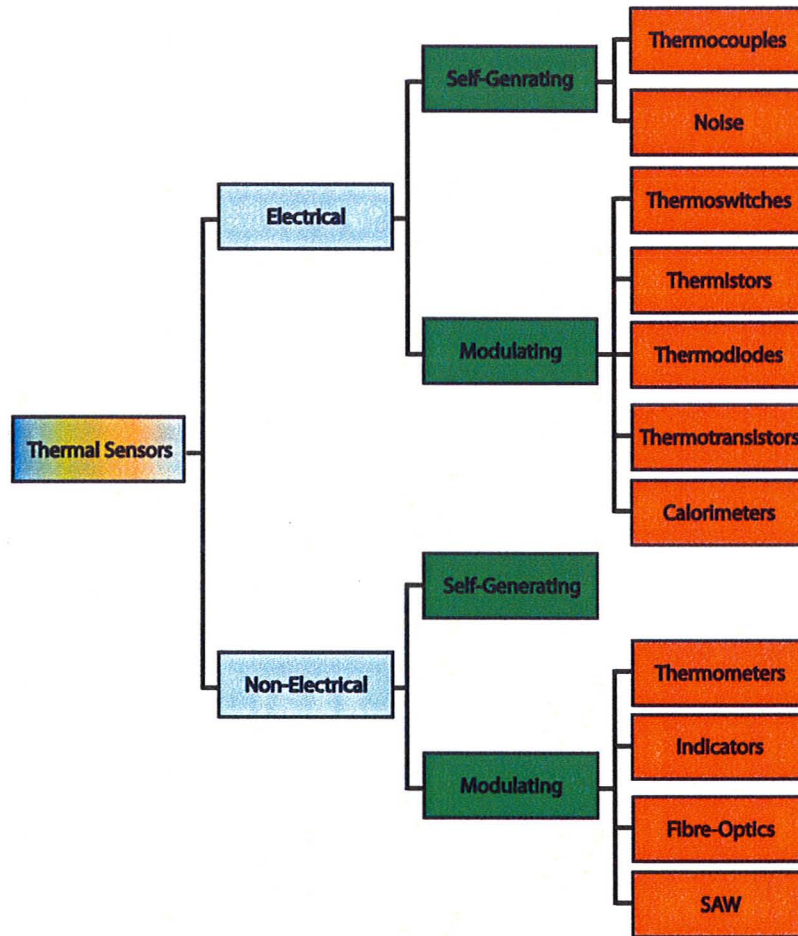


Figure 2-1: Classification scheme of contacting thermal sensors, (adapted from [1]).

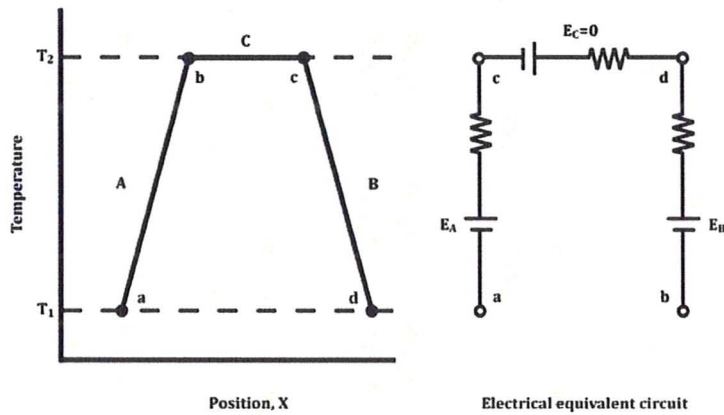


Figure 2-2: Basic thermocouple Temperature/X diagram, and Equivalent Electrical circuit, (adapted from [3]).

The objective here was to develop an electroplated micro scale thermocouple, micro fabricate the same and then document the corresponding microfabrication techniques. The following section describes the literature review of existing research in the field developed in the past with an emphasis on micro thermocouples. The fundamental physics of thermocouple phenomena and their governing equations, the materials, the fabrication methods, and characterization results are presented.

2.2 Fundamentals and Governing Equations

There are three major effects involved in thermoelectric thermometry: the Seebeck, Peltier and Thomson effects.

Thomas Johann Seebeck discovered that dissimilar conductors that form a closed circuit and are exposed to a temperature gradient will generate a net thermal electromotive force that induces a continuous electric current.

In the case of two dissimilar conductors A and B that are joined together at a hot point T_2 and with a temperature difference ΔT maintained between the hot point T_2 and the cold junction T_1 , an open circuit voltage ΔV is developed between the leads at the cold point (see Figure 2-2). This is known as the Seebeck effect and it can be expressed as [3]

$$\Delta V_\alpha = \alpha \Delta T \quad 2-1$$

where α is the Seebeck coefficient $\left[\frac{\mu\text{V}}{\text{K}} \right]$. For a practical working thermocouple the electro-thermal force is proportional to the product of the temperature difference and the Seebeck coefficient difference [3].

$$\Delta E_a = (\alpha_1 - \alpha_2)(T_2 - T_1) \quad 2-2$$

where α_1 and α_2 denotes the Seebeck coefficients of materials 1 and 2, respectively. The voltage produced is independent of both the size/shape of the junction or surrounding circuit.

A reference temperature T_1 (Ice Bath or cold junction compensation) is required as it is only possible to measure the temperature difference using thermocouples. Table presents some standard Seebeck coefficients for common metals with reference to Platinum at 0°C .

The EMF expressed in terms of the Fermi energy E_F and the diffusion potential q can be expressed as the Seebeck coefficient, which is a bulk property [5].

$$\phi = \frac{E_F}{q} = \alpha \Delta T \quad 2-3$$

$\frac{E_F}{q} = \phi$ is the electrochemical potential and q is the electron charge. The Fermi level of metals is temperature dependent. Thus the Fermi level difference will be lower at the hot junction such that the electrons will flow towards it causing a positive Seebeck coefficient. However a diffusion potential will develop which will oppose the EMF from

the change in Fermi level. Therefore there will be no gradient electrical potential unless a temperature gradient exists.

Table 2: Thermoelectric EMF and Seebeck coefficients of various metals at 200 °C relative to platinum at 0°C [1].

Element	ΔV_r (mV)	α ($\mu V/K$)
Chromium	+3.38	16.8
Gold	+1.84	9.20
Copper	+1.83	9.15
Platinum	0.00	0.00
Constantan	-7.45	-37.25

2.2.1 Empirical ‘Laws’ of Thermocouples

In order to get accurate repeatable measurements the following three empirical laws governing thermocouples need to be considered:

The ‘Law’ of Homogeneous Materials [3]:

‘A thermoelectric current cannot be sustained in a circuit of a single homogeneous material, however varying in cross-section, by the application of heat alone.’

The 'Law' of Intermediate Materials [3]:

'The algebraic sum of the thermoelectromotive forces in a circuit composed of any number of dissimilar materials is zero if all the circuit is at a uniform temperature.'

The 'Law' of Successive or Intermediate Temperatures [3]:

'If two dissimilar homogeneous metals produce a thermal emf of E_1 , when the junctions are at temperatures T_1 and T_2 , and a thermal emf of E_2 , when the junctions are at T_2 and T_3 , the EMF generated when the junctions are at T_1 and T_3 will be $E_1 + E_2$.'

The first law implies that there must be at least two different metals to create an EMF, and any EMF generated for a single metal is due to the non uniformities in the material. The second law implies that if a third homogenous metal C is added between the metals A or B, once the junction temperature remains the same, the net EMF of the circuit will remain the same. This holds true once there is good thermal and electrical contact between the different metals. The third law states that a thermocouple calibrated with a known reference temperature can be used at any other reference temperature once there is a known linear correlation.

2.2.2 Transient Temperature Measurements

Use of micro thermocouples is an effective method to measure temperature changes in a transient environment due to their ability to respond quickly (~3ms) [1]. A thermocouple has finite mass and therefore finite heat capacity, and consequently cannot respond instantaneously to temperature changes. Assuming a first order lumped system, the energy equation for the thermocouple sensor can be represented as [1]

$$\rho V c_p \frac{d\theta}{dt} = hA\theta \quad 2-4$$

where c_p is the specific heat, θ the difference of temperature between the thermocouple and ambient, h is heat transfer coefficient due to convection and A is the surface area of the thermocouple junction. Solving the equation, the time constant for a thermocouple can be obtained as [1]

$$\tau = \frac{\rho V c_p}{hA} \quad 2-5$$

For a short response time the thermocouple should be designed to have as large a surface area as possible while minimizing its volume.

2.2.3 Thermocouple Noise

The primary consideration determining the performance of a thermocouple is the signal to noise ratio. At the heart of the signal there is a fundamental noise generated due to actual temperature fluctuations and due to electrical interference, the limit of which is the sensitivity of the thermocouple. This most basic source of noise arises from the thermal energy, kT of the system. This source of noise is referred to as Johnson noise, after J.B.

Johnson who first noted it. It can be approximated as white noise. The average noise power, \bar{P}_f [W] for a resistance R [Ω] is [3],

$$\bar{P}_f = \frac{\overline{V_f^2}}{4R} = kT\Delta f \quad 2-6$$

where Δf is the difference in bandwidth of the signal between f and $f + \Delta f$ [Hz], $\overline{V_f^2}$ is the mean square of the fluctuating potential, k is the Boltzmann constant [J/K], R is the resistance of the conductor and T [K] is the absolute temperature of the conductor.

Assuming that R and T are constant over the bandwidth Δf , the Root Mean Square (RMS) value of the voltage of thermal noise for a thermocouple is [3]

$$V_f = \sqrt{4kTR\Delta f} \quad 2-7$$

with usual units of nV/Hz

2.3 Literature Review

Previous research on micro thermocouples mainly focused on temporal measurement of temperature in electronics and in harsh environments. Generally their fabrication techniques were sputter or electron beam deposition of metals for the two different component legs of the micro thermocouple. Initially micro thermocouples were deposited on the tip of cantilevers of an atomic force (AFM) and scanning tunnelling microscopes (STM). The AFM and STM used thermocouples to scan the surface of non conductive surfaces [4]. The majority of the heat transfer between the tip and the surface was through conduction through the gas and not through direct contact of the surface. Shi, L. et al. [5]

developed a multi layer process consisting of sputter and wet etching with buffered hydrofluoric acid to create cantilever tips for AFM probes. The main drawback of the AFM and STM methods is the effect of the measurement probe on its surroundings. The thermocouple tends to draw heat away from the sample affecting the true measurement, and additionally this will disturb the fluid flow.

Park et al. [6] designed a multiple array of 10 X 10 thermocouples in a 9mm X 9mm area, using aluminium nitride (AlN) to reduce the thickness of the intermediate layers so that a sensor thickness of 0.15 μm could be achieved. This dense multiple array with high spatial resolution was designed for measurements where there is a high temperature gradient over a small area in applications such as electronic cooling surfaces. The thermocouples had an equivalent Seebeck coefficient of 17.6 $\mu\text{V/K}$.

Jang, S. P. et al. [7] developed a thermal sensor array consisting of 25 T-type (Copper-Constantan) micro thermocouples sputtered on the end of a heat sink in an area 5X5 mm using stainless steel masks. They used the thermocouple to measure the surface temperature of the heat sink and subsequently were able to determine flow rate in a microchannel using the heat sink thermal resistance. Gualous, H. et al. [8] investigated an array of 16 thin film thermocouples with a junction area of 8 X 8 μm . The thermocouple consisted of gold and palladium layers and had a response time in the order of 140 μs .

Thermoelectric properties of electroplated CuNi alloy were investigated by Delatorre, R. G. et al. [9]. They constructed a thermocouple with a junction consisting of CuNi alloy

and silicon. They found Seebeck coefficients as high as $-43\mu\text{V}/^\circ\text{C}$ for a junction size of $400\mu\text{m}$. An identical electroplating solution was used in this research.

Cygan, A. [10] designed an array of T type micro thermocouples consisting of electroplated post layers that would improve thermal insulation where the junction of the thermocouple was electroplated on top. Modelling found that posts of $3\mu\text{m}$ were optimum; however, it was not possible to fabricate an actual working prototype due to the complexity of the multi-layered electroplating fabrication process.

Chu, D et al. [11] examined the effect of the Seebeck coefficient with reductions of junction size. Their thermocouples consisted of gold and nickel elements and was fabricated on a 1 micron oxide film on silicon wafer. They observed that down to a thickness size of 100nm , the Seebeck coefficients did not experience any significant changes. However after this point there was a notable reduction in Seebeck coefficient with an increase in noise level. They observed a change in Seebeck coefficients with a variation of the thermocouple ratio of the element thicknesses. They explained that as the thin film gets thinner, the resistivity increases and the cross-section area decreases, therefore increasing Johnson noise levels.

An investigation into thin film thermocouples embedded into metals was examined by Zhang, X. et al. [12]. Similarly to Chu, D et al. [11] they found that a reduced film thickness resulted in faster response times; however, there was significant reduction in thermal sensitivity. The main difficulty in embedding thin film thermocouples in metal substrates is that there must be dielectric materials in order to provide electrical insulation

for the sensing unit. They used a combination of Alumina (Al_2O_3) and silicon nitride (Si_3N_4) in order to insulate materials from the substrate. This combination was chosen in order to cover potential pinholes in the alumina film and to minimize thermal stresses. They sputter deposited chromel and alumel as the thermocouple elements. In the manufacture of their standard K type thermocouple they used thin layers of Titanium (Ti) in order to get good adhesion between electrical insulators and the thermocouple elements. They achieved a thermal sensitivity of $40.6 \mu\text{V}/^\circ\text{C}$, which is comparable to the sensitivity of the macro standard K-type thermocouples. They did not observe any changes in Seebeck coefficients due to the thin layers of Ti used for adhesion.

2.4 Materials

The materials for the sensor substrate and sensor were selected based on their thermal and electrical properties and feasibility for microfabrication. A flat smooth glass or silicon with a 9000 \AA layer of oxide was chosen as the substrate material because of its capacity to electrically insulate and isolate the metal thermal sensor.

Electroplating was the preferred method for fabrication of the thermocouple both due to its low cost as well as the range of composition that can be obtained by tuning the deposition potential. Gold was selected for the thermocouple electroplating base because of its high resistance to electrochemical corrosion and oxidation which is crucial for electroplating. Since gold does not adhere to the glass substrate, a chromium layer is deposited as a seed layer for the gold deposition. Constantan was selected for one leg of the thermocouple. The reason for its selection was its high Seebeck coefficient relative to

other metals. It has a unique position for a metal or alloy as it has a negative Seebeck coefficient. The implication here is that when forming a junction with another metal or alloy it will show higher sensitivity relative to alternative alloys if such were chosen to partner that metal or alloy. Further properties of constantan are discussed in detail later in subsection 2.5.

Platinum was metal deposited as the second leg of the thermocouple. It was chosen due to the fact that all Seebeck coefficients of materials are always referenced to Platinum because it is a pure metal with a low Seebeck coefficient. The advantage is that even though secondary junctions will occur, the secondary junction effect is known and can be compensated from thermocouple reference tables, see Table 2.

2.5 Electroplating

Electrodeposition is a convenient and inexpensive way of depositing thin films on conductive substrates without damaging the substrates [13]. It is extensively used in industry due to its high quality of deposits, high production rates, few size and shape limitations and low initial capital investment. It has several advantages over sputtering vacuum deposition processes because it can have high deposition rates at low temperature, with the possibility of tailoring the crystallographic texture and composition of the deposits.

A typical electroplating cell setup generally consists of an electrically conductive and chemically inert anode (Platinum), cathode (conductive wafer that is to be plated), and an aqueous salt solution (metals to be plated), as shown in Figure 2-3. The substrate to be

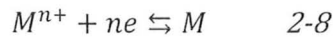
plated is initially patterned using a lithography process to create a mould for plating with junction sizes in the range 50 μm to 500 μm , (see Figure 2-12). The thermocouple substrate is then maintained at a negative potential relative to the anode. The aqueous salt solution contains reducible forms of ions of the desired metals. The positively charged cations migrate towards the negatively biased substrate where they are reduced, and deposited in the catholyte region (immediately surrounding the cathode of the solution), at the exposed conductive surface.

There are three fundamental stages in cathodic deposition of alloys:

1. Ionic Migration: occurs when the ions move in the direction of the cathode under the presence of applied potential, diffusion and/or convection, see Figure 2-3.
2. Electron transfer: occurs when the hydrated ion molecules align with the presence of the field on entering the diffusion double layer. As the metal ions enter the fixed double layer their hydrated shell is lost due to higher field potential. As these ions reach the cathode surface they become individually neutralized and absorbed onto the surface.
3. Incorporation: occurs when atoms are absorbed at the growth point on the cathode and combined with the growing lattice.

Detailed discussion of these mechanisms and their theoretical significance can be found in Pleith, W. [14].

When a platinum anode is immersed in an aqueous salt solution containing ions of the desired metal of deposition M^{n+} there will be an exchange of metal ions between the two phases, the metal and the solution. [14]



where n is the number of electrons involved in the reaction. The governing equation for the cathode potential, while deposition is occurring, is the Nernst Equation [15], and is the function of the activity of metal ions in the solution ($M^{n+} \equiv \frac{a_M^{n+}}{a_M}$) [15].

$$E = E^o + \left(\frac{RT}{n\mathfrak{F}}\right) \ln \frac{a_M^{n+}}{a_M} + P \quad 2-9$$

where E^o is the standard electrode potential of the metal, \mathfrak{F} is the Faraday constant (96487 Cmol⁻¹), R is the gas constant (8.314472 J/K mol), T is the absolute temperature in Kelvin, a_M^{n+} is the activity of the metal ion of the reactants, a_M is the activity of the metal ion of the products, n is the valence change of ions, (nickel $n=0,1,2,3$. Copper = 1,2),

The first term is the standard reduction potential for a given metal, the second accounts for the thermodynamic concentration of the metal ions, and the final term P is polarization. Polarisation occurs when there is a deviation of the cell potential from the equilibrium value when a Faradic current is applied. Potential is measured by the overpotential (η), see equation 2-11. The standard reduction potential of the electroplating solution under investigation is presented in Table 3. The reduction

potentials are referenced against a standard hydrogen reference electrode (SHE) at a temperature of 25°C and atmospheric pressure.

Table 3: Standard Reduction Electrode Potentials [15]

Electrochemical Reductions	Electrode Reaction	Standard Value (V) Versus SHE
Oxygen (Acid solutions)	$O_{2(g)} + 4e^- + 4H_{(aq)}^+ \leftrightarrow 2H_2O_{(l)}$	1.23
Oxygen (Basic solutions)	$O_{2(aq)} + 4e^- + 2H_2O_{(aq)} \leftrightarrow 4OH_{(aq)}^-$	0.401
Cu/Cu ²⁺	$Cu^{2+} + 2e^- \leftrightarrow Cu$	0.340
H ₂	$2H^+ + 2e^- \leftrightarrow H_2$	0
Ni/Ni ²⁺	$Ni^{2+} + 2e^- \leftrightarrow Ni$	-0.236
Hydrogen evolution	$2H_2O + 2e^- \rightarrow H_{2(g)} + 2OH^-$	-0.83

Overpotential (η) occurs when there is a difference between the equilibrium potential of the electrode E and the potential of the same electrode as a result of current flowing through it, $E(I)$,

$$\eta = E(I) - E \quad 2-10$$

This overpotential is the sum of different overpotential η terms due to different reaction steps.

$$\eta = \eta_{mt} + \eta_{ct} + \eta_{rxn} \quad 2-11$$

where η_{mt} is mass transfer overpotential (concentration polarization), η_{ct} is the charge transfer overpotential (activation polarization), and η_{rxn} is the reaction overpotential (reaction polarization). For large negative overpotential ($\eta \geq 100\text{mV}$) the total current density (i) increases exponentially with overpotential (η):

$$i = -i_o e^{-\alpha \frac{n\zeta\eta}{RT}} - i_o e^{(1-\alpha) \frac{n\zeta\eta}{RT}} \quad 2-12$$

where i_o is the exchange current density ($\eta = 0, i = i_o$), α is the transfer coefficient. This expression for the total current density is known as the Butler-Volmer equation and describes the electrode kinetics. The first term is associated with overpotential occurring forward reaction (in this case cathode), while the second term is associated with the overpotential reverse reaction (in this case anode). Equation 2-12 is an exponential relation, showing that for small changes in overpotential there will be large changes in current density. The logarithm of Equation 2-13 results in the Tafel equation, which can be used to model the electrode kinetics. [15]

$$\eta = a \pm b \log|i| \quad 2-13$$

where $a = \frac{2.303RT}{\alpha n\zeta} \log i_o$ and $b = \frac{2.303RT}{\alpha n\zeta}$ are constants and $|i|$ is the absolute value of the current density. The sign holds for anodic and cathodic processes respectively. The charge transfer coefficient α can be derived from slopes of the Tafel lines and the exchange current density i_o can be determined from an extrapolation to the Nernst potential when $E = E_o$.

Electrodeposited alloys have applications in decorative purposes, protective coatings (marine installations) or application where specific properties are required, such as better physical properties that include corrosion resistance and magnetic properties. Essentially, co-depositing of two metals does not differ from that of depositing of a single metal, nonetheless, finding the correct conditions for depositing is not a straightforward process. Two conditions must exist for alloy electroplating to occur [16];

1. One of the metals must be capable of being independently deposited (Copper) before the other metals are co deposited.
2. The deposition potentials must be fairly close (within 50 mV [16]) together.

Deposition of a given metal is dependent on the Nernst Equation, (Equation 2-9), which is made up of two main terms. The first of these is the standard electrode potential E^o of the metal in question. The other term is a function of the ions activity values, which in turn is proportional to the ionic concentration. For two cathode processes to occur simultaneously, for instance for Copper and Nickel to be deposited at the same site, then the specific potential equation 2-9 becomes;

$$E_{Cu} = E_{Ni} \quad 2-14$$

$$E_{Cu} = E_{Cu}^o + \left(\frac{RT}{n\mathfrak{F}}\right) \ln a_{Cu} + P_{Cu} \approx E_{Ni} = E_{Ni}^o + \left(\frac{RT}{n\mathfrak{F}}\right) \ln a_{Ni} + P_{Ni} \quad 2-15$$

This equation Nernst equations for copper and nickel - implies that for co deposition to occur either;

- The individual standard potentials E_{Ni}^o must be about equal to E_{Cu}^o so that minor adjustments in the bulk concentrations of the metals will make E_{Ni} and E_{Cu} equal. This is not the case in this particular study, as the standard potentials of both Copper and Nickel are far apart (0.5 V).
- The standard electrode potentials differ by a large amount, such that the E_{Cu}^o cannot approximate to being equal to E_{Ni}^o . Thereby the value of the activity is controlled by changing the respective concentrations. This mechanism is the method of choice used in this study.
- Alternatively when the reduction potential is far apart, and large adjustment in the activities is not possible, the polarizations of P_{Cu} and P_{Ni} must be far enough apart to equalize the dynamic deposition potentials. However it is to be noted that high polarization values will result in two phase alloys [15].

As metals with higher potentials reduce preferentially (copper), they often prohibit the deposition of lower potential metals (nickel). Therefore the choice of the potential must be selected very carefully in order that the lower potential metal can be deposited simultaneously without use of excessive current density.

Figure 2-4 depicts a typical deposition voltage plot versus current density for two different individual metals. The partial polarization curves of two metals, M1 and M2, that are contained in the bath, their combined polarization curve and hydrogen evolution, which occur at higher negative overpotential that decreases efficiency, are presented. The curves are made up of three regions. Initially the reactions are thermodynamic controlled,

followed by an upward sloping kinetically controlled region and finally by a mass transport controlled region. In the thermodynamically controlled region, the standard potential is modified by thermodynamic solution factors, which is theoretically represented by the second term in equation 2-9. The electrons tend to move to their lowest energy state possible. Applying a current increases their activity (second term of Nernst equation 2-9), and allows reactions that would not normally occur to happen as the electrons can now move to their preferred energy level. The kinetic regions are where reactions are governed by the Butler-Volmer equation (Equation 2-12). In this region the current rises exponentially with an increase in overpotential. At low currents the surface concentration of ions is approximately that of the bulk concentration. At higher currents, the deposition rate is faster, and the ions cannot be replaced quickly enough, leading to the onset of the final region where mass transport is dominant. Here the current is large enough that species are fully reacting but the deposition rate remains constant. This is known as the limiting current. Even though the deposition rates remain constant the potential can be increased. However, when the limiting current is achieved, the current increases the amount of hydrogen evolution and not the species deposition. In Figure 2-4 co-deposition will occur at a potential V_1 with a ratio of $M1:M2$ in relation to I_1/I_2 . Alternatively, for a potential of V_2 a different ratio of $M1:M2$ of the alloy will be deposited which is related to I_3/I_4 . This demonstrates how an alloy can deposit two metals at one potential and how the composition percentage of the alloys can be determined.

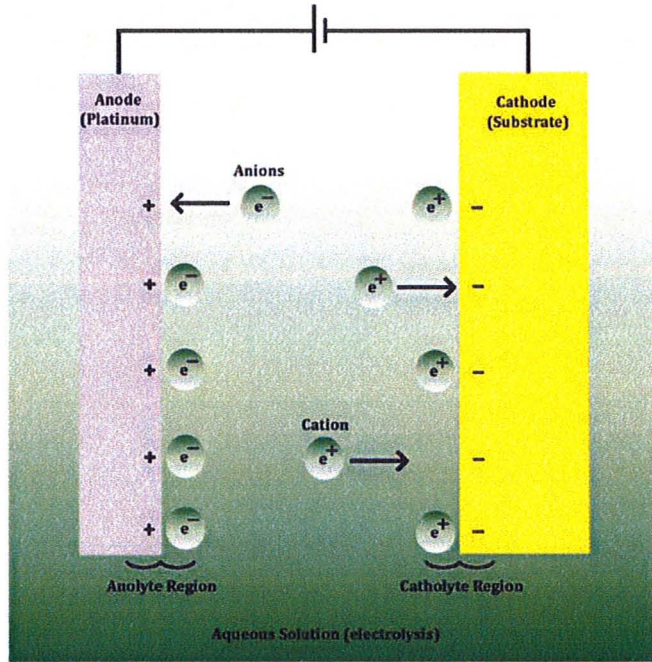


Figure 2-3: Schematic of basic electroplating cell

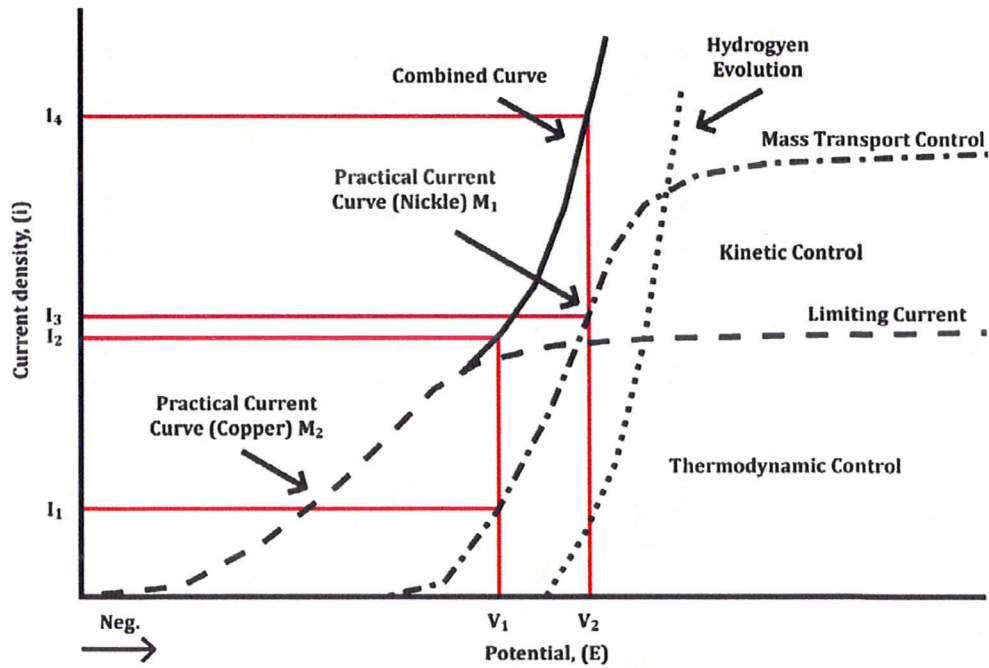


Figure 2-4: Polarization curves for Copper (M_2) and Nickel (M_1) Alloy deposition. (adapted from [10,15]).

2.5.1 Constantan Alloy

Constantan (NiCu) alloys have been electroplated due to its decorative use as long back as 1912 [17]. They have good corrosion resistance, catalytic, mechanical and electrical properties. Nickel-Copper alloys were selected for this study because of their high Seebeck coefficient relative to other metals and demonstrated linear output voltage curve over a wide operating temperature range (0-1250 °C). The linear output voltage is a particularly useful attribute when considering ease of calibration, determination of the certainty of individual measurements and consistence between devices. NiCu alloy is in an unique position among metals and metal alloys as it has a negative Seebeck coefficient. When combined with other metals to make a thermocouple junction, it will provide a larger Seebeck coefficient difference and hence a larger sensitivity. This is the primary reason why they are used in traditional k-type and t-type thermocouples. Different compositions of NiCu alloys will result in different Seebeck coefficients. With increasing nickel compositions the sensitivity of NiCu alloys increase until reaching a maximum at approximately 55%, after which there is a reduction in sensitivity again [3]. Alloys that are over 30% copper rich are highly corrosion resistant in acidic and alkaline media and in many oxidising and reducing gas environments. These properties are particularly good for micro thermocouples in microfluidic applications, as they will not tarnish or add harmful contaminants and not affect any biological samples.

Another advantageous attribute of CuNi alloy is that it is a catalytic material for a wide variety of processes. In electrochemical processes it is a mechanism for small molecule

transformations (H_2 , methanol, glucose) [18]. This has many applications in biosensor (glucose), fuel cells (dehydrogenation reaction from alcohol) and even environmental problems (nitrates etc.). These properties allow the possibility of the thermocouple to act with a dual application (taking temperature measurements, while at the same time acting as a catalyst). Foremost it is capable of making the appropriate measurement. In addition it could operate in a closed loop format (i.e. current passing through) that would permit it to act as a catalyst in certain applications. Also Nickel-Copper alloys have greater tensile strength than pure nickel [15]. Hardness values of alloys can be controlled very precisely as the grain size increases with nickel composition.

The characteristics of electroplated thin layers depend on the process, such as electrolyte composition, temperature, agitation, pH, the applied potential and the current density.

The standard reduction potential of copper (+0.34 V) and nickel (-0.25 V) versus the standard hydrogen reference electrode (SHE) are far apart, (see Table 3 for relative standard potentials of processes). Under normal deposition conditions of Copper and Nickel, equilibrium is never attained and the deposition potentials are always more negative than that of the standard potentials due to polarization (corollary of Faraday's Law). Therefore a complexing agent is required to bring the discharge potential of the two species closer together to co-deposit both metals from an electrolytic bath. Various complexants such as citrate, pyrophosphate, ammonia, and cyanide have been examined [19].

In this study both citrate and acetate complexing agents were considered. Partial current densities of copper and nickel are reduced by adding citrates to solution, however by different amounts. Complexing citrates cause the reduction of the concentration of Cu^+ ions by several orders and therefore the concentration ratio of Ni^+ ions to Cu^+ is increased. Rode, S. et al. [20] investigated the complexing chemistry for Copper-Nickel alloys from citrate baths. They examined the co-deposition models for similar electroplating solution; however, their solution had higher concentration of both copper sulphate, and tri-sodium citrates, leading to lower deposition of Nickel composition for relative negative potentials.

Rode, S. et al. [20] found that for a bath with pH 6 solution, all the Nickel ions are complex to NiCit^- . There were no Ni ions and no copper nickel complexes. The copper ions formed a dominant copper complex as $\text{CuCit}_2\text{H}_2^{4-}$. Complex metal ions, the concentration or activity of the ions in solution and the reversible electrode potential are calculated using the stability constant of the complex determined by Rode, S. et al [20]. Citrate baths produce good quality deposits with stress free Ni rich alloys possessed of a high current efficiency. Their low toxicity, stability of solution, and the fact that they can act as brightening, levelling, buffer agent removes the requirement for additional additive agents into the solution.

In this work, CuNi alloy was electroplated to fabricate one leg of the thermocouples. The electroplating solution used for this study is presented in Table 4.

Table 4: Electroplating recipe [13]

Material	Nickel Sulfate	Copper Sulfate	Citric Acid Trisodium Salt
Chemical Composition	NiSO ₄	CuSO ₄	C ₆ H ₅ Na ₃ O ₇
Quantity [mol/L]	0.171	0.019	0.19

The plating bath was prepared from analytical grade chemicals and de-ionised water with resistivity of 18.2MΩcm. The electrodeposition was carried out potentiostatically (-1.16V) in a three electrode cell, as shown in Figure 2-5. The voltage was adjusted to maintain a desired current density, between the wafer and the Silver-Silver Chloride (Ag/Ag-Cl) reference electrode (that was placed close to the cathode), compensating for changing impedances of the electrodes during plating to maintain a more constant current density.

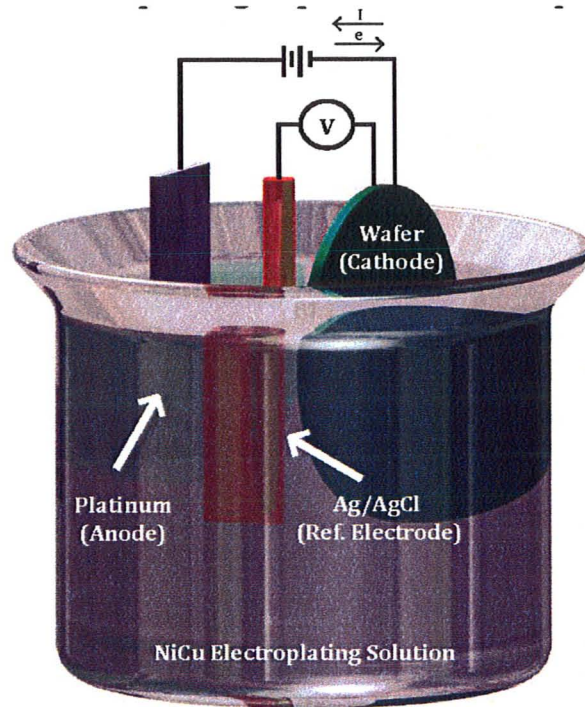


Figure 2-5: Electroplated potentiostatically setup in a three electrode cell

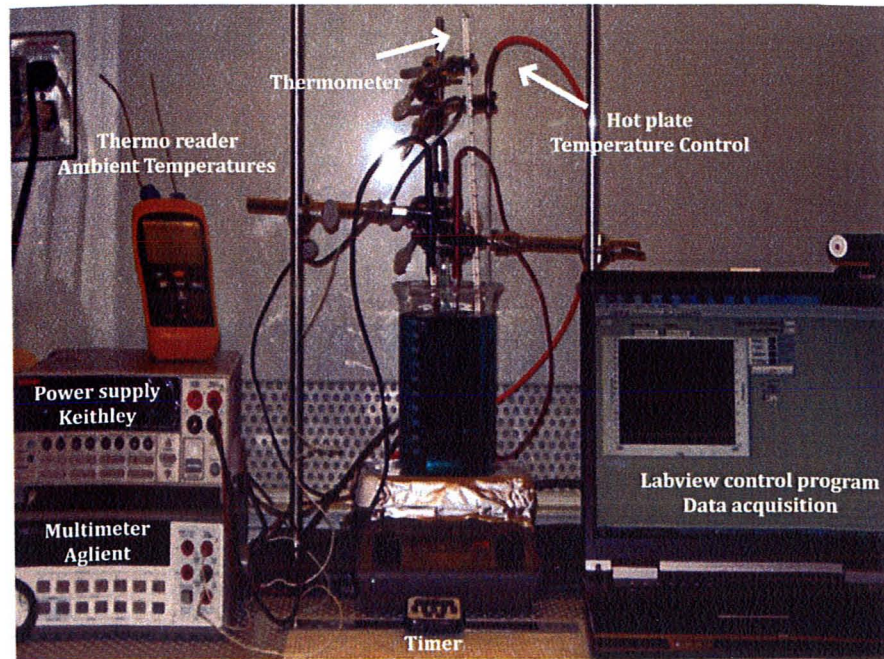


Figure 2-6: Experimental setup

The bath was operated at 30°C, in order to eliminate the effects of ambient temperature. Increasing the temperature promotes the more noble metal deposition. The deposition of the metal was controlled using a Labview interface, see appendix D, keeping the reference voltage constant in relation to the substrate by changing the potential between the power source [Keithley 2410] and the substrate, (see experimental setup Figure 2-6). It was agitated at 300 rpm by mechanically bringing fresh solution to the cathode surface, causing the diffusion layer thickness at the cathode to decrease. This promotes the more reactive metal (Cu) to deposit, by bringing fresh solution to the quiescent stationary double layer. The less reactive metals are thus removed. However this effect is minimal when dealing with complex ions (this case). The pH was acidic at 6. The pH generally doesn't affect the composition, however it is more important for regulating physical properties [20]. Deposition rates were typically 6.66 Å per second and deposition typically occurred for 5 minutes and resulted in 200 nm thickness.

In the potential range where reduction of Copper and Nickel occurred, hydrogen evolution is also present and cannot be neglected. Hydrogen evolution occurs at 0V referenced against a SHE, and in aqueous solution, is preferential to that of Ni reduction, see Table 3. Hydrogen evolution rates usually increase with increasing negative potentials. However due to polarization, hydrogen overvoltage potentials of some metals can be reached without discharge of hydrogen. Examining the Nernst equation 2-9 it is made up of standard potential and also a function of the ions activity values. By manipulating its second term and changing the concentration, the Ni reduction can be made to occur before the onset of Hydrogen evolution. When hydrogen evolution occurs

the metal ions will plate the cathode in an erratic manner, giving a dendritic structure, with poorly adhering coatings of insufficient thickness [21]. Avoidance of this is highly desirable.

Figure 2-7 shows the I-t curves with different electrolysis potentials. The curves show that a more negative potential will result in a larger reduction current. It can be seen from Figure 2-7 that a small increase in overpotential η will result in an exponential increase in the current density, which is described by the Butler-Volmer (equation 2-12).

The electroplated constantan composition was characterised using Energy Dispersive Spectroscopy (EDS). Figure 2-8 shows the percentage of Ni content in the alloy as a function of the deposition potential. The experimental results are plotted with experimental data obtained by Sartorelli, M.L. et al. [13]. The depositions of the Copper and Nickel ions are independent of each other, so the total voltage potentials are the sum of the voltage potential of their components. At more positive potentials the deposition of pure copper occurs. The electrolyte solution contains low concentrations of copper ions, its reduction is diffusion controlled [13] and follows the rules of mass transport with the limiting current of Cu^{2+} , see Table 3. Essentially, at low concentrations the Cu ions quickly dropped to zero where they have to be refreshed from the bulk solution. The new Cu ions must cross the thin double layer. Thereby the diffusion controls the rate of the reaction rather than the kinetics. Cu can be independently deposited (one of the criteria for alloy electroplating) at potentials lower than ($\sim -0.5\text{V}$).

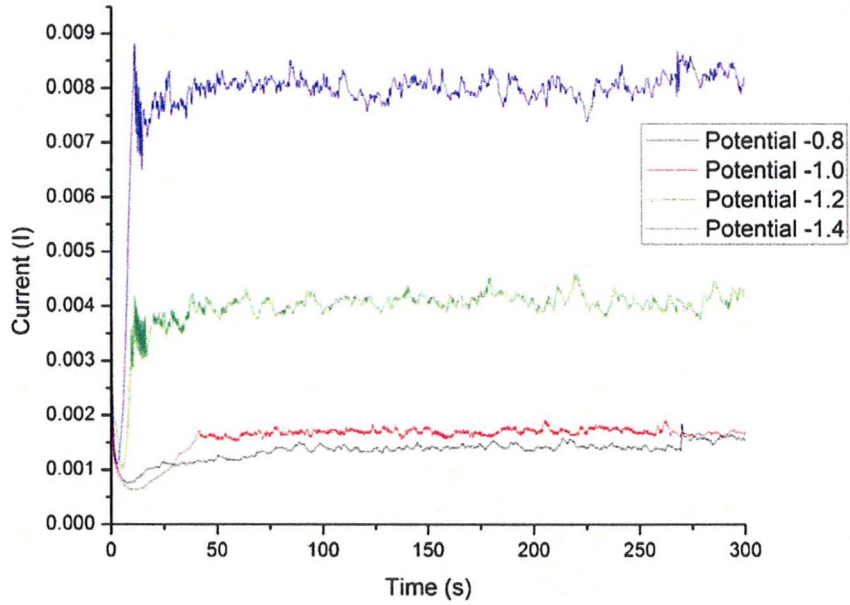


Figure 2-7: *I-t* curves of different potentials of -0.8, -1, -1.2 and -1.4 V's Ag/AgCl

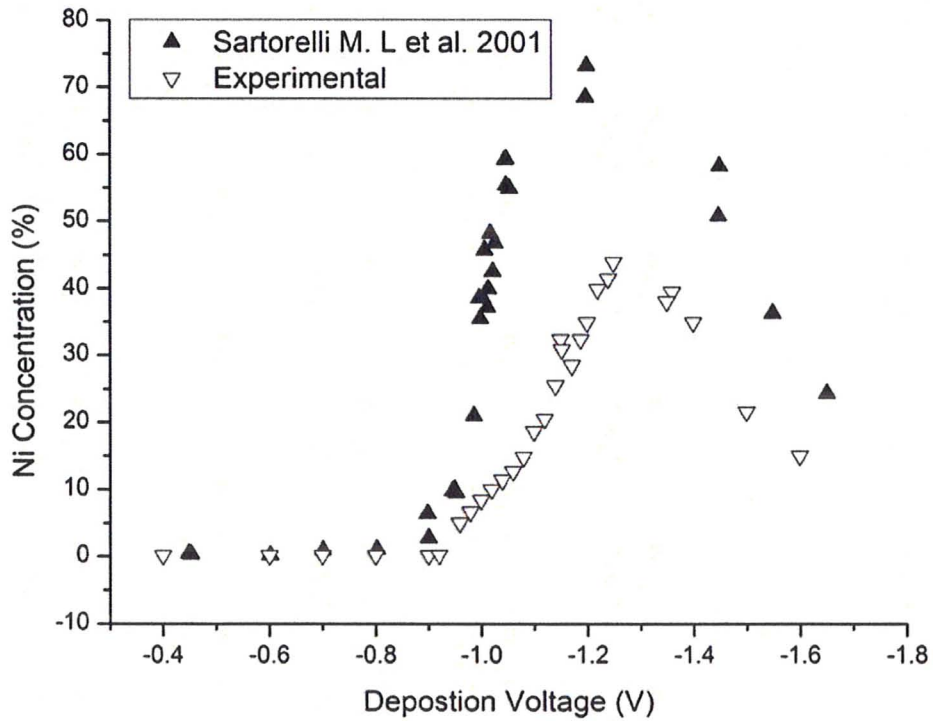


Figure 2-8: EDS results the percentage nickel with deposition voltage.

At the potential where Ni deposition ($\sim -0.95\text{V}$) begins, the Ni deposition is first charge transfer controlled. The partial current is again described by the Butler-Volmer equation 2-12. It can be seen that at large overvoltage, the charge transfer dominates. The increasing partial current of nickel deposition is added to the limiting partial current of Cu deposition [14]. As increasing polarization occurs at the cathode, the Ni ions discharge also becomes diffusion controlled and this explains the reduction of Ni content at even further negative potentials.

The deposits were of a smooth, metallic appearance. At low composition percentages of nickel the deposits were bright shiny reddish colour. With increase in composition of nickel that reddish shine became faded to be replaced by a bright metallic grey deposit. Scanning Electron Microscopy (SEM) showed the deposits to be homogeneous with small granularity, (see Figure 2-9 a). The grain size is dependent on the applied potential and at higher compositions of nickel larger granularity occurs. It was noted that the level of homogeneity of composition and grain size of the films declined past a negative potential of -1.25V . This represents the potential point where hydrogen evolution occurred. SEM images verified a high concentration of holes within non homogenous films once hydrogen evolution became established (see Figure 2-9 b).

The electroplating characterization results were consistent with previous research [13]. The variation between the results can be explained by a number of differences in the operating parameters and experimental setup (non agitation, saturated calomel electrode (SCE) reference electrode, platinum foil anode size, 0.478 cm^2 exposed plating area, 3 cm

distance between anode and cathode). Firstly, Sartorelli used a Saturated Calomel Electrode (SCE) as a reference electrode with potential voltage [$E_{25^{\circ}C}^{\circ}$] of 0.242 V with respect to SHE. A reference electrode is a device which has a well defined potential with respect to the SHE reference electrode [15]. In this study an Ag/AgCl reference electrode with a potential [$E_{25^{\circ}C}^{\circ}$] of 0.198 V with respect to SHE reference electrode was used [14]. Furthermore the operating bath temperature was set to 30°C that will further reduce the Ag/AgCl electrode potential with respect to the SHE reference electrode. The difference in the potential of the different reference electrodes can account for the more negative shift in the curve. The electroplating bath solution was agitated which has the effect of increasing the potential, see equation 2-9, of the nobler copper to deposit. This has the adverse effect of reducing the percentage of nickel thus reducing the height of the curve. Other possible discrepancies between the results are surface area of anodes, the surface area to be deposited on, different potentials between crystals sizes, and the nature of the metallographic crystal face exposed to the solution that may determine its potential.

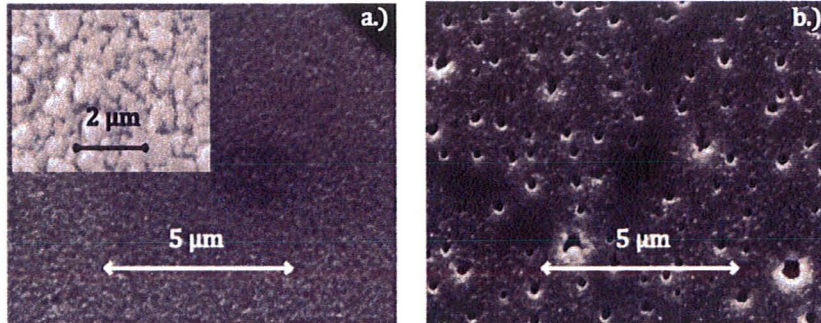


Figure 2-9: a) SEM picture of typical constantan thin film, b.) non-homogenous film caused due hydrogen evolution

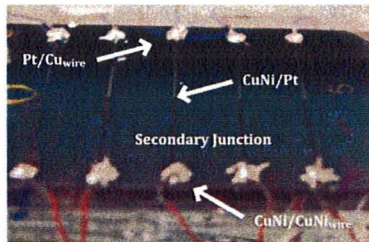


Figure 2-10: Picture of the leads attached with the silver conductive epoxy paste.

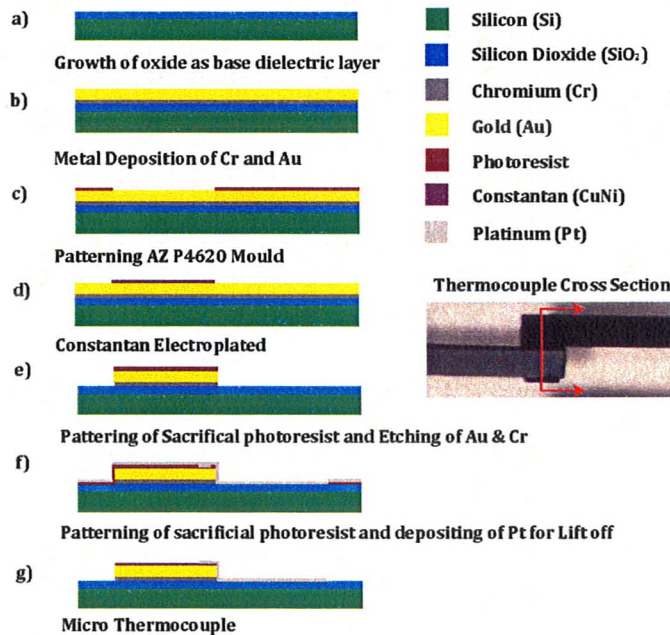


Figure 2-11: Process flow of micro thermocouple

2.6 Secondary Junctions and Lead Wire Attachment

Secondary junctions are unwanted junctions that contribute to the total generated e.m.f. When there are a number of such junctions in a sequence they each contribute to the total thin film thermocouple output. Reduction of errors can be optimised by attention to materials and the methods of attachment at these junctions. In order to minimize secondary junction effects, all components must be homogeneous, all like materials should have identical Seebeck characteristics and the temperature of all these identical junctions should be properly controlled [3]. Secondary junctions may arise due to the Seebeck coefficients of the thin films diverging from that of the contact wire, usually because of different crystal structures in each.

Two methods of attaching, the lead wires to the contact pads were considered:

1. Soldering – Soldering to a thin film sample requires extreme care and is undesirable because it is very difficult to make the contact areas small enough to avoid excess error. The sample may also be contaminated or damaged during the soldering process. It is therefore less than ideal as a method in this instance.
2. Silver conductive epoxy application is considered to be more optimal as it has a low thermal resistivity ($> 0.0004 \Omega\text{cm}$) and thermal conductivity (2.5 W/mK). Due to its low thermal diffusivity, this is ideal to reduce the effects of the secondary junction.

There were three junctions that contribute to the output of the TFTC, (see Figure 2-10):

1. Platinum /Cu lead wire (due to cost considerations),

2. Constantan /Platinum (measurement junction),
3. Constantan / Constantan lead wire.

Traditionally, macro scale thermocouples are characterized in a thermal bath to determine their sensitivity. This only works at the micro scale if the secondary junction thermal diffusivity is of the order of 10 % and the connection pads are at a far enough distance from the heat source. It is also necessary to keep the secondary junction away from the bath itself, keeping it at a constant different temperature to that of the thermal bath in order to get reasonably accurate Seebeck coefficients.

Platinum being the most expensive material was foregone in preference to Silver conductive epoxy and thin copper lead wires. The effects of platinum copper junctions at known temperatures were determined using existing thermocouple tables, see Table 3.

A test to determine if there was EMF generated at these junctions was performed in a similar manner to Jia et al. [22]. Each junction was cooled separately down to a temperature of 77K or -196 °C with a drop of liquid nitrogen and the voltage was measured. It was found as expected that an EMF was generated when either Pt/Cu lead wire or the CuNi /Pt junctions were cooled. However, there was no EMF detected when the CuNi / CuNi lead wire junction was cooled. This was due to the fact that the composition of the electroplated constantan matched that of the constantan lead wire.

2.7 Thermocouple Fabrication

Initially, a thin silicon oxide (SiO_2) layer of 9000 Å was grown on a silicon wafer as shown in Figure 2-11 (a). The SiO_2 layer acts as an electrical insulator (dielectric layer). A 60 Å layer of chromium followed by a 200 Å layer of gold was deposited on the Silicon Oxide as a plating base, shown in Figure 2-11 (b). Chromium acts an adhesion layer between the gold thin film and the substrate.

The gold acts as a seed layer for subsequent electroplating. Subsequently, the wafer was plasma oxidized at 80 W for 1 minute to remove any organic residues and improve surface adhesion. A thick positive photoresist (AZ P4620) was spun cast at 3000 rpm for 30 seconds. The sample was baked at 100 °C for 4 minutes. The substrate was exposed through the first mask for 39 seconds at 7.6 mJ/sec and was developed in 1:3 AZ 400K to DI water for 2 minute to pattern the moulds for the electroplating as shown in Figure 2-11 (c). A picture of the mould is shown in Figure 2-12 (a). Constantan was electroplated onto the exposed gold surface (Figure 2-12 (b)) using the following conditions. The constantan-plating solution consisted of 26.47 g/L nickel sulphate, 3 g/L copper sulphate and 49.035 g/L Citric Acid Trisodium Salt [19]. The plating was performed potentiostatically (-1.09V with reference to a Ag/AgCl saturate electrode) in a three-electrode cell, as shown, see Figure 2-5 producing a deposition rate of 6.66 Å per second. A labview control program was used to control the homogenous of the film. Initially the reference voltage was ramped up to avoid hydrogen evolution. This would give alloy compositions of 16.3 Nickel and 83.7 Copper, which was picked to match the composition of constantan lead wire. The photoresist was dissolved in acetone and the

substrate was subsequently plasma oxidized at 80 W for 5 minutes in order to completely remove the photoresist. Afterwards, S-1808 photoresist was spun cast at 3000 rpm for 30 seconds. The sample was soft baked at 110 °C for 90 seconds. The substrate was exposed for 5 seconds at 7.2 mJ/sec to pattern to protect the thermocouple leg while etching using the second mask and was developed in 1:5 developer 351 to DI water for 25 seconds. Commercial gold etchant [Sigma-Aldrich] and a nickel compatible chromium etchant [Cyantek Corp.CR100] were used to etch the base seed layer, Figure 2-11 (e). The photoresist was removed by acetone and the substrate subsequently plasma oxidized at 80 W for 5 minutes in order to completely remove the residual photoresist. Next, primer [MicroPrimer HP Primer, ShinEtsuMicroSi] was spun cast at 4000 rpm for 30 seconds. Following this, S-1808 photoresist was spun cast at 4000 rpm for 30 seconds. The sample was soft baked at 90 °C for 2 minutes. The substrate was exposed for 5.63 seconds at 7.1 mJ/sec, using the third and final lift off mask to pattern the platinum component of the thermocouple. It was then soaked in toluene for 6 minutes before being blown dry by nitrogen. The toluene modifies the top layers of the photoresist, hardening them, making them more difficult to develop away. This causes an undercut profile of the developed photoresist, which causes a break in the deposited metal films and ensures easy lift-off. It was developed in 1:5 developer 351 to DI water for 90 seconds. A 60 Å layer of chromium followed by a 1200 Å layer of Platinum was deposited on the substrate, shown in Figure 2-11 (f). Chromium acts an adhesion layer between the platinum and the substrate. The platinum was released, upside down, in a bath of acetone. The photoresist was removed by acetone and subsequently plasma oxidized at 80 W for 5 minutes in

order to completely remove the residual photoresist. Figure 2-13 shows a complete fabricated thermocouple. The complete process flow for the micro thermocouple is contained in Appendix A.

2.8 Thermocouple Experimental Setup

The primary function of the experimental setup is to characterize the micro thermocouple. The facility is shown schematically in Figure 2-14. The experimental setup allows the determination of the sensitivity (Seebeck coefficient) of the micro thermocouples and characterizes the voltage output as a function of temperature.

The test facility consists of a thermal bath NESLAB RTE 10 [Thermo Electron Corporation] with built in RTD temperature control. An Omega 710 RTD calibrated to ± 0.03 °C was used as the reference temperature for calibration (see appendix B) and was measured using a 34401A multimeter [Agilent] with data acquired using a GPIB-USB-HS and Labview. The micro thermocouple output voltage was measured using a 34401A multimeter [Agilent] which had a resolution of 1 μ V and accuracy of ± 5 μ V. 52II thermometers [Fluke] were used to measure ambient temperature, the temperature of the surface of the micro sensor, and the secondary junctions temperatures with accuracy of ± 0.1 °C.

The NESLAB RTE 10 thermal bath was powered up and on reaching the desired temperature was allowed to operate for a further 1 to 1 ½ hours to ensure thermal equilibrium. The test section was immersed in the bath until its thermocouple junctions were completely submerged in water, keeping the secondary junction above the water

level of the bath. The substrate was located a distance of 10 mm away from the reference RTD. Thermal equilibrium was assumed between the bath temperature measured by the reference RTD and the junction of the thermocouple when all the embedded macro T type thermocouple remained constant for a period of no less than 5 minutes. The T-type thermocouple was embedded between the substrate and glass backing and is not in contact with the water. Steady state was assumed to have been reached between the temperature of the bath and the thermocouple voltage response when a period of time long enough for the temperature of the thermal bath to equal to the temperature at the thermocouple junction had passed, as the glass has a large thermal conductivity, see Figure 2-15.

Between tests the substrate was removed from the bath in order to reduce the effect of conduction through the substrate on the secondary junction. The temperature of the secondary junction is measured using a separate T-type thermocouple and this measurement was used to determine the added EMF of this secondary junction from reference thermocouple tables, see Figure 2-15. The T thermocouple was attached with thermal paste to surface adjacent to the secondary junction.

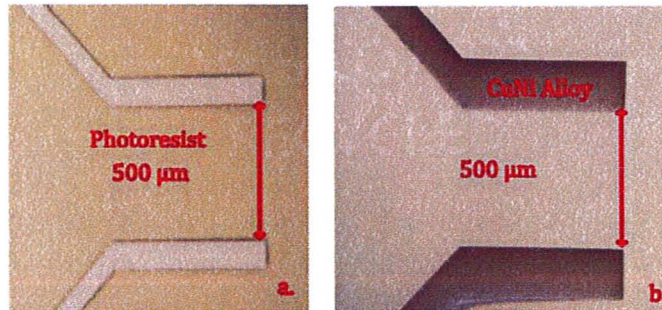


Figure 2-12: (a) First mould of positive photoresist (b) Constantan electroplated

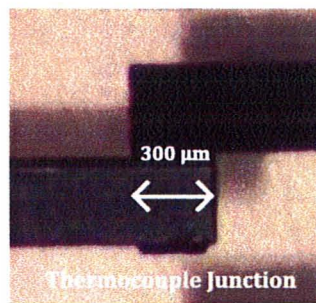


Figure 2-13: Completed fabricated micro thermocouple

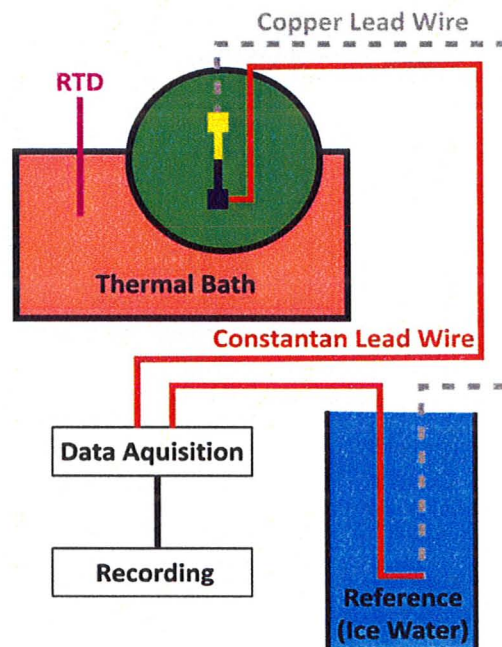


Figure 2-14: Schematic of characterization of micro thermocouples

2.8.1 Effect of Seed Layer on the Underlining Micro Thermocouple

To assess the effect of the seed layer on the micro-thermocouple, a macro thermocouple of wire diameter of $(0.002'' \Phi)$ was sputter coated with 1000 \AA of gold on its junction and was compared with an identical macro thermocouple of $(0.002'' \Phi)$. The macro thermocouples were submerged into the thermal bath with the micro thermocouple. The macro thermocouple temperatures were read directly off a 52II Thermometer [Fluke]. It was seen that the thermocouple temperature readings were offset by $0.01V$ throughout the experiments.

From the macro tests we can conclude that the effect of the seed layer shifts the curve upwards, however the slope remains the same, and therefore the sensitivity of the thermocouple remains the same. In the fabrication of the micro thermocouple the gold seed layer is over etched to prevent a junction forming between it and the constantan and Platinum thin films. This allows us to conclude with some degree of confidence that the effect of the gold seed on the overall Seebeck effect can be neglected.

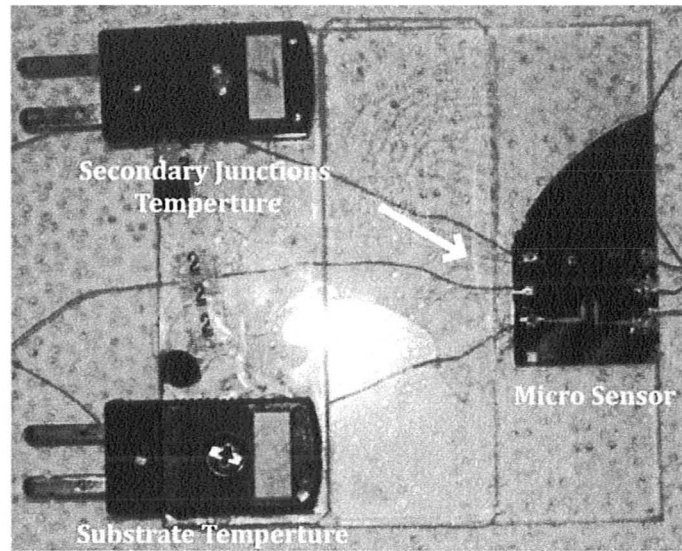


Figure 2-15: Picture of the test section used in calibration micro thermocouples

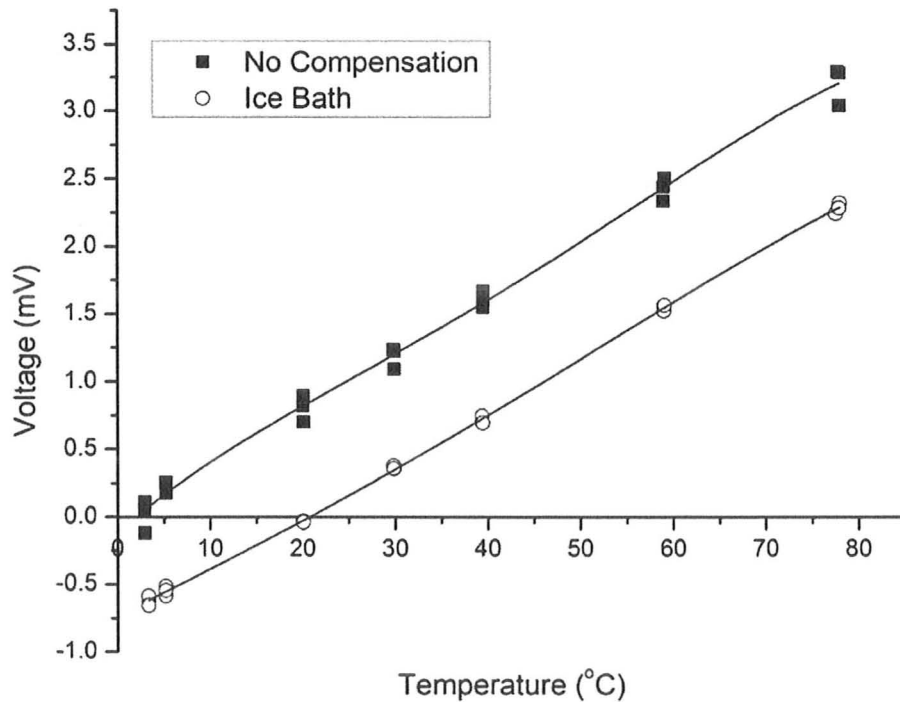


Figure 2-16: Calibration curve for thermocouples consisting of 16.31%Ni 83.69 % Cu. The lower curve represents when an ice bath was used and has a slope of $39.04 \mu V/^{\circ}C$. The upper curve is where the no compensation was used and has a slope of $41.75 \mu V/^{\circ}C$.

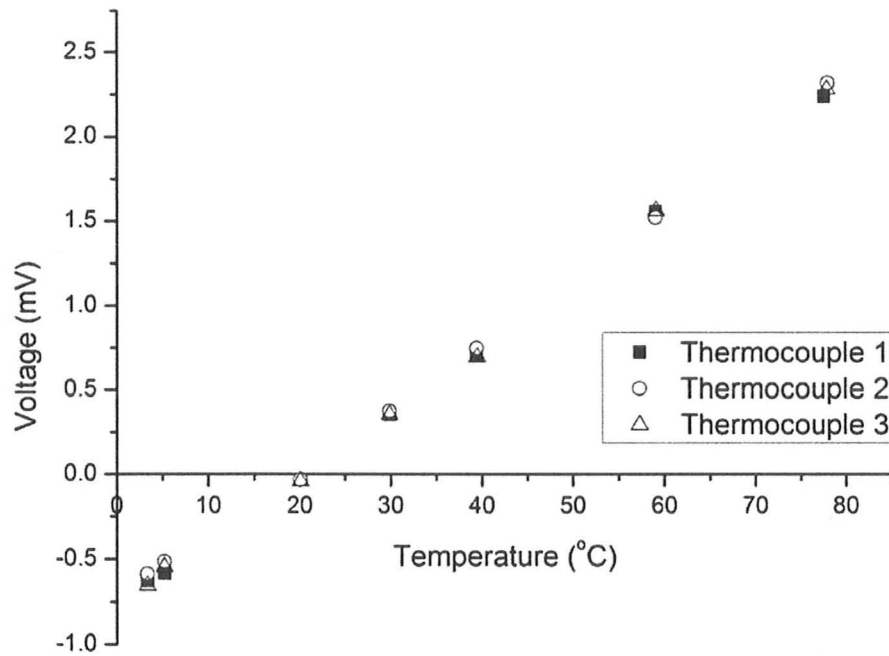


Figure 2-17: This plot represents the consistence between different thermocouples in devices

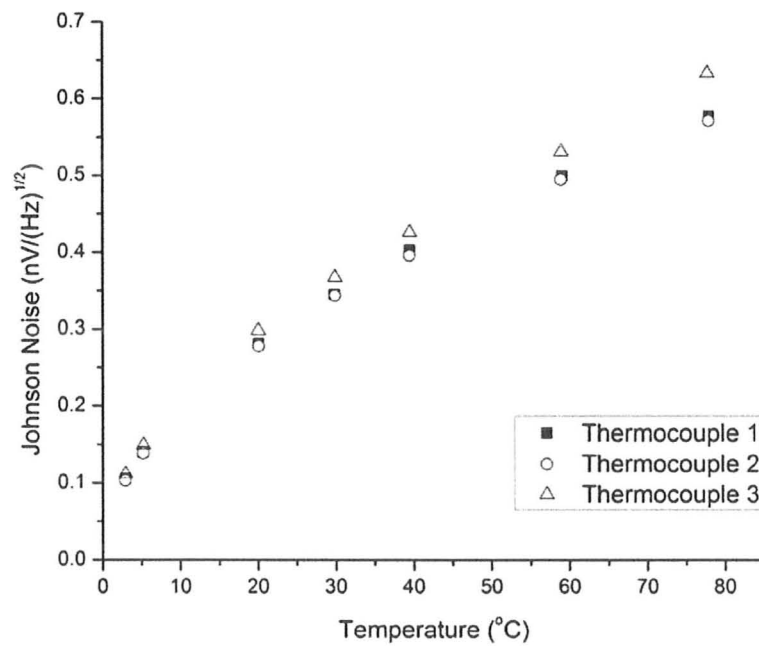


Figure 2-18: Plots the Johnson Noise verse Temperature for the three different thermocouples

2.9 Micro Thermocouples Results

The sensitivity of the constantan electroplated metal was tested using a thermal bath as stated previously. The platinum leg of the thermocouple acted as a reference allowing the determination of the Seebeck coefficient of the thin film. One batch of micro thermocouples was calibrated. Initially, tests between each set of thermocouple junctions sizes were carried out, (50 μm up to 500 μm) and consistency between readings was confirmed. Final calibration on this batch consisted of measurements on 3 micro thermocouples of junction size 300 μm . For each thermocouple 6 measurements were taken at each temperature point, 3 with ice bath compensation and 3 with no compensation. Subsequently these points were averaged, for both the ice bath compensation and no compensation cases, and the calibration curves were plotted and are presented in Figure 2-16. The constantan compositions for this batch was 16.3 % nickel and 83.7 % copper with a deposited thickness of 2000 \AA . The Seebeck coefficient was expected to have different sensitivity properties to that of the bulk material and this is consistent with other previous research [9; 13; 18; 19].

Figure 2-16 is a plot of both compensated and non compensated calibration curves for the constantan platinum micro thermocouple. The compensated micro thermocouple had two junctions, the constantan-platinum measuring junction and a secondary junction of platinum- copper that was at a known temperature. In order to get a more realistic measurement of sensitivity the follow equation was used.

$$V_{corrected} = V_{measured} - V_{PtCu} \quad 2-16$$

where $V_{corrected}$ is the actual voltage contributed due to the CuNi-Pt junction, $V_{measured}$ is the experimental voltage and V_{PtCu} is the theoretical voltage of copper at the known temperature of the Pt-Cu junction, from Table 2Table . At each temperature measurement point, the three measurements were averaged and a linear curve was fitted with OriginPro 8¹ software. The relative Seebeck coefficient is derived from the slope of the temperature difference with voltage curve, see Figure 2-16. The slope of the calibration curve (the sensitivity) was $39.04 \mu V/^{\circ}C$ with a standard deviation of $3.34 \mu V$. The calibration curves are typical piecewise polynomial curves consistent with the standard ITS-90 for thermocouple references. The calibrated equation of the ice bath compensated micro thermocouples is

$$V = -73.463 \times 10^{-5} + 34.74 \times 10^{-6} T - 22.478 \times 10^{-7} T^2 + 31.752 \times 10^{-8} T^3 - 28.7291 \times 10^{-10} T^4 \quad 2-17$$

The non compensated micro thermocouple had three junctions, the constantan-platinum measuring junction, a secondary junction of platinum-copper that was at a known temperature and secondary junction consisting of a CuNi-Cu junction (T-type thermocouple). The temperature of the final secondary junction was taken at the room temperature. The following equation was used to find the corrected voltage measurement.

$$V_{corrected} = V_{measured} - V_{PtCu} - V_{Cu NiCu} \quad 2-18$$

¹ Thermocouple calibration curves are piecewise polynomial curves as set out by standard ITS-90 for thermocouple references. However, to determine Seebeck coefficients the standard is to determine the slope from a linear fit curve from the experimental data

where $V_{corrected}$ is the actual voltage contributed due to the CuNi-Pt junction, $V_{measured}$ is the experimental voltage, V_{PtCu} is the theoretical voltage of Copper at the known temperature of the Pt-Cu junction, and V_{CuNiCu} is the theoretical voltage at measured room temperature of the T-type thermocouple junction, the final two terms being determined from Table . The slope of the calibration curve (the sensitivity) of the non compensated micro thermocouple was $41.75 \mu V/^{\circ}C$ with a standard deviation of $7.458 \mu V$. The calibration equation of the non compensated micro thermocouples is

$$V = -11.268x10^{-5} - 59.24x10^{-6}T - 9.5026x10^{-7}T^2 + 1.78095x10^{-8}T^3 - 1.07493x10^{-10}T^4 \quad 2-19$$

In Figure 2-16 there is an offset of 0.622 mV between the calibration curves. The shift in curves can be explained by third empirical law of thermocouples, the law of Intermediate temperatures [3], where a reference temperature can be used at any other reference temperature once there is a known linear correlation.

The main contribution of this shift is the 3rd extra junction when considering the micro thermocouple. The fact that another junction is exposed, for the non compensated thermocouple, means that there is an additional contribution to the overall EMF. A theoretical correction factor was incorporated to approximate the associated EMF that generated with the secondary junction. Also, there is a larger scatter of the readings. The difference in slopes can be attributed to ambient fluctuations ($\pm 2^{\circ}C$) throughout the course of the experimental run, that would be detected by the exposed secondary junction. This is also the reason for the larger slope for the non compensated micro

thermocouple at $41.75 \mu\text{V}/^\circ\text{C}$ compared to $39.04 \mu\text{V}/^\circ\text{C}$ of the compensated micro thermocouple.

The standard deviation for the non compensated thermocouples of $7.458 \mu\text{V}$ was almost twice that of the ice bath compensated thermocouples at $3.34 \mu\text{V}$. Even though non compensated thermocouples are not the correct method of implementation of thermocouples as they are less accurate, it does raise a possibility for future refinements of measurement in microfluidic devices where space is of a premium. The disadvantage is obviously the loss of accuracy.

Initially, for the constantan material a negative slope curve was expected. However, this was not the case. Constantan is an alloy which is made up of 45% nickel and 55 % copper (bulk Seebeck coefficient $-37.2 \mu\text{V}/^\circ\text{C}$), whereas the batch of micro thermocouple that were calibrated had thin films with a composition of 16.31 % nickel and 83.69 % copper. This would most likely reduce the negative Seebeck coefficient significantly. Another factor is the thickness of the thin film layer. Higher compositions of the Nickel rich thin films were fabricated; however, the film thickness remained relatively low as hydrogen evolution occurred when the Labview control program (see appendix C) was left on for a long duration of time. This was due to the fact, that to keep the reference electrode at the constant voltage over a period of time, an iterative method was used over time that increases the voltage between the cathode and anode. Either a pulse electroplating method or patch on the Labview program may fix this problem. These higher Nickel compositions were not calibrated at this time as the focus was on the overall completion

of the device. Other possible factors that may affect the properties of CuNi thin film are impurities from the Au bond coat, surface effects, or substrate generated stresses [18].

Figure 2-17 is a plot of the Seebeck calibration curves for three micro thermocouples from the same batch. It can be seen from the plot that the micro thermocouples are highly consistent with a standard deviation error of $3.34 \mu\text{V}$. This indicates that the electroplating thin film was homogenous and this was confirmed with SEM pictures. The small fluctuations between thermocouple measurements can be accounted for by the slightly different lead wire and lead wire length. Figure 2-17 confirms that only one thermocouple need to be calibrated in a batch of micro thermocouples to have an accurate measurement device. This is particularly important when dealing with MEMS devices as thousands of sensors can be fabricated on a substrate, and individual calibration per sensor would become tedious.

Johnson noise has a significant role when using a thermocouple as this limits its sensitivity. The signal to noise ratio should be as high as possible for best detection of thermal change in a fluid. Figure 2-18 is a plot of Johnson noise with respect to temperature for the three different thermocouples. It can be seen that this thermal noise is exponential dependent to upon the increase in temperature. Thermocouple 1 and Thermocouple 2 are reasonably consistent with each other. However, there is an increase in noise for Thermocouple 3 that may be due to the slightly different attachment of the extension leads, which act as antenna for picking up noise. The signal to noise will be

discussed again in chapter 4 as it plays a significant role in the detection of changes in the thermal pulse that is generated from the micro heater, which is presented in Chapter 3.

2.10 Summary

This chapter presented an overview of the development of micro thermocouples in this study. Classification schemes, fundamentals and governing equations were first discussed. The rationale of choosing constantan thin films is explained. Critical design specifications of the electroplating are discussed. Calibration of the composition of nickel to the electrical potential is presented and examined. Secondary junctions effects as sources of additional erroneous EMF are examined. The microfabrication process developed for the micro thermocouples is presented along with the advantages and limitations of each step of the procedure. The experimental calibrations of three micro thermocouples for both compensated and non compensated cases were presented. The calibrations produced a slope of $39.04 \mu\text{V}/^\circ\text{C}$ for ice bath compensated and $41 \mu\text{V}/^\circ\text{C}$ for non compensated thermocouples. The consistency of the homogeneity of micro thermocouples is discussed and the calibration curves for both cases are presented. Finally, the effect of signal to noise is investigated.

Chapter 3: Micro Heater

3.1 Introduction

In the previous chapter we examined the method of detecting thermal changes within microfluidic devices using micro thermocouples. In this chapter a method of introducing a thermal pulse into the system will be discussed. In particular, the development of a micro heater will be presented.

Micro heaters have extensive applications in MEMS devices as they utilize low power consumption, have fast response times, high mechanical stability, high fabrication yield, high density integration and controlled functionality. Micro heaters have high surface to volume ratios. This tends to improve the heat transfer within small volumes making fast reaction control possible. Applications include micro gas sensors, pressure sensors, flow rate sensors, micro explosive boiling, micro ignition of micro propulsion systems, and thermal micro sensors or micro actuators [24; 25; 26].

There are two types of micro heater; the wire heater and the thin film heater. The thin film micro heater has several advantages over the wire heater such as lower mass and ease of compatibility and integration with other devices. Micro heaters provide the ability to thermally activate systems at precise locations, and they can facilitate the integration of sensor arrays. They have linear variation of resistance with temperature making them particularly good for ease of calibration. A simple meandering type resistor micro-heater

was chosen as the primary design for this work because it was small, and can be easily micro fabricated and integrated into micro systems relatively inexpensively, see

Figure 3-2.

Direct measurements of temperature in micro heaters are notoriously difficult due to their small dimensions [27]. In this study the surface temperature of the micro heater was determined by calibrating the known change of resistance of the material as a function of temperature.

The specific objective was to design, micro-fabricate and test a meandered type micro scale heater. The following section describes the literature review of existing research in the field with an emphasis on meandered type micro heaters. The fundamental physics of the heat transfer phenomenon and the governing equations, the materials, the fabrication methods, fabrication process flow, and complete characterization results for the micro heater are presented.

3.2 Fundamentals and Governing Equations

Metals that are commonly used in the construction of micro heaters are ohmic so changes in the resistance can be calibrated versus temperature in a uniform temperature environment. Subsequently the supply input power can be calibrated with the resistance of the micro heater. For a given power input, it is possible to estimate the average temperature of the heater from resistance measurements. A resistance micro heater is governed by Joule heating (resistive or ohmic heating). This is a process by which

electrical energy in the form of current is passed through the conductor to release thermal energy to the medium in contact with the heater. The heat generated from Joule heating is

$$Q = I^2 R t \quad 3-1$$

where Q is the energy generated by a constant current I , R is the electrical resistance and t is the time.

The effect of conduction through the substrate is examined below, with heat transfer effects such as convection and diffusion discussed in Chapter 4, while radiation is neglected throughout as its value is negligibly smaller than that caused by thermal conduction.

Thermal conduction is governed by Fourier's law of conduction, and is given by

$$Q = -\kappa A \frac{dT}{dx} \quad 3-2$$

where Q is the heat transfer [J], κ is the conductivity of the material [W/mK], A is the area of contact and $\frac{dT}{dx}$ is the temperature gradient. The thermal conductivity of the material can be related to the thermal resistance as

$$R_t = \frac{t}{\kappa} \quad 3-3$$

where R_t is the thermal resistance [$\text{m}^2\text{K}/\text{W}$], κ is the thermal conductivity of the material [W/mK], and t is the thickness of the micro heater material [m]. A simple 1-D thermal

resistance model was used to compare substrate materials, and approximate input power for the heater.

Table 5: Thermal Conductivity and thickness of materials for 1-d thermal resistance model

	Gold	Silicon	Silicon Oxide	Glass
Thermal Conductivity [W/mK]	0.58	141.2	1.026	1.18
Thickness [μm]	3	475	0.9	475

3.3 Literature Review

Research on micro heaters to improve heating characteristics while minimizing power consumption has been performed [28]. Micro heaters using thin film Pt\Cr and Pt\MgO deposited on cantilevers (thermal bridge) that were made up of dielectric materials have been examined. Dielectric materials such as $\text{Si}_3\text{N}_4/\text{SiO}_2/\text{Si}_3\text{N}_4$ (N/O/N) showed high thermal isolation characteristics; however, they had limited life span and were fragile and subject to mechanical shock which gave limited design applications [24].

Chung, G.S. [24] examined the effect of trench structures constructed beneath low power micro heaters. The platinum heater was fabricated with a buffer layer of MgO between it and the silicon oxide substrate. They examine the effect of conduction and also power consumption for devices consisting of zero to 10 trenches. They found a better temperature distribution with an increase in the number of trenches, larger width and gap. For a power input of 0.9 W, in the presence of 10 trenches an operating temperature of 580 °C was achieved. For devices where no trenches were fabricated on the device an operating temperature of 280 °C occurred for the same input power of 0.9 W. These

lower heating characteristics were due to the high thermal conductivity of silicon. The increasing number of trenches improved thermal isolation as well as reduced the thermal losses. Consequently, a lower power consumption was required as the trenches reduced the effects of conduction by isolating the heater from the rest of the substrate.

Limitations of micro heaters that were fabricated on heavily p-doped silicon were examined by Fung, S.K.H. [29]. The polysilicon micro resistance heater was sputter coated with tin oxide and/or aluminium that acted as a hotplate which was designed to reduce thermal gradients. Despite the excellent material properties of silicon they found that a relatively high power consumption was required. For micro-heater filaments that are thermally insulated from the rest of the substrate surface, a back etching is required to leave a thin thermal bridge. In the case of a micro heater on a silicon substrate, temperatures of 800 K can easily be achieved with input power in the range 30-150 mW. Tiggelaar, R. M. et al. [30] fabricated 5 platinum meandering micro heaters over an area of 4.1 mm x 450 μm , with heater cross sectional width of 50 μm . The micro heater was used in a micro-reactor for gas phase reactions within a channel. The platinum heaters were deposited onto a substrate of heavily doped mono crystalline silicon, with an insulating layer of silicon nitride. The substrate was back etched to create a membrane for which rhodium was deposited at the middle/hottest point of the heaters as a catalyst for the micro reactor. The micro heaters were operated at power inputs of 0.4 W and this resulted in operating temperatures between 550-600 $^{\circ}\text{C}$. Analytic models for the temperature profiles were presented and different heater shapes (meander, sinusoidal and parallel bars) compared for both thermal and mechanical behaviour. A sinusoidal shaped

heater had the highest temperature distribution; however, its mechanical stability was lower than that of the meander design. The parallel bars had the lowest thermo-mechanical stresses. The main draw back was the inability for integration of sensors between the heaters.

Baroncini, M. Et al. [26] proposed a double spiral heating element for steady state localized uniform heating over the sensing area of a gas sensor. They fabricated a four-point probe micro heating element and developed a simple analytical model for it. The Pt/Ti micro heater was fabricated on a silicon nitrate substrate. They thermally isolated the device by anisotropically etching the backside of the silicon wafer. A peak temperature of 460 °C was achieved with an average approximate temperature gradient of 0.05 °C/μm, for a power input of 70 mW.

Zhang, K.L. et al. [27] designed a thin film gold/titanium micro heater for applications of micro-thruster ignition and micro boiling on a pyrex bulk substrate. They performed experiments to determine the resistivity and thermal conductivity of the thin film which differed from the bulk properties. The heater produced a temperature change of 80°C for an input of 5V over a period of 2 seconds, 300°C for an input of 8V for a period of 1 second and 400 °C change for 10V for a period of 2 seconds. This surface temperature was considered well suited for a short temperature pulse application and the same geometry of the meandering micro heater were used in this project. The differences between the designs were the materials used and the method of attaching the lead wires to the connection pads.

Platinum was preferred by some of the previous researchers for the micro heater as it had better controllability in terms of bulk resistance. In our research it was decided that the micro heater would be fabricated out of gold to allow easier integration of the micro heater with the subsequent flow sensor. To simplify the fabrication process, a glass based meandering micro heater was designed in order to eliminate anisotropic etching that is associated with silicon based microfabrication.

3.4 Materials

The materials for the sensor substrate and heater element were selected based on their thermal and electrical properties and feasibility of microfabrication using current technology. A flat smooth 350 μm thick Pyrex was selected for the substrate because of its low thermal conductivity and its capacity to thermally insulate, thereby isolating the heater electrically and thermally. This allows good heat confinement to be achieved and low power consumption. Gold was selected for the heater base because of its high electrical and thermal conductivity, high resistance to electrochemical corrosion and oxidation, and ease of integration of the heater with other sensors. A 400/800 \AA thick layer of gold was deposited on the glass substrate. This range of thickness was chosen to minimize the cross sectional area and consequently lower the resistivity. The width of the meandering micro heater film was 50 μm due to constraints of the lithography process, (alternative more expensive masks would be required for smaller features) and similarity in the design geometry of Zhang, K.L. et al. [27]. Since gold does not adhere to the glass substrate, a thin nominal chromium layer of 60 \AA was deposited as a seed layer for the gold deposition.

3.5 Microfabrication Process

The micro heater was fabricated using a one mask process as shown schematically in Figure 3-1. A 375 μm thick glass wafer was used as the substrate. A 100 \AA layer of chromium followed by a 400 \AA layer of gold was deposited on the glass substrate for the heater material, as shown in Figure 3-1 (a). Chromium acts as an adhesion layer between the gold thin film and the substrate. Subsequently, the wafer was plasma oxidized at 80 W for 5 minute to remove any organic residues and improve surface adhesion. S-1808 photoresist was spun cast at 3000 rpm for 30 seconds. The sample was soft baked at 110 $^{\circ}\text{C}$ for 90 seconds. The substrate was exposed for 5 seconds at 7.2 mJ/sec to pattern the micro heater using the second mask (see appendix A) and was developed in 1:5 developer 351 to DI water for 25 seconds, (Figure 3-1 (b)). Commercial gold etchant [Sigma-Aldrich] and a nickel compatible chromium etchant [Cyantek Corp.CR100] were used to etch the base layers, (Figure 3-1 (c)). The photoresist was removed by acetone and the substrate was subsequently plasma oxidized at 80 W for 5 minutes in order to completely remove the residual photoresist, revealing the micro heater (Figure 3-1 (d)). A picture of the micro heater is shown in Figure 3-2.

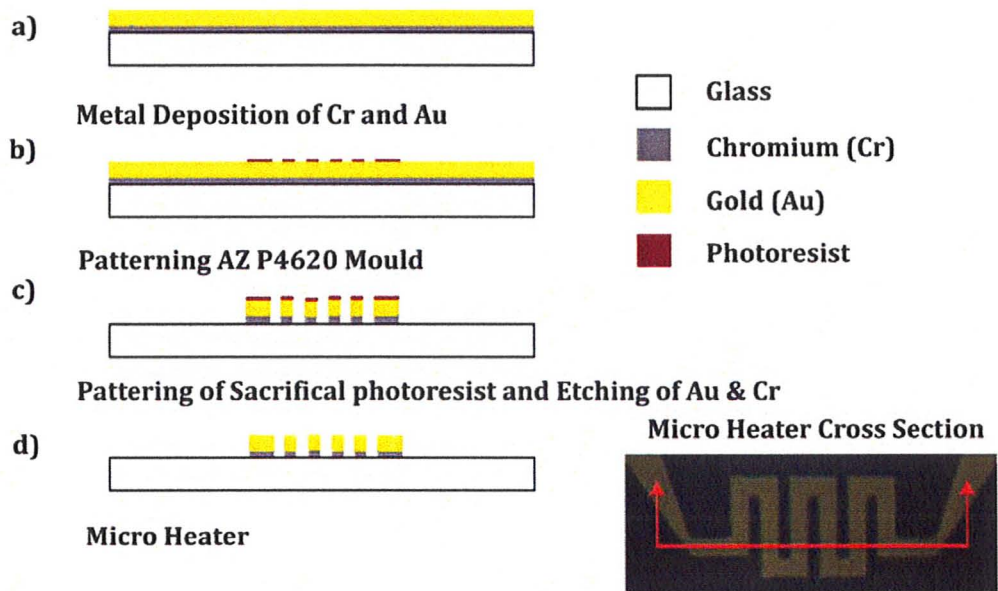


Figure 3-1: Heater fabrication process flow.

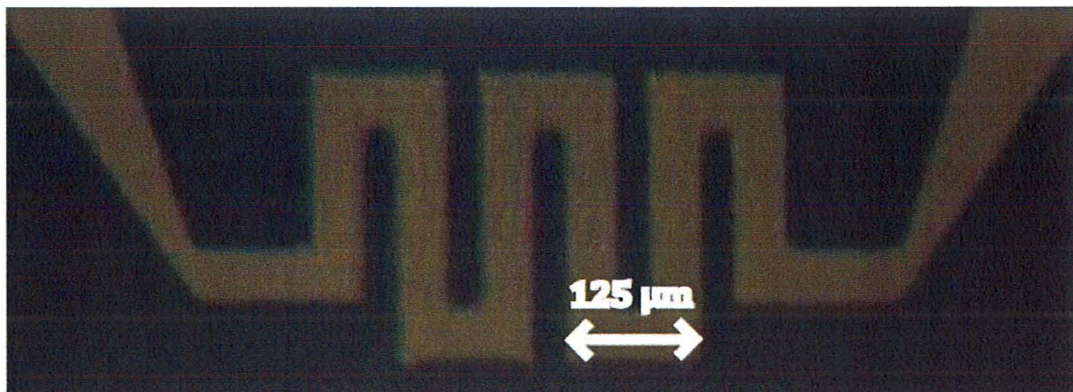


Figure 3-2: Micro heater

3.6 Experimental Setup

The micro heater was characterized in situ with the micro thermocouples, using the thermal bath NESLAB RTE 10 [Thermo Electron Corporation] (see schematic in Figure 2.15). The facility allowed the determination of resistance as a function of temperature. An Omega 710 RTD calibrated to ± 0.03 °C was used as the reference temperature for calibration and was measured using a 34401A multimeter [Agilent] with the data acquired using a GPIB-USB-HS and labview, to determine steady state, as discussed in section 2.7.

A four point resistance probe was connected to the lead wires (each length 3') which were connected to the micro heater, and was measured using a 34401A multimeter [Agilent]. The micro heater resistance measurements were taken using a 34401A multimeter [Agilent] that had a resolution of 3 m Ω and accuracy of ± 3 $\mu\Omega$. Steady state was taken when thermal equilibrium had been achieved (i.e. when the T-type thermocouples that were embedded in the micro thermocouple setup remained constant for a duration of not less than 5 minutes). The average resistance reading was determined as a function of a known temperature, and was subsequently correlated to self heating measurements at selected power levels. Thus a correlation of average temperature of the surface of the heater versus power levels was achieved.

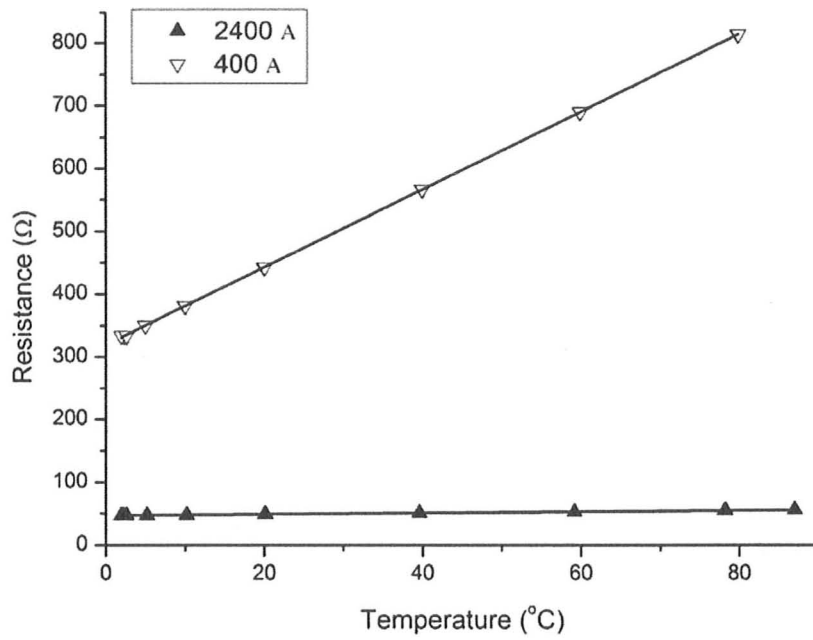


Figure 3-3: Calibration curve of resistance surface temperature of the heater

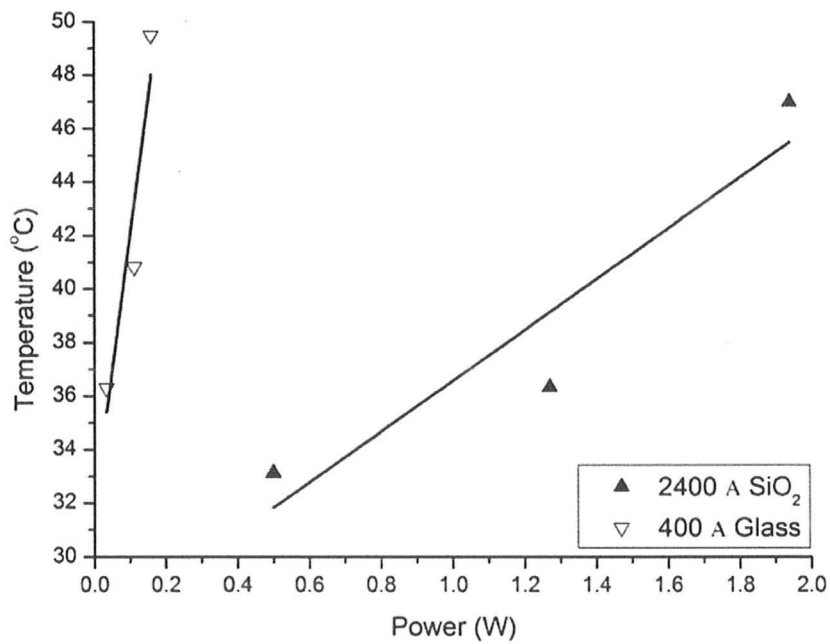


Figure 3-4: Microheater maximum temperature versus electrical power input

3.7 Micro Heater Characterization

A meandered micro heater was fabricated in order to introduce a thermal pulse into a micro channel. The calibration of the resistance for known uniform temperatures was performed using a thermal bath as described previously. For each micro heater, three measurements were taken at each temperature point. Subsequently these points were averaged and the calibration curves were plotted, as shown in Figure 3-3.

The calibration curve is linear, and shows the temperature dependent relationship with respect to change in the resistance of the metal.

$$R_H(T) = R_o(1 + \alpha_o T) \quad 3-4$$

where $R_H(T)$ and R_o are the resistance of the heaters at temperature T and $T = 0^\circ\text{C}$ respectively, and α_o is the temperature coefficient of resistance at 0°C .

The change in resistance of the micro heater with temperature for the micro heaters thickness of 2400 \AA and 400 \AA is shown in Figure 3-3. A linear curve was fitted with OriginPro 8 software. The slope of the resistance versus temperature for the 2400 \AA thick gold micro heater on a SiO_2 substrate was $0.10219 \text{ } \Omega/^\circ\text{C}$ with a standard deviation of $1.03 \text{ m}\Omega$. The calibration equation can be represented by

$$R_H(T) = 46.66491(1 + 2.1898^{-3}T) \quad 3-5$$

where the constant 46.66491 represents the resistance at temperature $T = 0^\circ\text{C}$ and 2.1898^{-3} is the temperature coefficient α_o at 0°C .

The slope of the resistance versus temperature for the 400 Å micro heater on a glass substrate was 6.181 Ω/°C with a standard deviation of 5.67 mΩ. The calibration equation is

$$R_H(T) = 319.11483(1 + 1.9369^{-2}T) \quad 3-6$$

where the constant 319.11483 represents the resistance at temperature $T = 0^\circ\text{C}$ and 1.9369^{-2} is the temperature coefficient α_o at 0°C .

The correlation estimates the average of the temperature profile across the micro heater element. However, this is based on the assumption that the heater is at a uniform temperature throughout the element. Typically thermal gradients can occur along the heating element, especially at the centre and at the sites of the connection pads as shown by Zhang, K.L. et al. [27]. They demonstrated that a thermal gradient was apparent by both modelling and by experimentally bringing their device to destruction and examining thermal sensitive coating. From Equation 3-6 we obtain an average overall temperature of the surface of the heater as the centre of the heater can be several degrees higher (approx 10°C [27]). For micro electronic applications the maximum elevation of the temperature of the fluid is approximately 60°C . There is a significant temperature gradient on the surface of the micro heater, however, with update in experimental facilities significant reduction in noise to signal can be achieved, which would allow for further reductions of power requirement and thus reduction in the temperature gradient.

The power input to the micro heater was correlated to the resistance of the heater. This resistance measurement could then be related to surface temperature using equation 3-6

determined from Figure 3-3. A plot of the surface temperature of the heater to the power input level is presented in Figure 3-4. A correlation between the surface temperature of the heater to input power can thus be determined. The calibration equation is linear and for the silicon oxide substrate can be represented as

$$T = 27.0964(1 + 0.3495P_{i(T)}) \quad 3-7$$

where $P_{i(T)}$ is the power input and T is the temperature.

Input voltages of 5V, 8V, 10V were used for the micro heaters that were fabricated on a silicon oxide substrate with a corresponding power of 499.5mW, 1.27W and 1.943W respectively. At these power levels the surface temperatures were 33.1 °C, 36.3 °C and 46.9 °C respectively.

For the micro heater that was produced on the silicon oxide substrate, the power consumption was extremely high (1.943 W for surface temperature of 46.9 °C), and would not be suited to MEMS applications. This is due to the high thermal conductivity of the silicon, which acts as a heat sink. This means that more power is required to increase the temperature of the fluid as heat is conducted away towards the silicon substrate. Thus, for a feasible device fabricated on silicon oxide, an anisotropically backside etch is required to reduce conduction in the substrate. The backside etch would reduce the thickness and provide thermal isolation between the heater and the silicon substrate. This would reduce the thermal losses and thus lower the power consumption required to get the same changes in temperature.

The calibration equation for the micro heater on the glass substrate is

$$T = 31.987(1 + 3.1317P_{i(T)}) \quad 3-8$$

where the $P_{i(T)}$ is the power input and T is the temperature.

The voltage input for the micro heaters that were fabricated on a glass substrate are 5V, 8V, 10V respectively that required a power input of 46mW, 112mW and 160mW and respectively. At these power levels the surface temperatures were approximated at 36.3 °C, 40.8 °C and 49.4 °C respectively. These are significantly lower due to the glass having a thermal conductivity that is two orders of magnitude lower than that of silicon. Again reducing the thickness of the substrate (thermally isolating the heater) would greatly reduce the power consumption. In future optimisation studies this could be carried out by etching in HF acid.

3.8 Summary

This chapter presented an overview of the development of micro heaters in this study. Fundamentals and governing equations were discussed. The experimental calibration of the micro heater for its variation of resistance with temperature was presented. The microfabrication process was presented along with the advantages and limitations of each step of the procedure. Tests were conducted at steady state producing a linear characteristic equation which correlates the temperature with power input. The effects of the substrate on the micro heaters and conclusions on further optimisation were discussed.

Chapter 4. Micro Flow Sensor

4.1 Introduction

In the previous chapters we examined the sensors for detecting thermal changes within microfluidic devices (i.e. micro thermocouples), and then examined the method of introducing a thermal pulse (i.e. micro heater) into the system. In this chapter we will discuss and analyse the integration of both, to create a method that can detect changes in flow rates in microfluidic systems.

Microfluidic devices are often required to manipulate small fluid volumes which require active sensing and control with fast response times and location selective precision. Such micro devices have found a wide range of applications in such industries as electronic cooling, pharmaceuticals, biomedical and combinatorial synthesis (rapid chemical analysis and high throughput screening). In these devices, accurate measurements of very small flow rates of the order of nanolitres per minute are required. Thus there is a growing need for micro flow sensors, as these utilize low power consumption, have mechanical stability, with high fabrication yield, high density integration and controlled functionality.

Flow velocity is a particularly difficult measurement to achieve, due to diversity of medium, condition and performance criteria, and the fact that it is not a scalar quantity. While precise flow measurement and control are generally demanded in these

applications, existing commercial sensors are inadequate for this purpose because of their large size, high cost and difficulties in interfacing with microfluidic devices.

There are several methods to sense flow that use a variety of physical phenomena. The physical principles that are commonly used for fluid flow sensing are;

- I. Mechanical (e.g. Volume, Force).
- II. Nuclear Physics (e.g. Nuclear Resonance, Isotope Injection)
- III. Optics (e.g. Laser Anemometry, μ PIV)
- IV. Electrodynamics (e.g. Induction, Conduction)
- V. Hydrodynamics (e.g. Thrust, Pressure Difference)
- VI. Thermodynamics (e.g. Heat Conduction and Convection)
- VII. Acoustics (e.g. Doppler Effect, Time of Flight)
- VIII. Stochastic (e.g. Correlations)

There have been several different micro fabricated flow sensors that have used these principles with varying levels of success, many being highly application dependent. Figure 4-1 shows a classification scheme for the family of flow sensors. Among the several methods of flow sensing, there are three promising principles for the measurement of flow; (1) laser anemometry, (2) differential pressure sensors, and (3) thermal flow sensors.

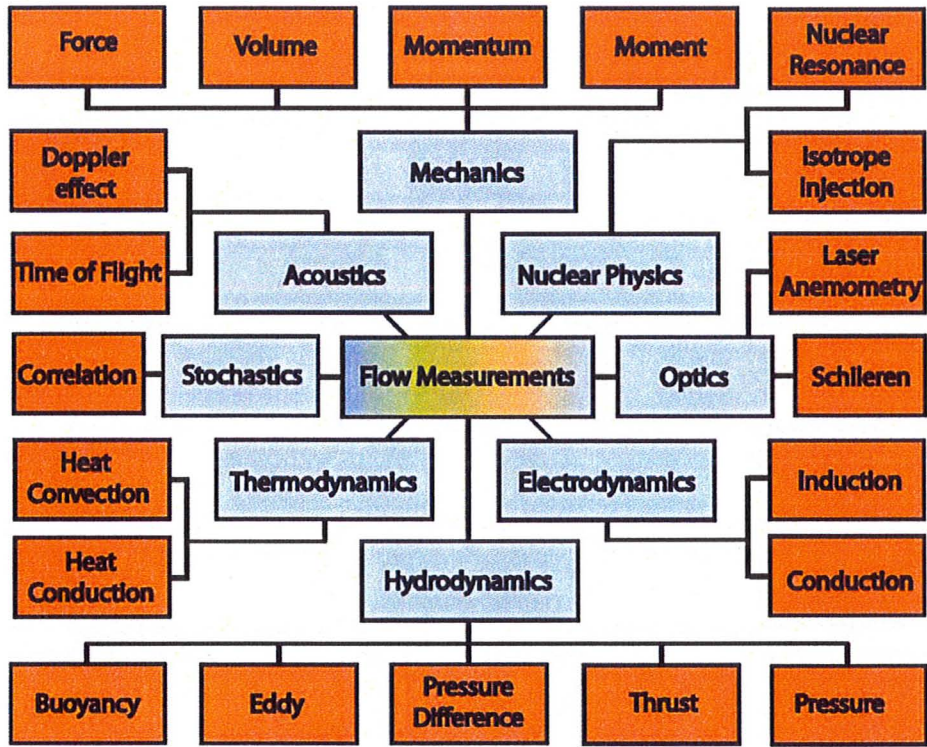


Figure 4-1: Classification scheme of physical principles of flow sensors, (adapted from [1])

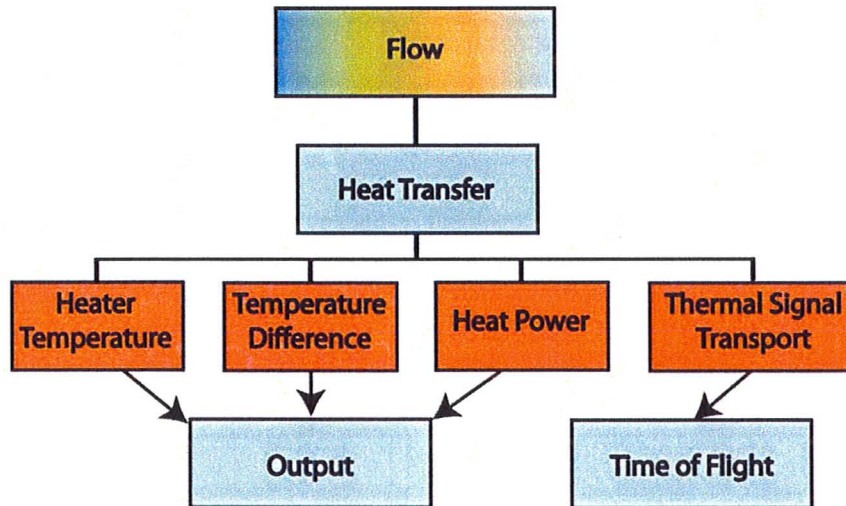


Figure 4-2: The three signal domains and signal transport of a thermal flow sensor, (adapted from [1]).

Laser anemometry techniques such as Micro Particle Image Velocimetry (μ PIV) are very accurate, non-intrusive and allow for the measurement of flow velocities. However the equipment is rather bulky, with high initial capital cost and the sensor is not incorporated within the device. Differential pressure detection techniques are very suitable for liquid flow measurements at high throughput levels, as the pressure loss along a microchannel is a linear function of flow velocity. However, at lower volume liquid flow applications (nl/min) and for gas flow, where pressure loss would be very small, the accuracy and detectability is significantly reduced. Thermal flow sensors are being more widely used because of their relative ease of incorporation into microfluidic devices. In its simplest form, the fluid flows over an impulse heat transfer source where the heat pulse is advected and detected downstream by a thermal sensor. The velocity can then be estimated using a velocity inversion algorithm.

The thermal flow principle was chosen for this study due to its mechanical and electronic circuit simplicity. It has the advantage of small size, fast response time, low power consumption and good interface with microfluidic devices. The method is compatible with standard electronic methods of data acquisition. The method is also highly sensitive at low flow rates. However, due to the heat pulse generated in these devices, it requires very short pulse times (order of ms) and good thermal isolation.

A thermal flow sensor generally consists of a heater and one or more temperature sensors. There are several modes of operation, depending on the way the heat transfer effects are evaluated. Figure 4-2 shows the general signal transport in thermal flow sensors. The

heater may be operated in a pulse heating mode or in a constant temperature mode while measuring the heating power/temperature or the response of the sensor to the input. There are three types of thermal flow sensors: hot film type, calorimetric type and time of flight type.

Hot film type sensors or hot-wire anemometry (HWA) measure the effect of the fluid flow on a sensor that is maintained at a temperature above the fluid. For these sensors, in the constant temperature mode, any increase in mass flow of the fluid in contact with the sensor requires an increase in electrical power in order to maintain the hot film at the same temperature. If operated in the constant power mode, the temperature of the hot film will decrease with an increase in mass flow rate which is then measured. These sensors types often suffer from offset and drift problems, thus reducing their accuracy.

Calorimetric principle is based on the temperature distribution around a heater, due to thermal dissipation caused by a flowing fluid. At no flow, the distribution would be symmetric; however, as the mass flow rate is increased there will be a skewing of the temperature distribution towards asymmetry away away the flow direction. The big disadvantage of this mode of operation is that it must run at a constant temperature, dissipating heat into the fluid that can be detrimental for biological applications.

Thermal time of flight (TTOF) sensors are those in which a heat pulse is generated and its heat trace is picked up by a downstream sensor at a known downstream distance. The time between the heat pulse generated and its detection can be used to determine the flow

velocity. This system is offset free and has less long term drift. A lower flow rates time of flight becomes difficult to detect the thermal signal.

4.1.1 Flow Sensor Design

The focus of the flow measurement was to research and develop a reliable flow sensor with a novel correlation technique. A micro thermal pulse calibration flow sensor was chosen because of its suitability to microfluidic applications, and in particular because it is suited to both harsh micro electronics (to tackle hotspots) and temperature sensitive biological environments. The method has several advantages. It can be implemented relatively inexpensively, as it is amenable to standard microfabrication techniques and can measure a wide range of flow rates with minimal disturbance to the flow.

A meandering resistance micro-heater was fabricated to create a temperature pulse in the moving fluid as described in the previous chapter. This thermal pulse was detected by a micro thermocouple located downstream of the heater. The flow sensor can be operated by using a novel correlation technique, and also in a time of flight mode. For time of flight mode the time between the pulse and its detection is used to calculate the velocity of the flow.

The device design, shown schematically in Figure 4-3, consists of a microheater to generate the thermal pulse and a micro thermocouple downstream at a fixed distance to detect the pulse. Pulsing the heater minimizes the heat input into the working fluid. Furthermore, it is also micro scalable, has a small foot print and can be easily integrated within microfluidic systems.

The existing research in the field is reviewed below, with an emphasis on micro flow sensors, the fundamental physics of flow phenomenon and the basic heat transfer equations are presented. The materials, working fluid, fabrication methods, and characterization results for the flow sensor are also presented.

4.2 Literature Review

The literature on micro flow sensors is divided into three sections: (i) thermal sensors, (ii) electrochemical sensors and (iii) others.

4.2.1 Thermal Flow Sensors

The first thermal flow sensor was proposed by C. C. Thomas in 1911. It was the first time that heat was used as a principle of detecting the mass flow rate in a macro channel. It consisted of a copper heater and two thermocouples that were placed in an open channel. The device was rather bulky, and disturbed the flow around where the heater was introduced, as shown in Figure 4-4.

The first thermal flow sensor that was designed on a silicon substrate was described by van Putten, A.F. P. and Middelhoek, S. [31] in 1974, where it operated under the anemometer principle. Kim, T.H. and Kim, J.K. [32] fabricated and characterized a gaseous micro thermal flow sensor with thin film thermocouples that worked under the calorimetric principle. It was fabricated on a quartz substrate using stainless steel masks and sputtering processes. The micro thermocouple consisted of alumel and chromel materials that make up a K-type thermocouple. The microchannels were fabricated from PDMS using Bakelite material as the master. The calorimetric technique requires a

relatively slow (~ 100 s) initial start up time to allow the device to come to thermal equilibrium. They correlated their device for flow rates in the range of 5 to 100 SCCM by applying 100 W for 10s and examining the effect of the flow rates on the asymmetry of the temperature profiles. They determined that there was an optimum distance between the sensors to achieve a maximum sensitivity of the output. Weiping, Y. et al. [33] developed a calorimetric based thermal flow sensor on a silicon substrate. It operated in a constant heat power mode, with operating voltages in the range of 3 to 18 V to limit the surface temperature of the heater to 60 °C as its design purpose was for biochemical sampling. It was able to measure flow rates in the range 10 to 700 $\mu\text{l}/\text{min}$. The micro channel on which the sensor operated was a capillary tube.

Rodrigues, R.J. and Furlan, R. [34] designed a pulsed micro flow sensor that was suitable for both gaseous and liquid flow measurements. It operated with both sinusoidal and pulsed signals and showed an improvement to similar sensors that were operated in a DC mode. They extended the range of measurements to low flows (5-25 mm/s). They determined an analytical model for a square wave pulsed time of flight that was in good qualitative agreement above velocities of 5 mm/s. The device was also operated in the calorimetric mode; however, no results were presented for this mode of operation.

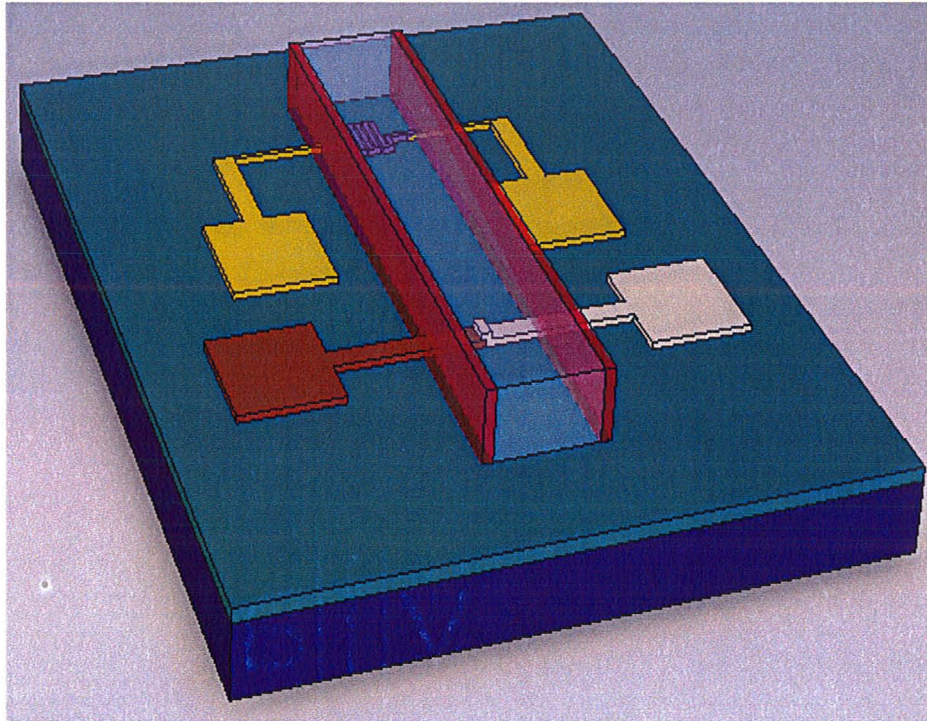


Figure 4-3: Conceptual schematic of a thermal micro pulse film flow sensor

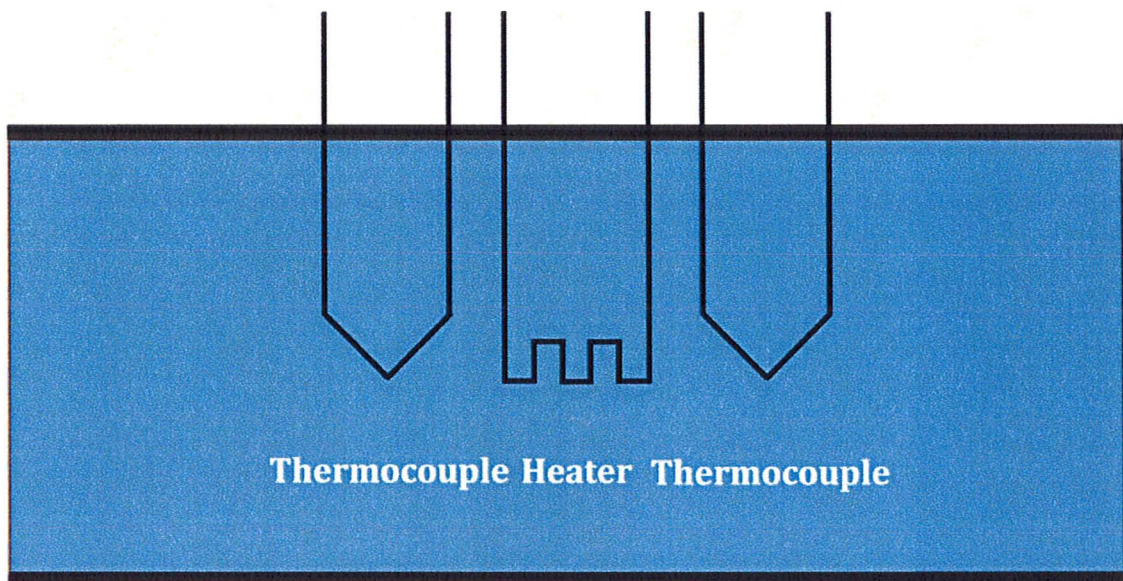


Figure 4-4: The first macro thermal flow meter proposed by C.C. Thomas in 1911, (adapted from [1]).

Hariadi, I. et. al. [35] used a simple one dimensional model to examine a thermal time of flight sensor. They used an equivalent electrical network in order to simplify the heat transfer problem. The model was applied to detect the effects of increasing the width of the heat pulse on the magnitude of the detecting sensor. They also presented a novel way of determining the flow velocity data by calibrating the device to the period of the output signal as a function of the fluid velocity. They found that their model was within 15% of the experimental results.

Ashauer, M. et. al. [36] fabricated and tested a thermal time of flight flow sensor that could measure both liquid and gas flows. Their sensor could operate by either time of flight or thermotransfer mode. Thermotransfer is where the fluid is heated and the corresponding temperature rise is measured. The heating of the fluid is restricted to within the boundary layer. By combining both sensing principles within the same device, a large dynamic range of operation was obtained. Their sensor was bi-directional and was able to detect flow velocities from 0.1 to 150 mm/s with resolution of 0.1mm/s.

Ashauer, M. et. al. [36] examined the influence of different fluids (water, oil, isopropanol) on sensor calibrations. As the thermal interaction occurs within the thermal boundary layer of the fluid, the response was dependent on thermal conductivity and the viscosity of the medium when operating in the thermotransfer mode. However, in the thermal time of flight mode, no effect on the medium was observed as the time of flight is directly correlated with the flow rate.

Buchner, R. et al. [37] designed a fabrication process for a thermal flow sensor where the change in temperature was detected using a thermopile. It was designed to operate in a high temperature environment. It was fabricated on a silicon substrate and was thermally isolated using a deep reactive ion etch (DRIE) technique. The thermopile consisted of 15 individual thermocouples. Each thermocouple had a sensitivity of $287 \mu\text{V/K}$ with an overall thermopile sensitivity of 4.3 mV/K . The flow rate was determined using the calorimeter principle. The response time to the thermopile was 2.61 ms and the sensor was able to detect flow rates up to $2 \mu\text{l/s}$, with a resolution of $0.2 \mu\text{l/s}$. Table 6: Overview of experimental and modelling of micro flow sensors.

Bruschi, P. et al. [38] designed an anemometric flow sensor for liquids that used only one temperature sensor. They examined the effect of settling time (time duration between measuring cycles) on both the constant temperature (CTA) and constant power (CPA) mode. They found that the CTA mode had a reduction of the settling time, and this was particularly evident at the lower flow rates due to sensor signal degradation as settling times are longer and the voltage values are not able to be sampled at steady state conditions. The sensor was meso in size (1.5 mm^2) and the probe was intrusive into a standard pipe, leading to small insertion losses. They developed a closed loop control sensor that could measure flow rates from $0.6 - 30 \text{ l/hr}$. They found that using a pulse mode improved the settling times and shortened the measurement cycle. The single temperature sensor avoids mismatching problem at the same time and had a sensitivity of 3.3 mV/K .

Author	Sensor Type	Flow range	Resolution	Fluid	Size [mm]	Notes
Kim, T.H. Kim J.K (2006)	Calorimetric	5-100 SCCM	5 SCCM	Gas	30 x 0.8	k-type thermocouples, sputtering fabrication
Weiping, Y. et al. (2005)	Calorimetric	10 – 700 μ l/min	~	Gas	~	Input power 3-18 V giving max temp 60 °C due to biochemical samples
Rogdriguez, R. J. Furlan, R. (2003)	Calorimetric & TOF	5 – 25 mm/s	5mm/s	Liquid/Gas	~	Analytical model, Measurement and Heater thermoresistive
Hariadi, I. et al. (2002)	TOF modeling	0.143 – 2.089 m/s	~	Liquid	~	model 15%+ pulse times 10ms - 30 ms
Ashauer, M. et al. (1999)	Thermotransfer & TOF	0.1 – 150 mm/s	0.1mm/s	Liquid/Gas	0.4 x 0.6	pulse power 50 mW, response time 2 ms
Bucher, R. et al. (2005)	Thermotransfer (Thermopile)	Up to 2 μ l/s	0.2 μ l/s	Liquid	4 x 2	Distance from heater 20 - 200 μ m, Thermopile Sensitivity 4.3 mV/K, consist 15 thermocouples individual sensitivity 287 μ V/k Response time 2.61
Bruschi, P. et al. (2004)	Thermotransfer (Anemometric)	0.6 - 30 l/hr	~	Liquid	1.5 x 1.5	Pulse mode -Improved settling times, shorter measurement cycle, temperature sensitivity 3.3 mV/K, Closed loop controlled.
Okulan, N. et al. (2000)	Pulse Thermotransfer	0.01 – 10 ml/min	~	Liquid	~	25% pulse cycle, 50 to 100 ms on times unamplified sensitivities of 60 mW at 10 μ l/min, single and Double pulse modes
Wu, J. Sansen, W. (2002)	Electrochemical (Oxygen)	1 – 15 μ l/min	1 μ l/min	Liquid	2 x 1.5	100 ms @2V
Poghossian, A. et al (2003)	Electrochemical (pH sensitive ISFETs)	0.1 – 0.6 ml/min	~	Liquid	14 x 16	Sensitivity 56 mV/pH
Harnet, C. K. et al. (2003)	Electrochemical (Conductivity TOF)	10 – 2000 nl/min	~	Liquid	~	1ms @ -110V
Mosier, B. P. et al. (2004)	Electrochemical (Conductivity TOF)	0.01 – 10 μ l/min	1 μ l/s	Liquid	0.14 x 3.126	Operating at high pressures (10000 psi)
Szekely, L. et al. (2004)	Optical(Fiber optic probe)	1-100 μ l/hr	0.3nl/hr	Liquid	External	Measured the meniscus of the liquid to determine flow rate response time 400

Okulan, N et al. [39] developed a pulsed mode thermotransfer micro flow sensor on a low stress silicon oxide bridge. The sensor was pulsed for intervals of 100 ms with a duty cycle of 25 %, with current input of 3 mA. The power input was limited as the temperature sensing element was for biological applications with a maximum working temperature of 60 °C. They observed for zero flow rate of the liquid there was an increase in output voltage of 100 mV within the first 30 s of operation. This drift occurred due to a continual increase in sensing element temperature (diffusion of the pulse) where the lack of forced convection resulted in a long thermal time constant. They also observed that the sensor detected changes of temperature due to the pulse, as initially there was a rise in temperature towards steady state temperature (at lower flow rates it does not reach steady state), after the trailing edge of the pulse. The sensor cools down significantly slower than the heating trailing edge of the heat pulse. Consequently, the detection sensor has additional offsets (accumulative initial conditions) as the cycles continue. They introduced a novel double pulse operation to reduce the effect of drift from the accumulative initial condition following each pulse. The double pulse regime forces the temperature to equilibrate towards the steady state temperature for the sensors. This can be shown in no flow rate condition as now there is no initial offset for the first 30 s. It increases the validity of the measurements even though temperature drift may still occur. They were able to detect a flow range of 0.01 to 10 ml/min and with the double pulse regime, and they had a repeatability of measurements of ± 1.49 %.

4.2.2 Electrochemical Flow Sensors

The initial electrochemical time of flight flow sensor was proposed by Wu, J. and Sansen, W. [40]. They used a molecule tracer (oxygen) instead of a thermal tracer. The advantage here was that the molecule tracer cannot diffuse into the walls, thereby eliminating the effect of conduction through the walls. An electrochemical cell was used to produce oxygen that was detected by a downstream cell. The operating range was between 1 to 15 $\mu\text{L}/\text{min}$, and the small operating range was due to the sensitivity of the oxygen sensor.

A time of flight flow velocity sensor using Ion-sensitive field-effect transistors (ISFETs) was developed by Poghossian, A. et al. [41]. The sensor consisted of an ion generator and two pH sensitive ISFETs that were located downstream. It operated under a time of flight principle that detected changes in pH. The ISFET output signal changes were typically about 180-200 mV. The pH sensitivity for the ISFET was 55-58 mV/pH for change of pH of approximately 3.2-3.5. They calibrated their device in the range 0.1 to 0.6 ml/min. Due to the fast response time of ISFETs there is a potentially large dynamic measurement range from $\mu\text{m}/\text{s}$ to m/s. The biggest drawback is the fact they are relatively large, (sensing area of 0.5 x 1 mm for each ISFET) and so will have low spatial resolution.

A conductivity pulse time of flight flow sensor was developed by Harnett, C. K. et al. [42]. The flow rate was determined by measuring the time of flight of an ion pulse introduced by electrolysis at a pair of electrodes inside the channel. The advantages of this system are that the ion pulse cannot diffuse into the walls reducing the need for thermal isolation, and it is insensitive to viscosity variations. However it requires high-

voltage inputs, and it can only operate in weakly buffered solutions for slow flow rates because the ion pulse would disperse away before being detected and are subject to DC electronic drift. They operated the sensor over a flow range of 10-2000 nL/min.

Mosier, B. P et al. [43] further developed the concept of a conductivity pulse time of flight sensor and in 2004 patented it as a composition pulse time of flight mass sensor. The device was of similar design and operating principle to Harnett, C.K. et al. [42]; however, they extended the operating range from 1 nL/min to 10 μ L/min. It was also claimed it operated under pressure conditions up to 10000 p.s.i, with the limitation being the material of the micro channel. The device size was minimized to 0.14 x 3.126 mm.

4.2.3 Other Techniques

A novel optical method to determine flow rates in the order of nl/s was developed by Szekely, L. et al. [44]. Who developed a method that could accurately measure in operating range of 1-100 μ l/hr with an extremely high resolution of 0.3 nl/s. They used a fibre optical probe technique that involved measuring the meniscus of the fluid. The disadvantage of this technique is it requires a meniscus (only operates at beginning of flow) and the device is not in situ, so requires external bulk equipment.

4.3 Fundamentals and Governing Equations

In the previous chapters we examined the principles behind thermal sensing and of the micro pulse heater. Here we incorporate both principles and examine the fundamentals and governing equations of flow measurement. The many different factors that need to be considered, in order to get an accurate mass flow measurement, including the heat

transfer to the fluid, heat dissipation of the pulse and profile quality of the pulse are examined.

Thermal flow sensors involve three energy domains: flow, thermal and electrical. The interaction between the electrical and thermal domains to produce the heating pulse and detect it has been covered in chapter 3 and chapter 2 respectively. The flow and thermal interactions between the fluid and the sensor will now be discussed.

The flow is governed by the Navier-Stokes equations while the thermal energy exchange is governed by the thermal boundary layer equations. The heat is conducted from the surface of the resistance heater to the fluid, where it is advected downstream and detected by a micro thermocouple.

The overall heat generated by the heater is transported in four ways, namely the diffusion heat transfer within the fluid q_{fluid} , the substrate q_{solid} , the forced and free convection q_{conv} and radiation q_{rad} .

$$q_{total} = q_{fluid} + q_{solid} + q_{conv} + q_{rad} \quad 4-1$$

The radiation losses, q_{rad} is relatively small in the standard environment and temperature, and thus can be neglected. Free convection can be neglected due to the small thermal gradient within the operating conditions. However, the forced convection due to fluid flow is of significant importance. The Navier-Stokes equations can be simplified by assuming laminar flow and neglecting buoyancy forces. The heat transfer to the fluid is determined by diffusion and forced convection mechanisms. The rate of change of temperature of a fluid can be determined using an energy balance.

For a one dimensional case it is given by [45];

$$\frac{\partial T}{\partial t} = \alpha \frac{\partial^2 T}{\partial x^2} - V_x \frac{\partial T}{\partial x} \quad 4-2$$

where T is the temperature as a function of position x, time t, and α is the heat diffusion coefficient given by

$$\alpha = \frac{k_f}{\rho C_p} \quad 4-3$$

where α [m²/s] is the diffusion coefficient, k_f is the thermal conductivity, ρ is density and C_p is the specific heat capacity of the fluid. The first term is the transient rate of change of temperature. On the right hand side of equation 4-2, the first term is associated with diffusion while the second term is associated with forced convection. Equation 4-4 is a transient diffusion-convection heat transfer equation that can be solved using a circuit modeling approach [35].

The heat transfer due to conduction within the substrate is governed by [45];

$$\frac{\partial T}{\partial t} = \alpha \left(\frac{\partial T}{\partial x^2} + \frac{\partial^2 T}{\partial y^2} + \frac{\partial^2 T}{\partial z^2} \right) \quad 4-4$$

Equation 4-4 again can be solved using an equivalent electrical network, consisting of elements of thermal resistance and capacitance [35].

The thermal energy exchange between the sensor and the fluid is governed by the thermal boundary layer equations. The heat transfer between the surface of the heater and the fluid is proportional to the temperature gradient within the boundary layer and can be expressed using an average heat transfer coefficient h as [45]

$$h = k_f \frac{\partial T / \partial y}{T_s - T_\infty} \quad 4-5$$

where k_f is the thermal conductivity, T_s is the surface temperature and T_∞ is the ambient temperature of the fluid.

For a laminar boundary layer with an unheated starting length the average Nusselt number, Nu_x can be expressed as [46]

$$\overline{Nu}_x = \frac{hL}{k_f} = \frac{0.332 Re_x^{1/2} Pr^{1/3}}{\left[1 - (x_0/x)^{3/4}\right]^{1/3}} \quad x > x_0 \quad 4-6$$

where Re_x and Pr are the Reynolds number and the Prandtl number respectively and x_0 is the unheated starting length from the channel to the heater.

The heat transfer coefficient can be determined by [45]

$$q = hA\Delta T \quad 4-7$$

where q can be estimated from [45]

$$q = mc_p\Delta T \quad 4-8$$

where m is the mass flow rate of fluid, c_p is the specific heat of the fluid and ΔT is the change in temperature.

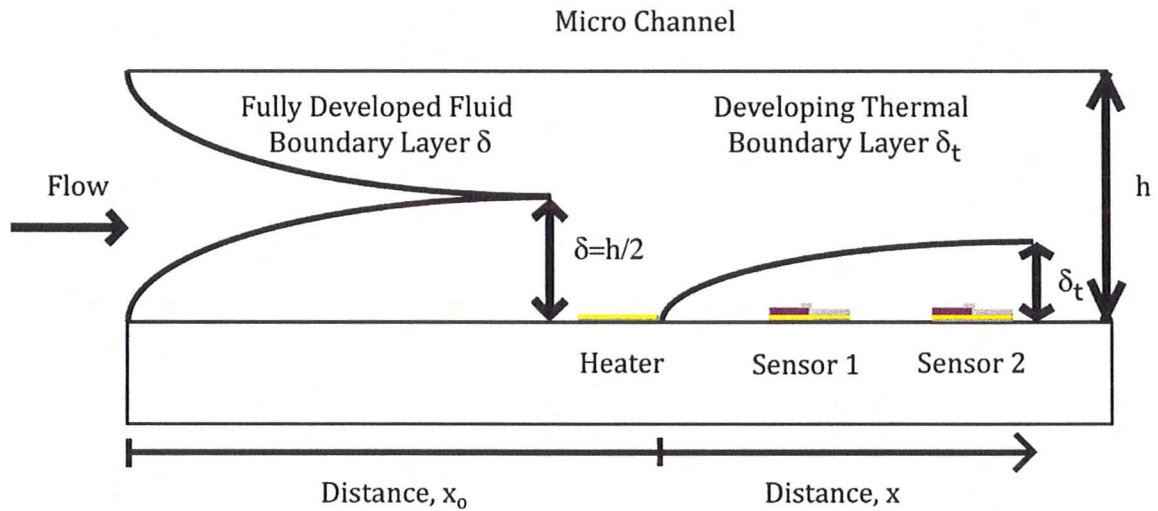


Figure 4-5: Boundary layer for micro channel where the fluidic boundary layer is fully developed and the thermal boundary layer is developing after the heater

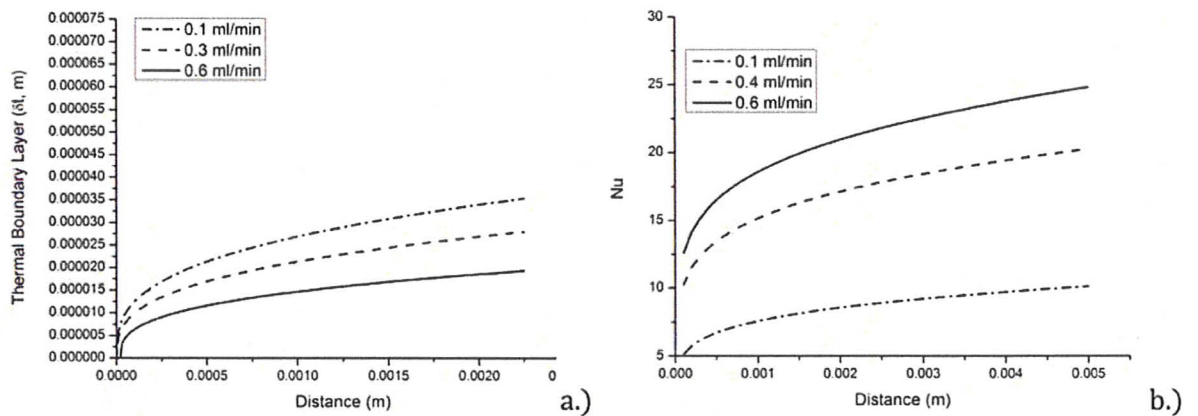


Figure 4-6: a.) Thermal boundary layer with distance from the heater is reducing with increase flow rate, b.) Nusselt number with distance from the heater, the Nusselt number is increasing with flow rate

The fluid is fully developed, and thermal laminar boundary layer thickness can be represented by the following equation [46]

$$\delta_t = \frac{\sqrt{\frac{3\alpha x}{U_{max}}}}{\sqrt{\frac{3}{20}\frac{\delta_t}{\delta} - \frac{3}{280}\left(\frac{\delta_t}{\delta}\right)^3}} \quad 4-9$$

For fully developed flow in a channel $\delta = h/2$, where h is the channel height. Substituting into equation 4-9

$$-\frac{3}{35}\frac{\delta_t^5}{h^3} + \frac{3}{10}\frac{\delta_t^3}{h} = \frac{3\alpha x}{U_{max}} \quad 4-10$$

The using Equation 4-10 thermal boundary layer can be solved using an iterative method, and is plotted in Figure 4-6. From Figure 4-6 a.) it is clear that with decrease in thermal boundary layer with increase in flow rate. From Figure 4-6 b.) it is clear that there is increase Nusselt number with increase in flow rate. The amount of heat is constant between the different flow rates. With increase in flow rates the thickness of the thermal boundary layer is reduced, thus reducing the area in which the heat transfer occurs. The thermal energy is shared between a smaller area of fluid and thus the sensor detects more thermal energy.

A simple one dimensional order of magnitude model was used to determine the effect of substrate material on heat transfer from the heater to the fluid (convection) and substrate (conduction, diffusion). The diffusion length scale was determined as

$$l \sim \sqrt{\alpha t} \quad 4-11$$

and the diffusion time scale is

$$t_{diffusion} \propto \frac{l^2}{\alpha} \quad 4-12$$

The convection time scale is estimated as

$$t_{convection} \propto \frac{l}{U_{conv}} \quad 4-13$$

If we assume

$$U_{conv} \sim U_{mean} = \frac{\dot{v}}{A} \quad 4-14$$

we have a first approximation of the effect of the substrate on the convection of the heat pulse by the fluid.

Table 7 shows the ratio of the convective to diffusion time scales for a silicon substrate for different flow velocities and distances between the heater and sensor. The corresponding ratios for a glass substrate are shown in Table 8. It is clear from Table 7 and Table 8 that for a silicon substrate the effect of diffusion through the substrate dominates, and the convection of the heat pulse by the flow would be small, making detection of the pulse by the sensor due to the flow difficult. For a silicon oxide layer it can be seen that again the diffusion is dominant. Even at the higher velocity of 5.56×10^{-2} m/s, the diffusion through the substrate is higher than the convection through the working fluid. Thus, the dominant mode of heat transfer would be that of diffusion through the substrate. For the glass substrate, the diffusion rate through the substrate and the working fluid is less than that of the time scale for forced convection. For the operating velocity

range of 1.11×10^{-3} to 7.8×10^{-2} m/s, it can be seen that the thermal pulse can be detected.

However, below this velocity range, it is harder to determine the dominant effect.

Table 7: The ratio of time taken for heat pulse to be detected due to the effect of convection only, to the time taken for the heat to diffuse through the substrate to reach sensor at known distance downstream for a silicon substrate.

		Convection/Diffusion Time Scale Ratio			
		Silicon			
Distance [m]		3.45×10^{-4}	5.35×10^{-3}	2×10^{-3}	3×10^{-3}
Velocity U_{conv} [m/s]	0	0	0	0	0
	1.11×10^{-3}	208.18	124.49	35.93	23.91
	5.56×10^{-3}	41.56	26.81	7.19	4.78
	1.1×10^{-2}	21.01	13.56	3.63	2.42
	3.3×10^{-2}	6.99	4.52	1.21	0.81
	4.44×10^{-2}	5.20	3.35	0.9	0.6
	5.56×10^{-2}	4.16	2.68	0.72	0.48
	6.7×10^{-2}	3.44	2.23	0.6	0.3
	7.8×10^{-2}	2.96	1.91	0.51	0.34

Table 8: The ratio of time taken for the heat pulse to be detected due to the effect of convection only, to the time taken for the heat to diffuse through the substrate to reach sensor at known distance downstream for a silicon substrate.

		Convection/Diffusion Time Scale Ratio			
		Glass			
Distance [m]		3.45×10^{-4}	5.35×10^{-3}	2×10^{-3}	3×10^{-3}
Velocity U_{conv} [m/s]	0	0	0	0	0
	1.11×10^{-3}	0.28	0.18	0.048	0.032
	5.56×10^{-3}	0.06	0.04	0.001	0.007
	1.1×10^{-2}	0.03	0.018	0.005	0.004
	3.3×10^{-2}	0.01	0.0061	0.002	0.001
	4.44×10^{-2}	0.007	0.0045	0.0012	0.0008
	5.56×10^{-2}	0.005	0.0036	0.0009	0.0006
	6.7×10^{-2}	0.0047	0.0031	0.0008	0.0005
	7.8×10^{-2}	0.004	0.0025	0.0007	0.0004

4.3.1 Modes of operation

The flow sensor developed herein can either be operated in the time of flight mode or by a simple calibration method correlating the change in voltage signals to the mass flow rate of the working fluid.

4.3.2 Time of flight

For the time of flight mode, the deformation of the heat pulse during advection due to diffusion and convection needs to be considered. The response curves of thermocouples along the flow direction will have different shapes and will be shifted along the time

scale. The first thermocouple will detect a bell shaped pulse; however, by the time the pulse has reached the second thermocouple, the amplitude will have decreased with the width of the curve spread, due to diffusion and dissipation of the heat pulse, as shown schematically in Figure 4-7. The time shift will be inversely proportional to the flow velocity.

For time of flight, the analytical solution for a pulse signal with input strength q_0 is given by [35]

$$T(x, t) = \frac{q_0}{4\pi\kappa t} e^{-\frac{(x-ut)^2}{4\alpha}} \quad 4-15$$

where κ is the thermal conductivity of the fluid and q_0 is the initial heat transfer input to the system. Knowing the distance between the thermocouples, the flow velocity can be calculated by determining the time difference between detection of the pulse at each location. The simplest case where convection dominates (i.e. high flow rates) gives us the traditional time of flight equation:

$$u = \frac{x}{t} \quad 4-16$$

However at smaller flow velocities where diffusion may have an effect. Solving equation 4-15 we have time constants such that [35]

$$\tau = \frac{-2\alpha + \sqrt{4\alpha^2 + u^2 x^2}}{u^2} \quad u \neq 0 \quad 4-17$$

$$\tau = \frac{x^2}{4\alpha} \quad u = 0 \quad 4-18$$

4.3.3 Pulsed thermotransfer calibration

The thermotransfer principle is that the heat loss from the micro heater source to the fluid will increase with the flow rate, thereby giving greater voltage amplitude of the thermocouple response with increasing flow velocities. There are two benefits of this technique; one is scalability and the second is no time domain information is required, after initial calibration is done. There is, however, a drawback to this method. The calibration curves are dependent on the working fluid properties, and thus each different working fluid will require a new calibration. However, when calibrating one device, due to the nature of the micro fabrication processes, several thousand of the same sensors are calibrated in parallel.

Our calibration technique involves correlating the change in voltage detected by the thermocouple to mass flow rates. This method has the advantage that once it is calibrated, then very little external hardware is required for post processing. This is in contrast to TOF technique that requires extra hardware for the data to be time stamped accurately. Here, the amplitude between the different pulses is calculated and correlated for different flow rates to obtain a calibration curve.

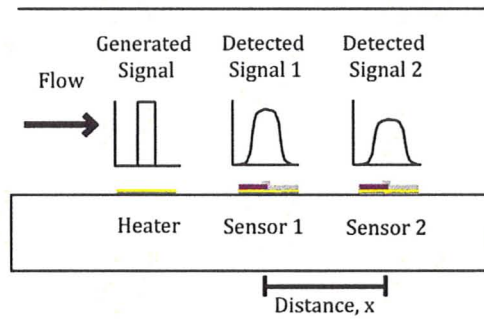


Figure 4-7: Schematic of time of flight sensor, thermal pulse introduced, and detected downstream by two sensors.

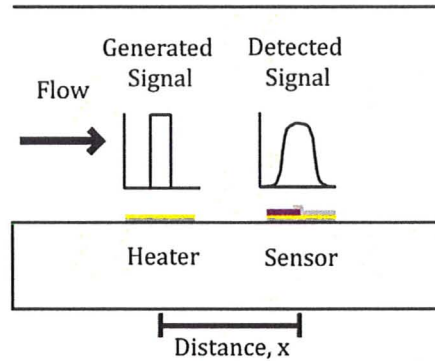


Figure 4-8: Schematic of thermotransfer calibration technique, thermal pulse introduced, and detected downstream, where the amplitude of the responses are correlated with mass flow rate

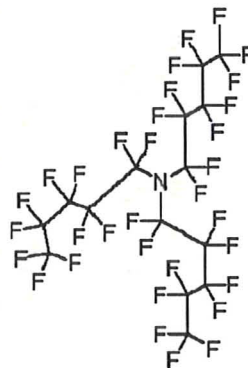


Figure 4-9: Molecular Structure of FC 70(copied from [56])

It requires only a heat source and a micro thermocouple, (as temperature drift is minimal, a second sensor becomes redundant) thus reducing its foot print, which is very attractive, see Figure 4-8. This is theoretically true for the time of flight sensor, however it is more complex to correlate an electrical thermal signal (heat pulse) with an electrical signal (thermocouple voltage response) as they have different magnitudes, than it is to correlate between two similar electrical signals (two thermocouples responses), to work out time shift information.

Even though the calibration correlations are dependent on the working fluid properties and operating conditions, a single calibration reproducible to thousands of other devices can be bulk micro machined.

4.4 Materials and Working Fluid

The materials for the sensor substrate, sensor, and microchannel were selected based on the micro flow phenomenon, their thermal and electrical properties and feasibility for microfabrication. The micro channel fabrication materials and working fluid are now discussed.

4.4.1 Working Fluid

The working fluid has a significant impact on the performances of the micro flow sensor. The main drawback of PDMS is that it is hydrophobic which means it restricts the flow of water in the channels. Many different temporary and semi permanent techniques to make the surface of PDMS hydrophilic have been investigated and are reviewed in Makamba, H. et al. [50]. Therefore the main requirements for fluid selection was that it

wets the PDMS surface and hence the microchannel can be filled and that it has high heat transfer coefficients in order to have a strong thermal signal from the heater to the thermocouples.

Water, Methanol, and FC 70 were all considered as the working fluid. A comparison between their physical properties under standard ambient temperature and pressure conditions is presented in Table 9. Water is widely used in microfluidics as it is biologically compatible. Although it has a high specific heat, its large latent heat capacity means that long pulse times would be required to get strong thermal signals. Most importantly PDMS is hydrophobic so the water would be restricted in the PDMS channels. Methanol on the other hand makes PDMS wettable. Initial testing of the micro flow sensors within the microchannel were undertaken using 3M™ Fluorinert™ Electronic Liquid (FC 70) as the working fluid. FC 70 is a clear, colourless, non-flammable, low-odour and fully-fluorinated liquid. It is compatible with sensitive materials, leaves no residue upon evaporation, and is both thermally and chemically stable. Its high dielectric strength and conductivity makes it excellent for heat transfer for thermal management applications. Its chemical structure is $(CF_3(CF_2)_4)$. FC 70 has a boiling temperature of 215 °C under standard atmospheric conditions. The molecular structure of FC 70 is shown in Figure 4-9.

Table 9: Physical properties of different fluids under standard ambient temperature and pressure conditions.

Properties	Water [52]	Methanol [52]	50% Methanol 50% Water	HF70 [56]
Chemical Structure	H ₂ O	CH ₃ OH	H ₂ O+ CH ₃ OH	(CF ₃ (CF ₂) ₄)
Molecular Weight (g/mol)	18.016	32.04	161.4	820
Density (kg/m ³)	1000	795.77	~ 918.52	1940
Dynamic Viscosity (Pa/s)	0.001003	.000525	~ 0.00076	0.024
Thermal Conductivity (W/m ² K)	0.595	0.196	~ 0.395	0.070
Boiling Point (°C)	100	64.7	~ 82.3	215
Specific Heat (kJ/kgK)	4.184	2.554	~3.390	1.1
Latent Heat (kJ/KgK)	2260	1100.2	~ 1680	69
Dielectric Constant	80	33.6	~ 56.8	1.98

However, due to the low thermal conductivity of FC 70, a high power consumption was required for detectable thermal pulses as conduction through the substrate materials was dominant. With further thermal isolation of the heater from the substrate FC 70 would be ideal for micro electronic cooling applications.

In this study, the micro flow sensors were tested using a mixture of 50% of Methanol and 50% of water as the working fluid. Methanol is miscible in water and also enables wetting of the mixture in PDMS microchannels. The mixture is clear, colourless,

compatible with sensitive materials, and its high dielectric strength and conductivity make it excellent for heat transfer for thermal management applications. It has an approximate boiling temperature of 82.3 °C under standard atmospheric conditions. A 50% Methanol and 50% water mixture was chosen as it allowed the liquid to flow through the channel.

4.5 Microfabrication Process

The micro flow sensor microfabrication is a three part process. It consists of:

- 1) micro thermocouple and heater fabrication,
- 2) microchannel fabrication,
- 3) system integration.

4.5.1 Fabrication process

The fabrication process for the flow sensor involves the integration of both the micro thermocouples and micro heater within a microchannel.

There are two changes to the fabrication procedure of the micro thermocouples described in Chapter 2; firstly, the substrate is glass instead of silicon oxide and secondly the micro heater is integrated within the fabrication process by incorporating it in the second mask design, (see Appendix C).

A 60 Å layer of chromium followed by a 200 Å layer of gold was deposited on the glass as a plating base, shown in Figure 4-10 (a). Subsequently, the wafer was plasma oxidized

and a thick positive photoresist (AZ P4620) was spun cast. The first mask containing one leg of the thermocouple was exposed and developed, (see Figure 4-10 (b)).

Constantan was electroplated onto the exposed gold surface (Figure 4-10 (c)). A thin S-1808 photoresist was spun cast. The second mask containing both the micro heater and the micro thermocouple was exposed and developed, (see Figure 4-10 (d)). At Figure 4-10 (d), the process flow is divided into a section through the micro thermocouple and a second through the micro heater. The gold and chromium layers are etched away to reveal the micro heater. Again thin S-1808 photoresist was spun cast and the final lift off mask was exposed and developed, to fabricate the second leg of the thermocouple. A 60 Å layer of chromium followed by a 1200 Å layer of Platinum was deposited on the substrate, shown in Figure 4-10 (e). Chromium acts as an adhesion layer between the platinum and the substrate. The platinum was released, upside down, in a bath of acetone.

Figure 4-10 (f) shows the completed individual fabricated micro-thermocouple and micro-heater. Fabricating both the micro heater and the micro thermocouples together on the same substrate provides the framework for the micro pulse film flow sensor, as shown in Figure 4-10 (g). The completed fabricated micro pulse film flow sensor is shown in Figure 4-11.

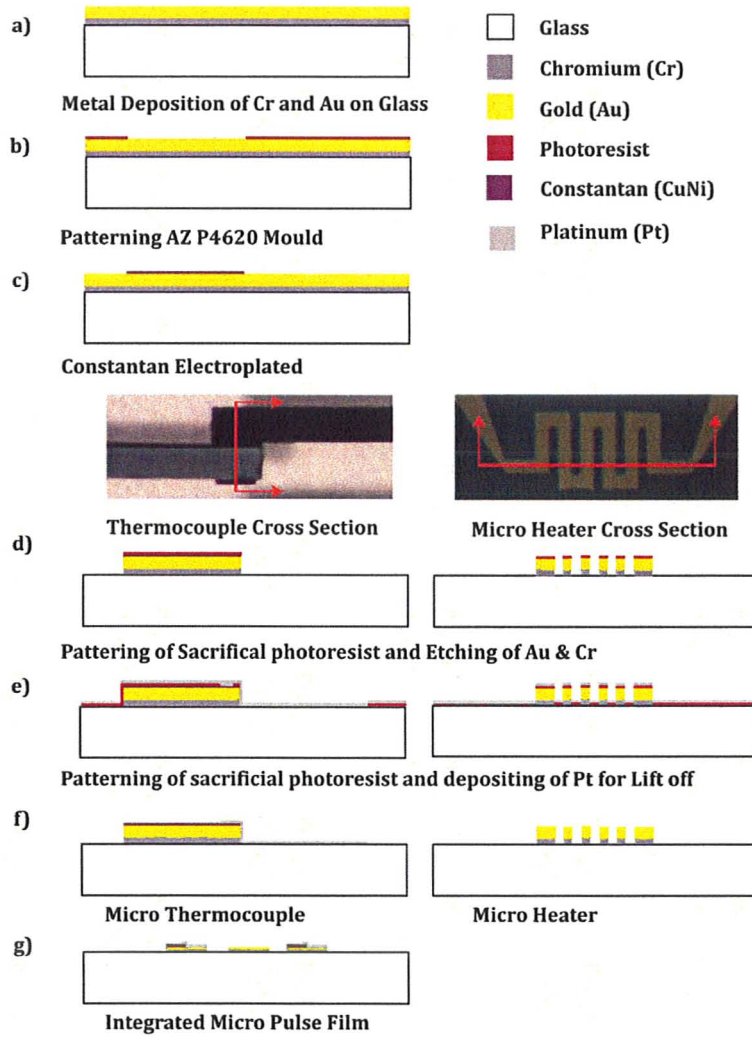


Figure 4-10: Fabrication process flow for the integrated micro pulse film

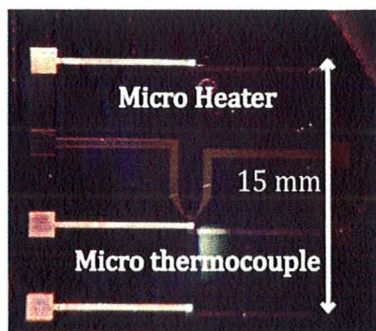


Figure 4-11: Completed fabricated pulse film flow measurement device on SiO_2 substrate

4.5.2 Fabrication of micro channels

Traditionally microfluidic devices were fabricated using silicon and glass techniques. These tried and tested techniques are expensive and time consuming and require the use of clean room facilities, reducing their usefulness for rapid evolution of prototypes [47]. Fabrication for microfluidic technologies using Poly(dimethylsiloxane) (PDMS) is preferred due to its ease of fabrication, low cost, quick throughput and flexibility in application. PDMS is a silicone-based material supplied in two components, a base and curing agent. The base is made up of short chemical chains containing the vinyl groups ($-\text{CH}=\text{CH}_2$) which, when mixed with the curing agent that is made up of long chains containing hydrosiloxane (Si-H) groups become cross-linked and solidifies [47, 48].

PDMS devices are fabricated by soft lithography where the pre-polymer mixture is cast on a master (or mould) replicating its features. Subsequently, the pre-polymer is polymerized using heat to produce an elastomer. The PDMS pre-polymer is poured and conforms to the features, see Figure 4-12. It is inert, non-toxic making it biocompatible, it is electrically and thermally non conductive and has low fluorescence. Thus it will not interfere with fluorescence as it is transparent in the visible/UV region so optical detection methods are possible. However it is hydrophobic but it can be made hydrophilic by surface modification techniques [49; 50; 51].

4.5.3 Microchannel Fabrication

The microfluidic channel was fabricated by casting polydimethylsiloxane (PDMS) on top of an SU-8 (MicroChem Corp.) mould which was patterned photolithographically to

define the microchannel structure. A silicon wafer was plasma oxidized for 1 min at 50 W to improve the adhesion properties. Su-8 100 was spun cast at 3000 rpm on a silicon wafer for 30 sec to spread a 100 μ m thick layer. The resist was soft baked for 10 minutes at 65 $^{\circ}$ C, and for 30 minutes at 95 $^{\circ}$ C. Subsequently the sample was exposed for 90 seconds at 7.2 mJ/sec using a negative microchannel mask. Following exposure, the sample was post baked for 1 minute at 65 $^{\circ}$ C, and for 10 minutes at 95 $^{\circ}$ C. A 1:10 curing agent to base PDMS pre-polymer mixture was cast on the SU-8 moulds to produce a replica. The cast PDMS pre-polymer was cured at 65 $^{\circ}$ C for 1 hour. The cured PDMS elastomer was peeled off from the Su-8 mould, and holes were punched in them in order to attach glass tubing for the inlet and outlet of the channel, see Figure 4-12 for process flow.

4.5.4 System Integration:

The microfluidic channel was integrated to the micro pulse flow sensor by adhering it to the substrate using a combination of plasma oxidization and liquid PDMS as glue, see Figure 4-12. Both the PDMS channel and the silicon substrate were plasma oxidized for 1 minute at 50 W. A 1:3 curing agent to base mixture of PDMS was spun cast on a glass slide at 3000 rpm for 1 minute. The microchannel was placed gently onto the spun PDMS, to attach the thin film of PDMS only in the elevated regions, preventing the channel being clogged. The PDMS elastomer with microchannels was subsequently aligned using alignment markings on the substrate with the thermocouples and micro heater. Then a 1:3 curing agent to base mixture of PDMS pre-polymer was poured on the microchannel border and baked at 150 $^{\circ}$ C. The PDMS pre-polymer on the microchannel

boundary bonded the microchannel with the underlying substrate. This prevented leakage problems [51].

4.6 Experimental Setup

The primary function of the test rig was to characterize the micro pulse flow sensor. The test setup is shown schematically in Figure 4-13. This test setup allows the determination of the flow rate in potentially three different modes; time of flight, temperature difference, and calibration.

The test facility consists of an AFG 3022B function generator [Tektronix], with amplifier [Harshaw NV-26], 54624A Oscilloscope [Agilent], Z80210 syringe pump [KD Scientific] ice bath, low band pass filter [Wavetek dual Hi/Low filter model 852], 34401A multimeter [Agilent] with data acquired using a GPIB-USB-HS and LABVIEW software to record the transient measurements. The voltage output from the micro pulse flow device thermocouples were measured using two 34401A multimeter which had a resolution of $1\mu\text{V}$ and accuracy of $\pm 5\mu\text{V}$.

Accurate measurement of the thermocouple response voltage requires either amplification of the signal or a data acquisition system sensitive enough to measure low voltage levels, since here we are trying to identify the signal peak of a very low voltage signal (mV) of the thermocouple. Amplification brings the voltage signal into range of detection of the data acquisition; however, amplification augments both the noise and the signal. Power input to the micro heater was generated by the AFG 3022B function generator which has a maximum frequency of 250 MHz with $5V_{\text{p-p}}$. For higher voltages, an amplifier was

required. This amplifier increased the noise on the power input (see Figure 4-14). To reduce the noise associated with the amplifier it was powered up for a period of 45 minutes before testing, which gave a slight reduction of the noise (machine required time in order for operating temperature stabilization).

Tektronix ArbExpress software was used to design the input pulse signals, which were entered into the AFG 3022B function generator. Different duty cycles, amplitudes, and pulse durations were examined, as well as novel changes in amplitude curves and pulse duration curves.

Since noise can be significant and affect the results, all sources of noise were examined throughout the experiment using a 4 channel 54624A Oscilloscope [Agilent] which had a sampling speed of 500 MHz. Careful attention was paid to the electrical connections. For example, long thermocouple wires can act as antennae that pick up noise and ambient interference such as electromagnetic interference (EMI) and radio frequency interference (RFI). All wires and instruments were shielded using coaxial cables. Initial voltage measurements were acquired without filters and were converted into the frequency domain by using a Fast Fourier Transform (FFT) algorithm. Most of the interference was found to be above the 10 Hz (60 Hz (electric power noise) to 10 kHz) range and a hardware low pass filter [Wavetek dual Hi/Low filter model 852] was used with a 20 dB flat amplification. 10nF capacitors were placed between the lead wires as they entered the low pass filter in order to short the AC noise signal to ground. This 10 nF capacitor

resistor has the effect of reducing the noise at the (~10 MHz) MHz range, where the smaller the capacitor rating the higher the frequency in which the noise is reduced.

A Z80210 syringe pump was used to control the flow rates of the fluid. Its operating range was from 0.1 μ l/min to 0.7 ml/min. The flow rate was limited due to PDMS sealing problems that were caused by the higher pressure to drive the higher flow rates. The fluid in the channel was allowed to remain at steady state for 45 minutes prior to taking any measurements. After each test the fluid was pumped for a period of at least one minute and was again allowed to attain steady state for 5 minutes. The order in which the instruments were controlled was as follows. First the syringe pump was turned on, and then the function generator and pulses were introduced into the system. After 30 seconds (in order to get good signal conditioning) the labview control program recorded the response of the thermocouple to the heat pulse.

4.6.1 Signal Conditioning

The power was input using a function generator (AFG 3022B), with a max output of 5 V. It is shown in Figure 4-18 that for a power input of 5V, the signal is barely detectable by the thermocouple (response has large signal to noise ratio). To increase the signal strength, the voltage input needed to be increased. The function generator is not able to accomplish this. The low voltages were set on the function generator, in mV range, and were amplified using a Harshaw, NV-26 amplifier. The input voltages from the micro heater are shown in Figure 4-14, where it can be observed there are high levels of noise on the signal for each input (5, 8 and 10 volts). As there are high levels of noise on the

signal, the number of samples that were needed so the true voltage amplitude maximum was measurement, was in the range of 3 sets of 30 samples.

The measured voltage reading from the thermocouples are presented in Figure 4-15 along with the input voltage of the micro heaters. Three graphs using different pulse modes for the heater are presented for a constant mass flow rate of 0.3 ml/min. Figure 4-15 a) is a single pulse operation mode at 10 Volts. It can be seen that the peaks of the thermocouple response are very distinct and have consistent amplitude. There is no rise in the ambient conditions of the working fluid after each pulse cycle. Figure 4-15 b) is the output from a multiple pulse operation, where the input voltage is changed for each pulse (5V, 8V and 10V). It is shown that with the change in input voltage the output response changes similarly. The relaxation time for the heated working fluid after each pulse to return to ambient temperature is fastest in this mode. Figure 4-15 c) is of a multiple pulse operation where the pulse time is changed (50 ms, 100 ms and 150 ms). Here, with an increase of the pulse time, the output voltage of the detecting sensor increases. The detected voltage signals are now more prominent. Again the ambient working fluid temperature returns to ambient after each cycle.

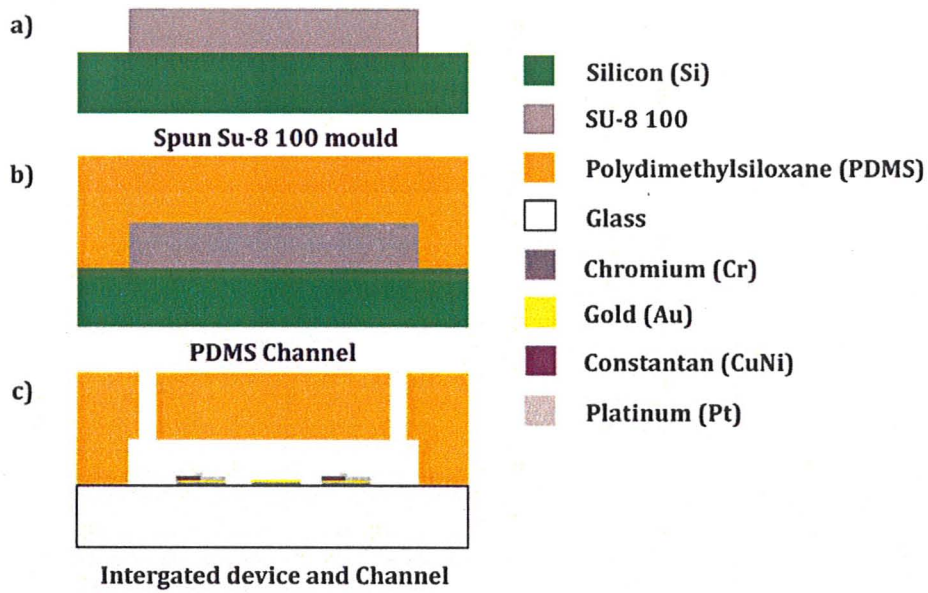


Figure 4-12: Su-8 100 PDMS microchannel fabrication and integration on the time of flight sensor.

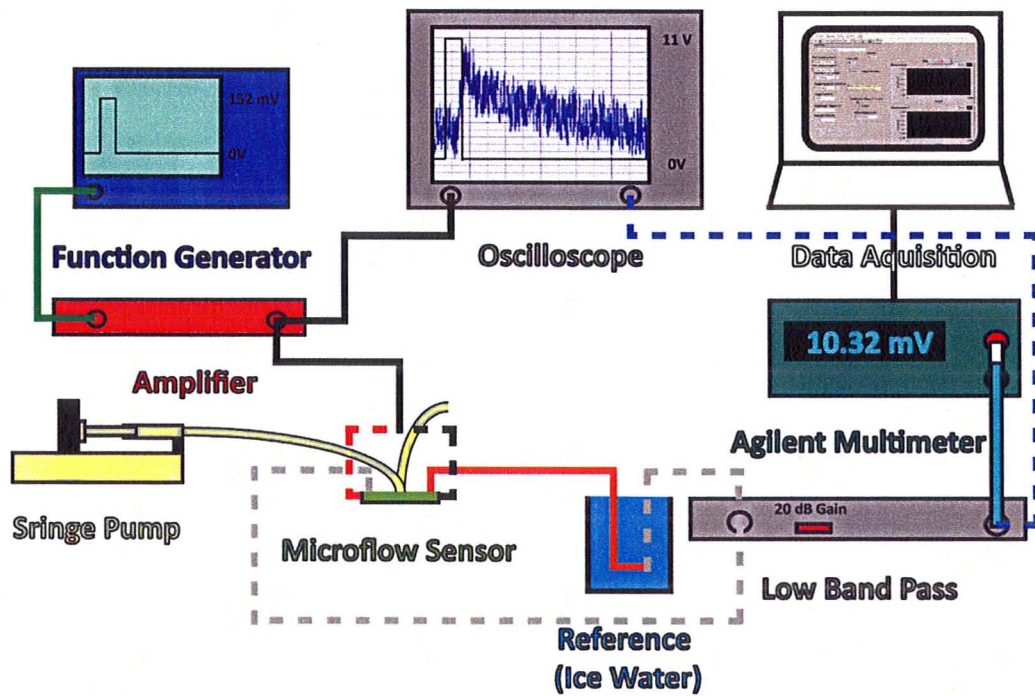


Figure 4-13: Schematic of characterization of micro flow sensor

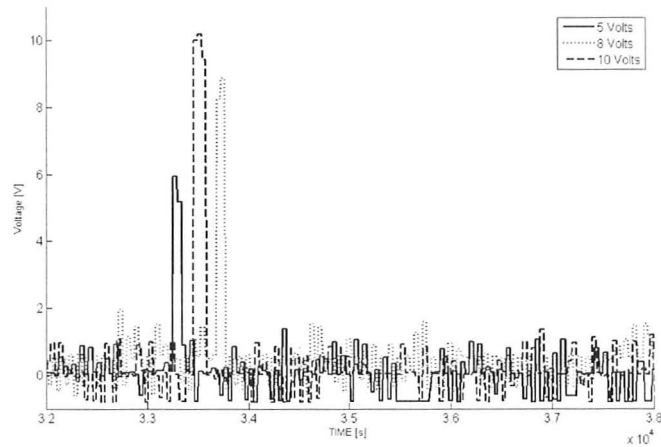


Figure 4-14: Typical voltage signal for the input of the micro heater, for 5, 8 & 10 volts

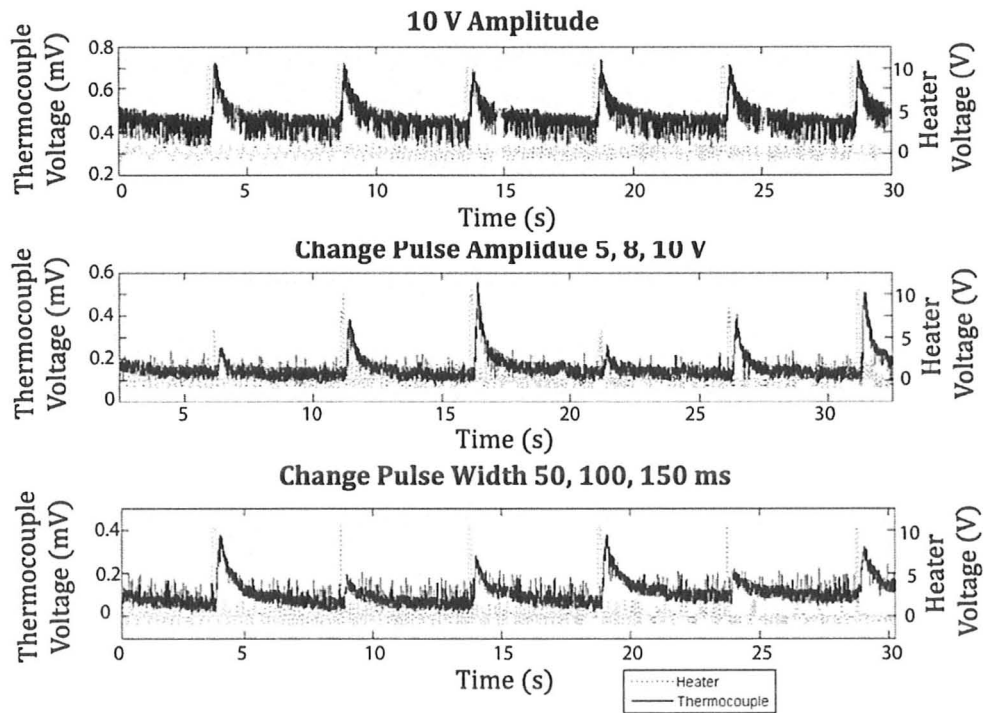


Figure 4-15: Measured voltages for mass flow rate of 0.3 ml/min, a) is single pulse operation at 10 V, b) is multiple pulse operation with changing amplitude 5, 8 and 10V. c) is multiple pulse operation with changing pulse times 50, 100, and 150 ms.

There is considerable noise on both the output signal and the input pulse, as can be seen on all three graphs. To filter the noise, a 3 point running average of the data was considered; however, this introduces both a time and amplitude shift of the pulse, and would affect the accuracy of the results. Ultimately it was decided upon using only the raw data as the peaks were very distinguishable despite the noise, and any effect of smoothing would have adverse effects on accuracy.

4.7 Experimental Results

4.7.1 Introduction

The micro flow sensor was correlated using the experimental setup, (see Figure 4-13) as outlined previously. The initial batch of micro flow sensors were fabricated on silicon dioxide substrates, as at the time of fabrication glass wafers were unavailable. For the silicon dioxide substrate devices, the heat transfer from the pulse micro heater was predominately through the substrate and not the fluid. This meant that the micro thermocouples detected the temperature change of substrate and not of the change in fluid temperature, except at the higher flow rates where there was a combined detection of the forced convection and the conduction through the substrate. Due to time constraints, and in order to prove the concept, it was decided to fabricate an alternative micro-meso device.

The alternative device consisted of the micro heater as described in chapter 3 and a meso T-type thermocouples of wire diameter (Φ 50 μ m) inserted into the PDMS micro channel, (see Figure 4-16). This eliminated the effect of conduction through the substrate on the

thermocouple output as the thermocouple was directly in the fluid flow; however, it required an optical but less accurate method of detecting the distance between the thermocouple and the heater. The following results are from this type of device unless otherwise stated.

4.7.2 Low duty cycle

A low duty cycle of 2.5 % was chosen for the pulsed heater input of between 50 to 150 ms intervals, typically between every 2-4 per second. This was found to minimize the thermally induced effects such as temperature drift on the working fluid properties. This low duty scheme resulted in high sensitivity and repeatability; however, it significantly reduced the response time of the measurements. Cooling the fluid to the surrounding ambient temperature after the heat pulse requires longer time than initial heating of the fluid. Increasing the duty cycle up to 25%, there was a gain in the response time of the flow sensor. However there was an additional slight increase in temperature drift. The maximum temperature of the working fluid was 60 °C, which is at the upper limit of tolerance for electrical cooling applications.

4.7.3 Time of flight

The operation of the micro flow sensor in the time of flight mode was initially examined. As expected, and it is very evident from Figure 4-17, there is a decrease in the maximum amplitude of the voltage signal and an increase in the time shift between the two thermocouple responses as the flow rate is reduced. At these lower flow rates, the detected pulse signal is weaker, increasingly deformed and broadened between the two

thermocouples. The position of the maximum amplitude is only dependent on the flow velocity.

At the lower flow rates, diffusion within the fluid dominates. At flow rates below 0.1 ml/min, the time of flight measurements are less detectable without an increase in the input power. This is not ideal, as in most MEMS devices the aim is to limit the power consumption. Additionally there is the danger of crosstalk of the heating pulse on the thermocouples. In this case, this is rather small and does not affect the measurement due to the fact that considerable time was spent grounding the experimental setup.

A cross correlation of the two signals was considered to determine the time shift between the input heat pulse and the thermocouple output. However it was deemed that the results were too subjective for this to be considered an accurate method of detection due to the experimental equipment. While a time shift was clearly evident through all measurements, no satisfactory correlation could be achieved due to limitations of the data acquisition system and its time stamping.

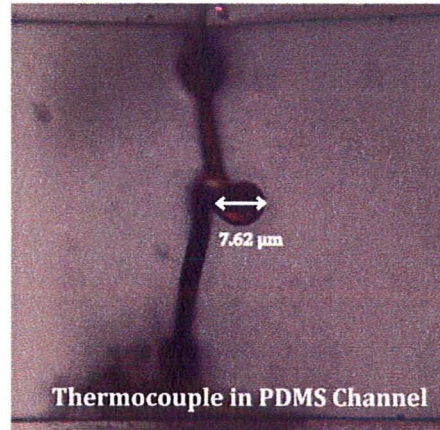


Figure 4-16: T-type thermocouple embedded at the top of the micro channel, its minimal junction size has limited effect on the flow

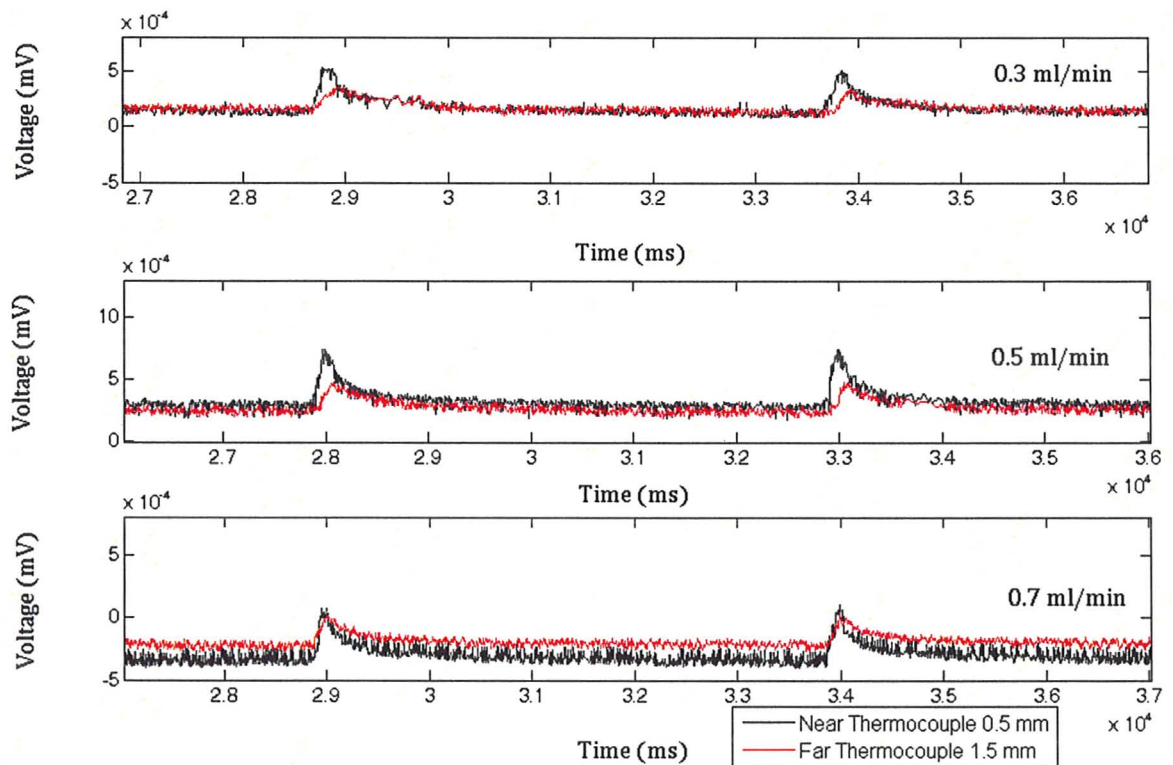


Figure 4-17: Shift of response curve to determine time of flight information. Single pulse regime, with input

10 V , for velocities of $3.33 \times 10^{-2}\text{ m/s}$, $5.56 \times 10^{-2}\text{ m/s}$ and $7.78 \times 10^{-2}\text{ m/s}$.

In the present setup, the time stamping was achieved using labview and a GPIB interface which acquires data from both thermocouples in series. This reduces the sampling frequency and also affects the ordering of the data as both are controlled by labview. Over multiple samples the time shift would be affected considerably by this limitation. The repeatability of this measurement was poor; however, with a simple upgrade of the data acquisition system, reliable time of flight measurements are possible. Upgrading the data acquisition system would involve acquiring a low voltage data acquisition board. This board would be able to acquire thermocouple data directly, eliminating the need for Agilent and GPIB interfacing. This would allow measurement from the thermocouple to be taken in parallel, and speed up the sampling rate. It is possible that at a higher flow rate than 0.7 ml/min the time of flight mode would be a more accurate method of detection and in combination with the calibration method it would increase the dynamic range of the device.

4.7.4 Single pulse operation mode

In the single pulse operation mode, the change in voltage detected by the thermocouple was correlated with the mass flow rate. The calibration principle is that the heat loss from the micro heater source to the fluid will increase with flow rate, thus resulting in a higher output from the downstream thermocouple, see Figure 4-18. The calibration matrix consisted of testing each parameter change three or more times for every flow rate, ranging from no flow up to 0.7 ml/min. The limitation of detectable flow rates in this setup occurred due to failure of PDMS glue seals at the interconnects. At flow rates

higher than 0.7 ml/min the high pressure gradients required to drive the flow resulted in small leakage.

The response of the thermocouple 0.5 mm downstream from the micro heater for 10 V input and period of 4 seconds and duty cycle of 2.5% is shown in Figure 4-16 for different flow rates. Clearly, the thermocouple output signal increases with an increase in the flow rate. At each flow rate three sets of data were taken and averaged. This exercise consisted of averaging approximately 40 to 50 data points. A linear curve was fitted to the data using OriginPro 8 software, see Figure 4-19. The calibration equation with a 10 V micro heater input is

$$V = 0.2377 + 1.8384U \quad 4-19$$

The calibration equation had a standard deviation of 4.9 mV. The calibration equation for the 8 V input was

$$V = 0.1826 + 2.223U \quad 4-20$$

with a standard deviation of 8.34 mV.

The calibration equation for 5 V input flow sensor was

$$V = 0.06167 + 2.186U \quad 4-21$$

with a standard deviation of 8.09 mV.

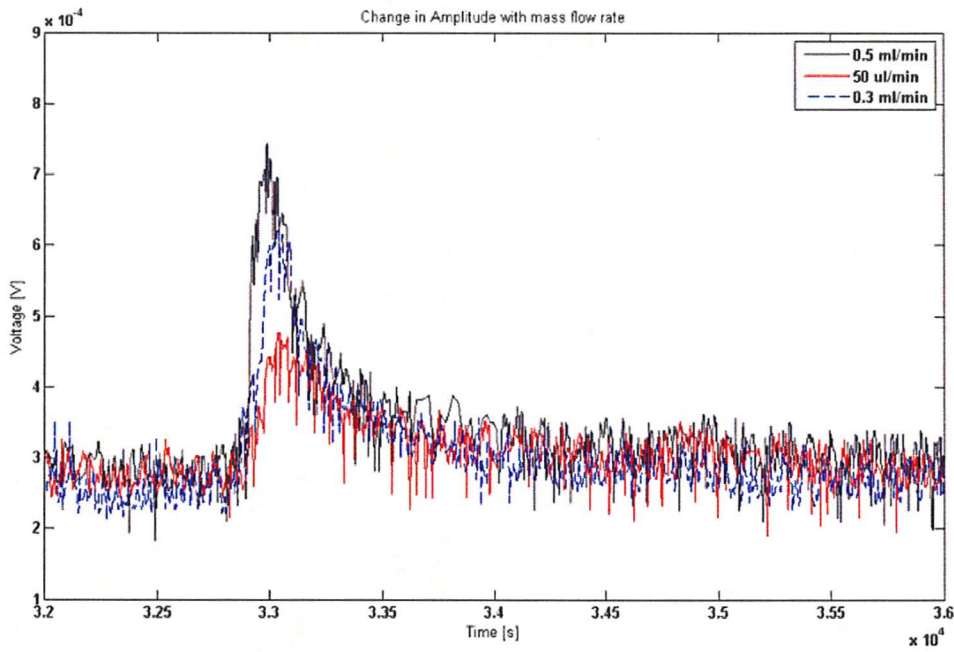


Figure 4-18: The effect of pulse detection with change in flow rates, for an input pulse of 10 V with a duty cycle of 2.5%, period 4 seconds.

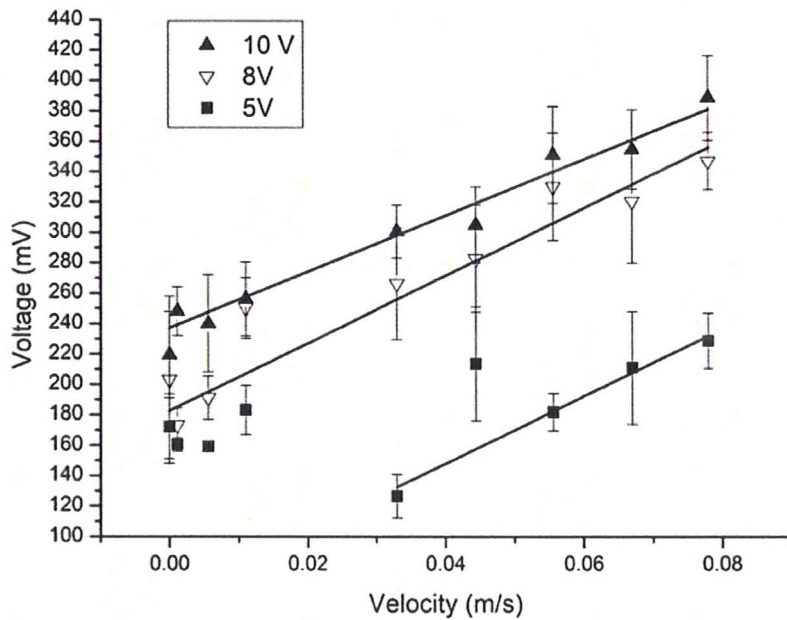


Figure 4-19: Calibration curves for the single pulse mode of the signal amplitude to velocity for different input powers.

At low heater power inputs of 5 V the sensor detection range was 0.1 ml/min to 0.7 ml/min. Below 0.1 ml/min the amplitude was within the noise region of the signal, see Figure 4-18. This made the detection of an individual pulse harder and reduced repeatability.

At 8V input there was a higher dynamic measurement range from 50 μ l/min to 0.7 ml/min. The standard deviation however was 8.36 mV which was higher than that of the 5V input (8.09 mV). This was due to the fact that the calibration was made over a larger range. When the input was increased to 10 V, the dynamic measurement range increased from 10 μ l/min to 0.7 ml/min. Interestingly, the standard deviation decreased to 4.9 mV, meaning that with an increase in voltage input there was an increase in dynamic range and repeatability. The increase in repeatability with increased voltage input was expected. An increase in the micro heater power would produce a stronger heat pulse, resulting in more heat transfer to the fluid and consequently a more detectable temperature rise by the thermocouple.

Figure 4-20 shows that input power to the micro heater does not affect the detection of heat pulse to the thermocouple. The linear relationship between the temperature difference and the mass flow rate holds; however, it does affect the detectability of the signals that are primarily governed by the noise in the system.

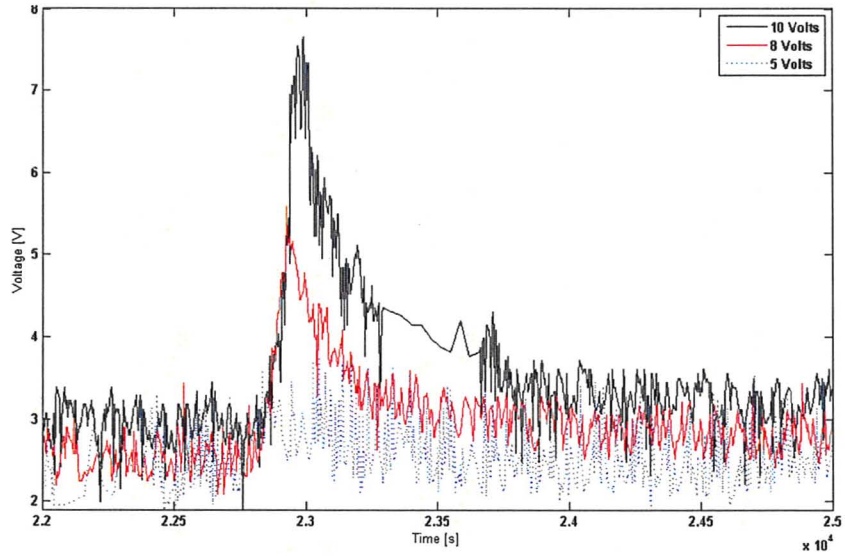


Figure 4-20: Signal response of thermocouple with different voltage inputs, for a flow rate of 0.1 ml/min and duty cycle of 2.5%, period of 4 seconds.

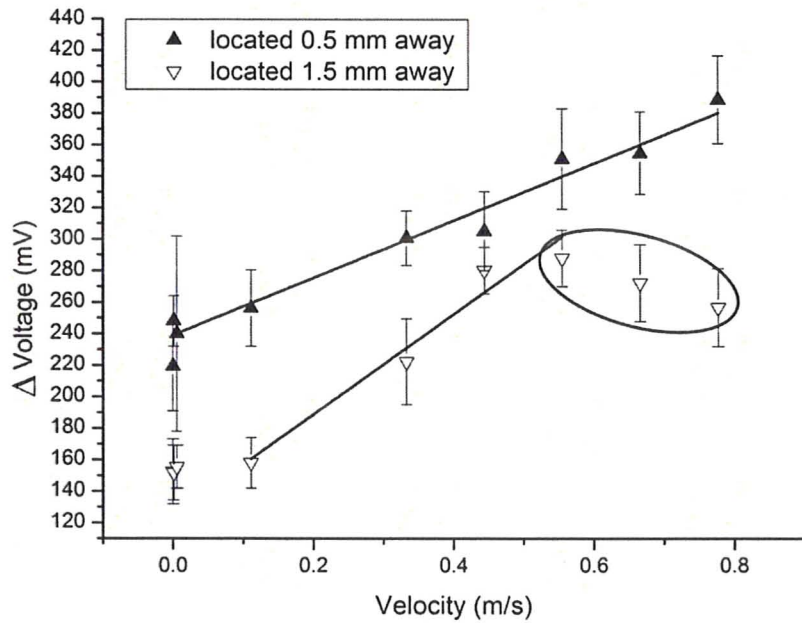


Figure 4-21: Calibration curves for near and far thermocouples for single pulse operation with a 10 V input.

Figure 4-21 consists of the calibration curves for a single pulse mode for inputs of 10 V for both near and far thermocouples. The calibration curves for the thermocouple located 1.5 mm away from the micro heater with a 10 V input is

$$V = 0.12531 + 0.31722U \quad 4-22$$

This calibration equation had a standard deviation of 7.88 mV, and was valid for flow rates in the range 50 μ l/min to 0.5 ml/min. At lower flow rates, the diffusion becomes more significant resulting in a loss of signal at the thermocouple. It was seen that with a small (<1 mm) increase in distance between the heater and the thermocouple, the sensitivity of the flow sensor increased, however with an increased standard deviation from the calibration. This was consistent with Mayer et al. [53] where the distance between the temperature sensor and heater are small.

For example, locating the heater and sensor very close together would result in the temperature difference between heated fluid and surrounding fluid being small. The heated fluid would pass the sensor almost instantly with little or no time for heat transfer losses. Conversely, if they are located too far apart, the sensor will not be able to detect any change in temperature, as the heated fluid would dissipate and diffuse its thermal energy by the time it passes over the sensor. This implies that the sensitivity will increase, reach a maximum, and then decreases again as the distance between the heater and thermocouple is increased. This is inconsistent with the results of Kim, T. H. et al. [32] where the sensitivity decreased with increased distance between temperature and heater,. In their case the heater and sensor where located a large distance away from each other

(5, 10 and 15 mm) and the heated fluid is dissipated and diffused away reducing the sensitivity. They located their sensor a distance greater than 5 mm away from the heater (far from the heater), thereby already operating on the downward edge of the curve. The heat loss from the micro heater to the fluid will increase with flow rate, thereby giving a greater voltage amplitude detection at the thermocouple with increasing flow velocities. The calibration curve with the thermocouple 0.5 mm away from the heater shows this behaviour. However at higher flow rates, for the thermocouple located 1.5 mm away there is a decrease in the signal as the velocity increases. The increase in flow rate increases the diffusion of the heat pulse, resulting in a reduction in the signal strength. This would also occur at the near thermocouple with further increases in flow rate and this shows the upper limitations of the thermotransfer calibration method. It was not possible to further investigate this as the maximum flow rate was 0.7ml/min because of the structural integrity of the microchannel at higher flow rates.

The upper limit of the dynamic range of the device can be increased by reverting to a time of flight measurement once the maximum point of the thermotransfer calibration method is reached and was demonstrated by Ashauer, M. [23].

4.7.5 Change in Pulse Width Operation Mode

The effect of changing the width of the heat pulse on the flow sensor operation was investigated. The response of the thermocouples to a pulse width cycling of 50 ms, 100 ms, and 150 ms is shown in Figure 4-22. It is clear that with an increase in pulse width there is an increase in amplitude of the response voltage from the thermocouple. The

difference in voltage response amplitude was calculated for each pulse, and the change in amplitude plotted against the mass flow rate. A linear slope can be calculated and correlated to the Velocity. The same thermotransfer principle applies as that of the single pulse mode, however a reduction in pulse widths reduces the thermal effect on the ambient fluid, and also the overall power consumption.

In this case, only one of three periods of pulsing is at the full pulse width duration. A sequence of weak, medium and strong pulse is now detected by the sensor. Effectively we have reduced the overall power consumption, which subsequently reduces the overall heat input into the system. This method also allows easier identification between cycles and that should allow for better cross correlation between sets of pulses.

The difference in voltage response with time between the changing pulse widths of 50 ms, 100 ms and 150 ms is shown in Figure 4-22 for different flow rates. Figure 4-23 a) shows the voltage responses of the thermocouple located 0.5 mm away from the heater, while Figure 4-23 b.) shows the response for the thermocouple located 1.5 mm away from the heater. In both cases, with an increase in flow rate, the voltage response of the thermocouple increased with an increase in pulse width. Consequently, the linear slope associated with the change in the pulse width regime increases with the flow rate. This is consistent throughout the data taken; however, in Figure 4-23 a.) for the thermocouple located 0.5 mm away, the first point associated with a 50 ms pulse is higher than that of the next two higher flow rates. This point is erroneous and decreases the slope for this particular flow rate. The reason for this is that at lower pulse widths there is a wider range of error, which is subsequently averaged. In this case, additional data points were

required in order to reduce this error; however, these were not taken at the time of measurement and the facility was reconfigured for another experiment by the time this discrepancy was discovered.

The calibration curves for the change in pulse width operating flow sensor are presented in Figure 4-24. At each flow rate at least three measurements were averaged and fitted with OriginPro8 software. The slopes [α] were derived from the slopes of the voltage difference with time, see Figure 4-23. The calibration equation for the near thermocouple for change in pulse width mode of operation, located 0.5 mm away from heater, was an exponential curve;

$$V = e^{(-36.424 + 2.2901\alpha - 0.0365\alpha^2)} \quad 4-23$$

The calibration curve for the far thermocouple for the change in pulse width mode of operation, located 1.5 mm away from the micro heater was a linear fitted curve. The slope of the calibration curve (sensitivity) was 28.58 $\mu\text{m}/\text{V}$ with a standard deviation of 4.74 $\mu\text{m}/\text{V}$. The calibration equation for the far thermocouple is,

$$V = -0.21564 + 0.02858\alpha \quad 4-24$$

Using the pulse width mode, we have the benefits of reduced thermal interference in the working fluid and lower power consumption.

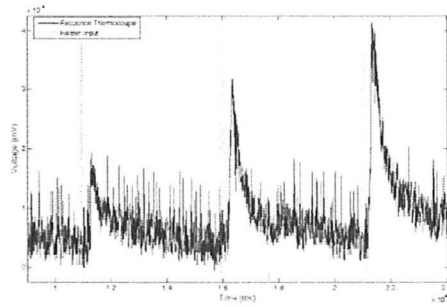


Figure 4-22: Response of the thermocouple to change in pulse width of 50, 100 and 150 ms for a 10 V input at flow rate of 0.5 ml/min.

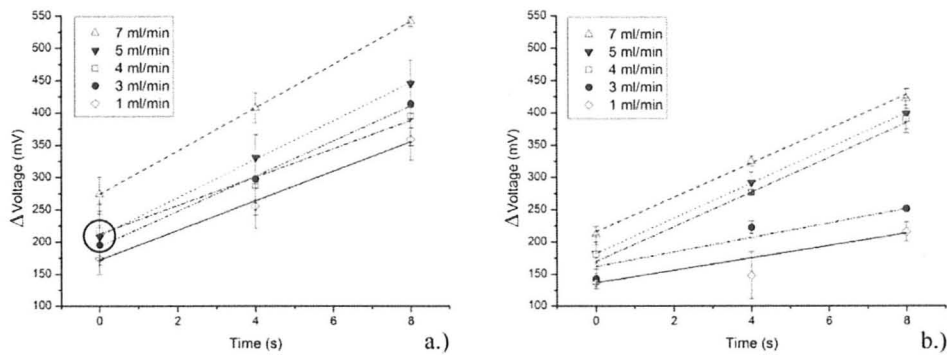


Figure 4-23: The difference in voltage amplitude for change pulse widths with time between pulses a.) thermocouple located 0.5 mm from micro heater, b.) thermocouple located 1.5 mm,

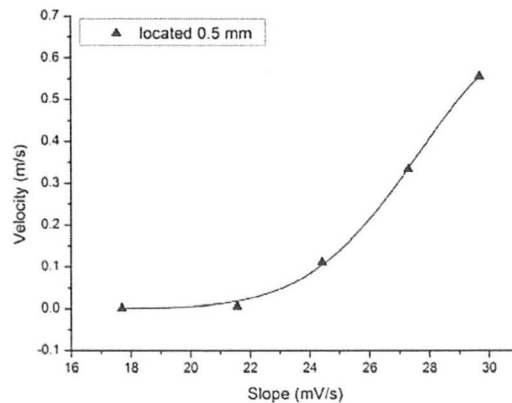


Figure 4-24: Calibration of velocity with slopes of thermocouple response for change in pulse width 50, 100, and 150 ms

4.7.6 Change in pulse amplitude operation mode

The effect of change in amplitude of the heat pulse on the flow sensor operation was investigated. The response of the thermocouples to the cycling of the amplitude of the pulse of 5 V, 8V and 10 V is shown in Figure 4-25.

It is evident that by increasing the pulse amplitude there is an increase in the amplitude of the response voltage from the thermocouple. The difference in voltage response amplitude was calculated for each pulse, and the change in amplitude plotted against the mass flow rate. A linear slope can be calculated and correlated to the mass flow rate. The same thermotransfer principle applies as that of the single pulse mode, however a reduction in pulse amplitude reduces the thermal effect on the ambient fluid, and also the overall power consumption.

A sequence of weak (5V), medium (8V) and strong (10V) pulses are now detected by the sensor. The cycling of the heat pulses makes it is easier to identify (match the pulse amplitude) between cycles and that should allow for better cross correlation between sets of pulses.

The difference in voltage response with time between the changing pulse amplitude of 5V, 8V and 10 V are shown in Figure 4-26 for different flow rates. Figure 4-26 a) is for the voltage responses of the thermocouple located 0.5 mm away from the heaters, while Figure 4-26 b.) is the response for the thermocouple located 1.5 mm away from the heater. In both cases, with an increase in flow rate, the voltage response of the thermocouple increased with an increase in pulse amplitude. Consequently, the linear

slope associated with the change in the pulsed amplitude regime increased with the flow rate. This is consistent throughout the data taken.

The calibration curves for the change in pulse width operating flow sensor are presented in Figure 4-27. At each flow rate measurement at least three measurements were averaged and curve fitted with OriginPro8 software.

The calibration equation for the near thermocouple for change in pulse amplitude mode of operation, located 0.5 mm away from heater, was a parabolic curve

$$V = -1.193 + 0.131\alpha - 0.00216\alpha^2 \quad 4-25$$

where α is the slope. The calibration curve for the far thermocouple for the change in pulse amplitude mode of operation, located 1.5 mm away from the micro heater was a linear fitted curve. The slope of the calibration curve (sensitivity) was $50.83 \mu\text{m}/\text{V}$ with a standard deviation of $8.35 \mu\text{m}/\text{V}$. The calibration equation for the far thermocouple is,

$$V = -0.2899 + 0.0508\alpha \quad 4-26$$

Using the pulse amplitude mode, we have the benefits of reduced thermal interference in the working fluid, more detectable signal than the single pulse mode and pulse duration mode and lower overall power consumption.

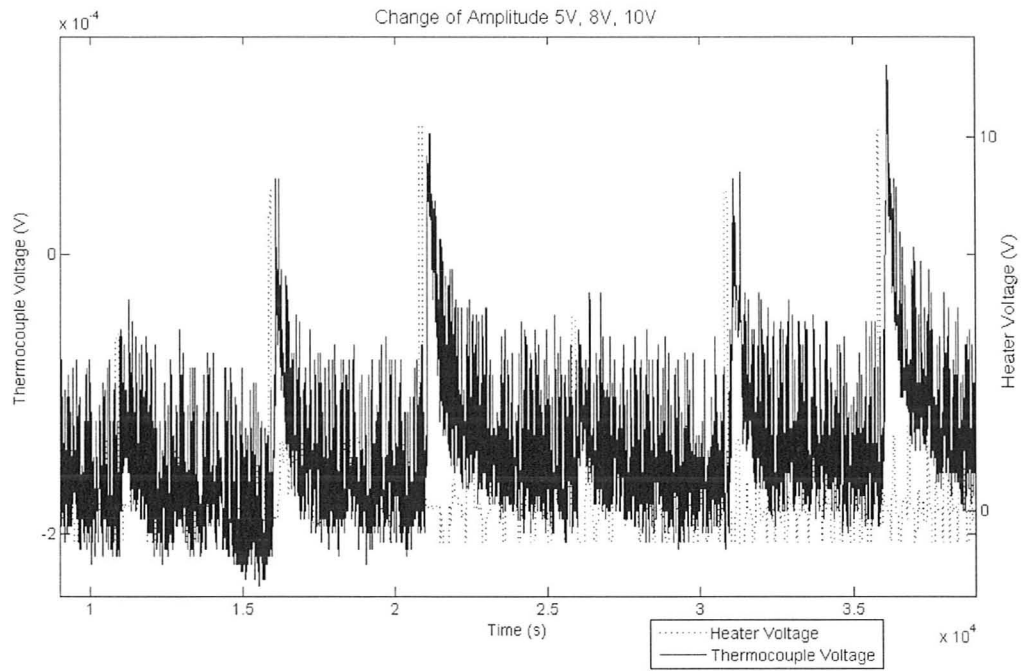


Figure 4-25: Is the response of the thermocouple to change in pulse amplitude 5V, 8V and 10V at flow rate of 0.5 ml/min.

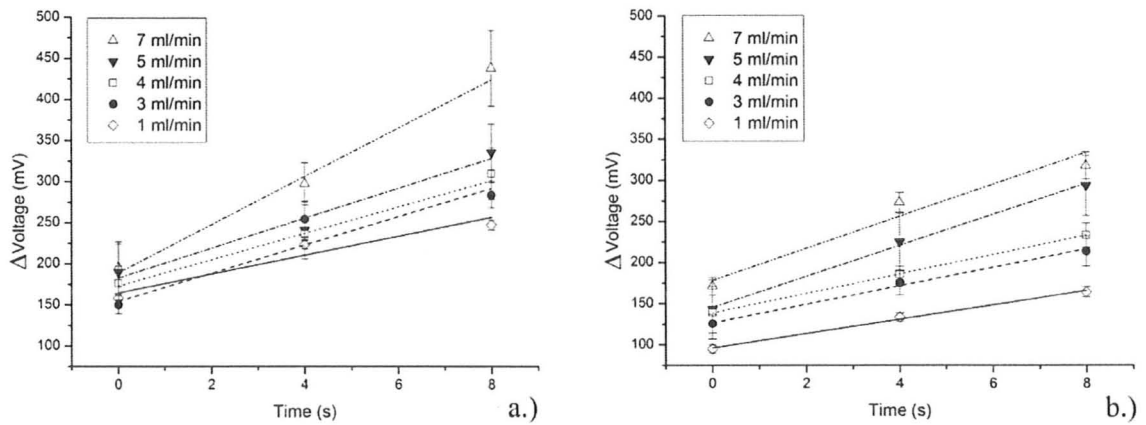


Figure 4-26: The difference in pulse amplitude (5, 8 & 10 V) with time between pulses a.) thermocouple located 0.5 mm from micro heater, b.) thermocouple located 1.5 mm.

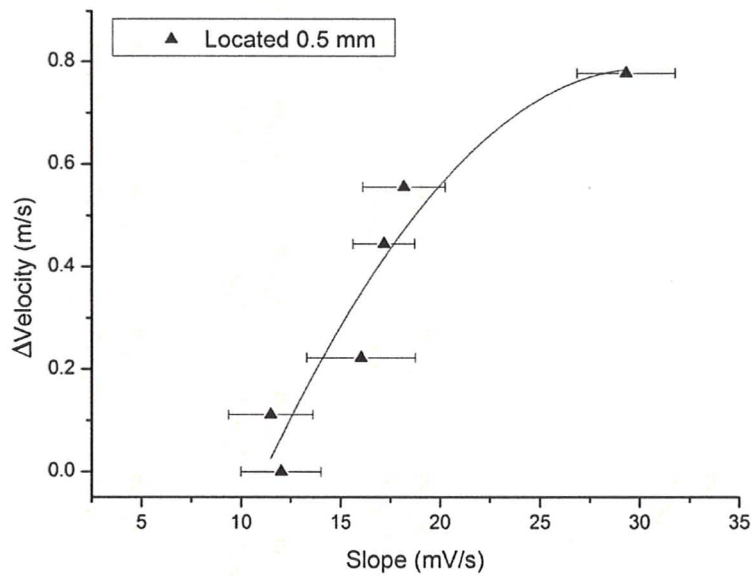


Figure 4-27: Calibration of velocity with slopes of thermocouple response for change in pulse width 50, 100, and 150 ms.

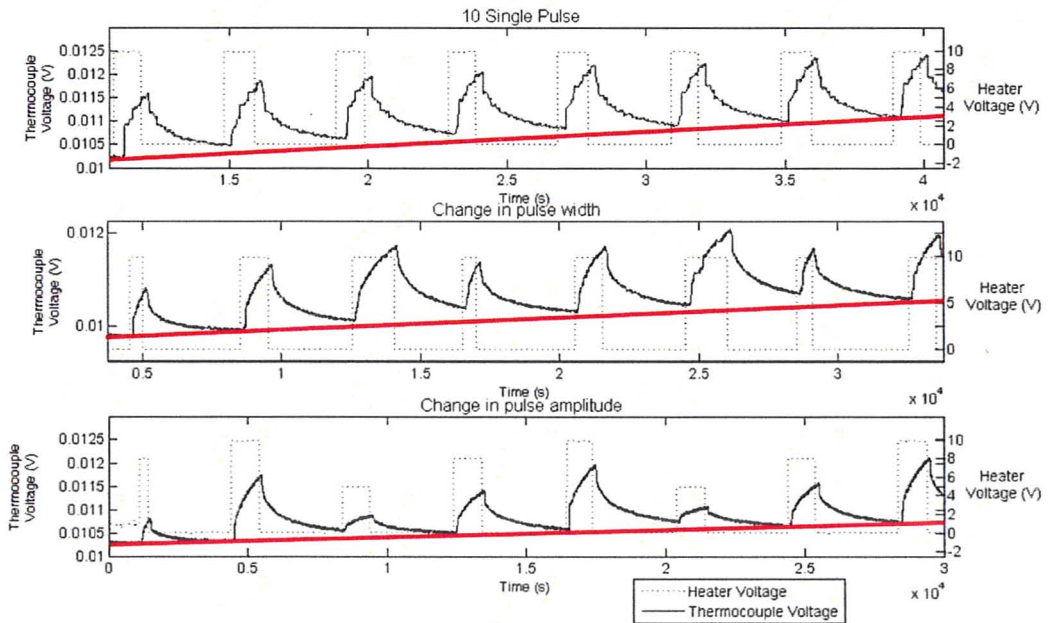


Figure 4-28: Plots of voltage response highlighting the effect of temperature drift for flow rate of 0.5 ml/min, period 4, seconds duty cycle 25%, a.) Single pulse 10 V input b.) Pulse width 10 V 0.5s, 1s and 1.5s c.) Change in amplitude 5 V, 8V and 10V

4.7.7 Temperature Drift

When the heat pulse is introduced into the working fluid, there is transient heating of fluid that is detected by the sensor. At low flow rates, where the forced convection is relatively small, there is a long thermal time constant associated with this. The sensor responds to the heat pulse resulting in a rise to a steady state temperature above the ambient, during the on period of the pulse. This is followed by a more gradual reduction in temperature back towards the ambient when the heater is off. At lower flow rates, the sensor does not reach the full steady state temperature, and consequently will not return to ambient, and there will be a continuous offset/drift by an additional but decreasing temperature/voltage amount.

Figure 4-28 illustrates that by changing the pulsing technique we can significantly reduce the temperature drift. For the single pulse operating mode, at low flow rates a temperature drift can be seen. This is due to the fact that a constant amount of heat is being introduced with each pulse, all of which can not be dissipated in the cool down cycle when the heater off. Using a varying pulse width scheme, the voltage of 10 V is input for different pulse durations. The cycle is much longer between the stronger pulses, (12 second compared to 4 seconds), and thus allows the fluid to equilibrate better resulting in less drift, with the additional benefit of lower overall power consumption. Finally, by using a change in voltage amplitude method, again we have longer periods between the strong (10V) pulses. Starting with a strong 10 V pulse, the response is registered by the thermocouple followed by an 8V impulse and finally by the weaker 5 V pulse. This method reduces further the effect of temperature drift and has significant advantages with power

consumption. At high duty cycles, this pulse technique would be particularly effective at alleviating temperature drift; however, it can not be fully eliminated and will always be present in some manner.

4.7.8 Advantages

The flow sensor was calibrated using the thermotransfer principle for flows up to 0.7 ml/min with a 5% precision, for three different operating modes.

- The main advantage of the proposed solution with respect to more conventional ones is its scalability, as it has a significantly reduced foot print requiring only one temperature sensor, and will result in a greater mechanical simplicity.
- The device requires negligible net heat input. Only a short period of heating time is required until a strong signal has been generated. The power consumption can be further reduced by introducing novel pulsing schemes. This makes the flow sensor particularly applicable to biological applications.
- No time domain information is required once initial calibration is done, with a calibrated operating range below $< 0.7\text{ml/min}$. This is a significant advantage of the thermotransfer method as it reduces the amount of hardware and software required, and would reduce chip real-estate requirements for lab on chip applications. It also makes the post processing rather more simplistic.

- The technique requires an initial complex calibration methodology that if it were required for each individual device thereafter would make this method too cumbersome and cause it to be made redundant. However, due to the batch fabrication method of MEMS devices, one device calibration per batch is all that is required. This makes this calibration method and mode of operation particularly attractive.

4.9 Summary

This chapter presents an overview of the micro flow sensor development and design in this study. Critical design specifications of the fabrication process of both the thermocouple and heater are examined. The rationale behind materials, working fluid, thermocouple design, and fabrication techniques are explained. The developed microfabrication process, along with advantages and limitations of each step of the process discussed. Detailed characterization results of the micro flow sensor are presented.

Chapter 5: Conclusions and Future Works

5.1 Introduction

In this chapter a summary of the conclusions of this study is presented. The key challenges and major benefits of the novel micro pulse flow sensor are reviewed. The key experimental results of the overall device, as well as each of the individual components of the device are summarized. This is followed by some recommendations for future work, which may clarify some of the questions that have arisen from this work.

5.2 Overview and Conclusions

There were three main objectives: (1) the development of the micro thermocouple, (2) the development of the micro heater and (3) the development of the micro flow sensor. In this thesis, micro thermocouples capable of highly precise (0.5 °C) temperature measurements and micro heaters were designed, fabricated and characterized.

Subsequently they were integrated into a micro pulse film sensor within a microchannel.

1. The microfabrication protocols and procedures were developed for the micro thermocouple, micro heater and micro thermal flow sensor. The micro flow sensor was fabricated using a three mask process.
2. Characterization of the constantan (nickel/copper) alloy for the fabrication of thermocouple was one of the main challenges of the fabrication process. The constantan alloy was electroplated using an electroplating solution suggested by

Green, T. K. et al. [19] and investigated by Sartorelli, M.L. et al. [13]. Material nickel composition concentrations were characterized for different reference potentials. With increase in nickel content there was increase in Seebeck coefficient. Typical deposits were smooth and metallic with small granularity. At -1.25 V decline in homogeneity of compensation and grain size, this is where hydrogen evolution occurred, and pin holes were found.

3. Both a compensated and a non compensated micro thermocouple arrangement were fabricated and tested, and as expected the calibration slopes were approximately the same at $39.04 \mu\text{V}/^\circ\text{C}$ and $41.75 \mu\text{V}/^\circ\text{C}$ respectively. However the accuracy of the compensated thermocouple is twice that the non compensated thermocouples due to additional secondary junctions present that was exposed to ambient (room temperature fluctuations $\sim \pm 2^\circ\text{C}$). The non compensated arrangement, notwithstanding the finding above, could be used for measurement where there is less stringent demand for accuracy.
4. There was a high consistency of the micro thermocouple measurements for the same batch, with a standard deviation of $3.34 \mu\text{V}$. This indicates a homogenous constantan film, with the deviations most like due to secondary junctions. This demonstrates that only one thermocouple would be required to be calibrated in a batch of micro thermocouples to have an accurate batch of the thermocouples.
5. The power required for the glass substrate was 46mW, 112mW and 160mW for 5V, 8V, 10V respectively, while for the silicon oxide it was 499.5 mW, 1.27 W and 1.943 W respectively. The significantly higher power consumption for the

silicon oxide substrate was due to the two orders of magnitude higher thermal conductivity of the silicon oxide compared to glass.

The micro flow pulse sensor developed here had good repeatability and had the effect of compensating against temperature drift that has been problematic in previous micro thermal mass flow sensors. The main features of the flow sensor are:

1. The sensor could be operated in three modes: (1) time of flight, (2) temperature difference¹ and (3) pulsed calibration mode. It was the pulse calibration technique that eliminated the interference of input temperature on the working fluid temperature.
2. The flow sensor was tested for three pulse mode configurations; single, multiple pulses with change in input voltage and multiple pulses with change in pulse duration. The results showed that the multiple pulse modes generated a more detectable signal than the single pulse mode and minimized thermal effects on the working fluid.
3. The multiple pulse regimes allowed increasing the devices dynamic flow range. The flow sensor could be replicated easily to be distributed throughout the microchannel so measurements could be made simultaneously at several locations.
4. The microfabrication process developed here was simpler and the sensor had a high response time, and was highly sensitive.

¹ Temperature difference mode was not demonstrate, but it can be catered for under current design

5. The micro flow sensor was tested with a working fluid consisting of a mixture of methanol and water. Experimental data showed promising results with fast and highly sensitive signals for ranges of 0.5 $\mu\text{l}/\text{min}$ to 0.7 ml/min . An operational maximum flow rate of 0.7 ml/min was achieved by the sensor. The device can be operated as a thermotransfer sensor for flow velocities up to 0.5556 m/s with resolution of 1.11×10^{-3} m/s
6. The main advantage of this technique is that following the initial calibration of the devices, there is no requirement for time shift data (each measurement requires a time stamp), and this reduces the amount of post hardware and software required to get tangible results.

5.3 Recommendation

There are a number of items of interest that could be pursued which relate to the present work. The following are recommended for future research:

1. In order to get higher film thickness for higher percentage of the nickel in constantan, a new labview control program should be developed to investigate a pulse electroplating method.
2. Back etching of the silicon dioxide substrate should be investigated to create a thermal bridge for the micro heater, and to see what reduction in power consumption of the micro heater might be achieved.

3. The flow should be measured using a μ PIV system, that is currently available in the lab. This will provide information on the flow field effect after the heat impulse is introduced to the system, and help to optimize the pulsing regimes.
4. Develop an alternative in situ technique to characterize the thermal pulse. One method is to use a temperature-dependent fluorescent dye, where the thermal plume from the heater could be recorded and the flow characteristic of the thermal signal varied using a similar technique that was developed for microfluidics in standard microchannels [53].
5. Update the data acquisition in order to achieve accurate time of flight measurements. Currently the thermocouple sensor responses are being acquired using GPIB-USB-HS which takes two in parallel, with the order set by LabVIEW. Both signals need to be acquired simultaneously and time stamped.
6. The experimental setup for the pulse calibration should be updated in order to reduce the level of noise on the microheater and subsequently on the response of the signal. This requires an alternative amplifier to that used [Harshaw NV-26]. By reducing the noise on the input pulse, the signal will become easier to detect, and subsequently it could require lower power levels to operate, thus improving the overall performance of the device.
7. Investigate the effects of different working fluids, as the sensor response is dependent on the thermal conductivity and on the viscosity of the medium. This would broaden the suitability of the device to different applications.

Reference

- [1] **Gardner, J. W.** 1994, *Microsensors: Principles and Applications*. s.l. : John Wiley & Sons.
- [2] **Van Herwaarden, A.W. Van Duyn, D.C. Van Oudheusden, B.W. Sarro, P.M.** 1989, *Integrated Thermopile Sensors*. Sensors and Actuators A, Vols. A21-A23, pp. 621-630.
- [3] **International, ASTM.** 1993, *Manual on the use of thermocouples in temperature measurement*. Fourth.
- [4] **Martin, Y. Williams, C.C. Wickramasinghe, H. K.** 1986, *Atomic force microscope-force mapping and profiling on a sub 100 Å scale*. Journal of Applied Physics, Vol. 61, s.10, pp. 4724-4729.
- [5] **Shi, L. Majumdar, A.** 2001, *Recent developments in micro and nanoscale thermometry*. Microscale Thermophysical Engineering, Vol. 5, pp. 370-378.
- [6] **Park, J-J. Taya, M.** 2005, *Design of micro-temperature sensor array with thin film thermocouples*. s.l. : ASME, Electronic Packaging, Vol. 127.
- [7] **Jang, S.P. Kim, S.J. Paik, K.W.** 2003 *Experimental investigation of thermal characteristics for a microchannel heat sink subject to an impinging jet, using a micro thermal sensor array*. s.l. : Elsevier, Sensor and Actuators A, Vol. 105, pp. 211-224.

- [8] **Gaulous, H. Louahlia-Gualous, H. Bocus, S.** 2001, *Realization and thermal characterization of thin-film optothermal microsensors*. s.l. : Journal of European Applied Physics, pp. 147-152. Vol. 14.
- [9] **Delatorre, R. G. Sartorelli, M. L. Schervenski, A. Q. Pasa, A. A. Guths, S.** 2003, *Thermoelectric properties of electrodeposited CuNi alloy on Si*. Journal of Applied Physics, Vol. 93.
- [10] **Cygan, A.** 2006, *Modeling and Fabrication of a Microthermocouple array*. Masters theise. Louisiana State : Louisiana State Univeristy.
- [11] **Chu, D. Bilir, T. D. Pease, F. R. W. Goodson, K. E.** 2003, *Thin film nano thermocouple sensors for application in laser and electron beam irradiation*. Boston : Actuators andn Microsystems, The 12th International conference on Solid state sensors. pp. 1112-1115.
- [12] **Zhang, X. Choi, H. Datta, A. Li, X.** 2006, *Design, Fabrication and characteriazation of metal embedded thin film thermcouples with various film thicknesses and junction sizes*. s.l. : Institue of Physics Publishing, 2006, Journal of Micromechanics and Microengineering , Vol. 16, pp. 900-905.
- [13] **Sartorelli, M. L. Schervenski, A. Q. Delatorre, R. G. Klauss, P. Maliska, A. M. Pasa, A. A.** 2001, *Cu-Ni thin film electrodeposited on Si: Composition and Current efficiency*. Physica Status Solidi (a), Vol. 187, pp. 91-95.
- [14] **Plieth, W.** 2008, *Electrochemistry for Materials Science*. 1st Edition.

- [15] **Schlesinger, M. Paunovic, M.** 2000, *Modern Electroplating* . Fourth edition.
s.l. : John Wiley & Sons, Inc.
- [16] **Lowenheim, F A.** 1978, *Electroplating*. [ed.] J Robinson and R Weine. 2. s.l. :
McGraw-Hill, Inc.
- [17] 1998, *The development of a stable citrate electrolyte for the electrodeposition of copper-nickel alloys*. Journal Electrochemical Society , Vol. 145.
- [18] **Qiu, R. Zhang, X. L. Qiao, R. Li, Y. Kim, Y. I. Kang, Y. S.** 2007, *CuNi Dendritic Material: Synthesis, Mechanism Discussion, and Application as Glucose Senesor*, American Chemical Society, Chemical Material, Vol. 19, pp. 4174-4180.
- [19] **Green, T. A. Russell, A. E. Roy, S.** 1998, *The development of a stable citrate eletrolye for the electrodeposition of copper-nickel alloys*. 3, s.l. : Journal of Electrochemical Society , Vol. 145.
- [20] **Rode, S. Henninot, C. Matlosz, M.** 2005, *Complexation Chemistry in Nickel and copper-nickel alloy plating from citrate baths*, The Electrochemical Society, Vol. 152, pp. C248-C254.
- [21] **Lee, A. Y. Falke, W. L. Schwaneke, A. E.** 1979, *Electroplating with Ni-Cu alloy*. US Patent 4167459.
- [22] **Jia, W. Nguyen, T. Gill, J. Nelson, J. S.** 2007 *Characterization of cryogen spray cooling with thin-film thermocouple*. Vancouver, British Columbia, Canada :

ASME-JSME Thermal Engineering Summer Heat Transfer Conference. pp.
HT2007-32222.

- [23] **Herin, P. H. Thery, P.** 1992, *Measurements on the thermoelectric properties of thin layers of two metals in electrical contact*. Measurement Science and Technology, Vol. 3, pp. 495-500.
- [24] **Chung, G. S. and Hong, S. W.** 2000, *Fabrication of Pt thin-film type microheater for thermal microensors and its characteristics*. Journal of the Korean Institute of Electrical and Electronic Material Engineers , Vol. 13.
- [25] **Bársony, I. Ádám, M. Kolev, S. D. Ducso, C. S. Vázsonyi, É. Szabó, I. Van den Berg, A.** 1998, *Fast, efficient bulk micro-machined heater for integrated sensor applications*. Southampton : Proceedings of the 12th European Conference on Solid-State Transducers, Eurosensors XII. Vol. 2, pp. 905-908.
- [26] **Baroncini, M. Placidi, P. Cardinali, G. C. Scorzoni, A.** 2004 *Thermal characterization of a microheater for micromachined gas sensors.*: Elsevier, Seneors and Actuators A, Vol. 115, pp. 8-14.
- [27] **Zhang, K. L. Chou, S. K. Ang, S.S.** 2007, *Fabrication, modeling and testing of a thin film Au/Ti microheater*. Elsevier, International Journal of Thermal Sciences, Vol. 46, pp. 580-588.

- [28] **Chung, G. S.** 2002, *The fabrication of micro-heaters with low power consumption using SOI and Trench Structures*. Metals and Materials International, Vol. 8, pp. 347-351.
- [29] **Tang, Z. Fung, S. K. H. Wong, D. T. W. Chan, P. C. H. Sin, J. K. O. Cheung, P. W.** 1998, *An integrated gas sensor based on tin oxide thin film and improved micro-hotplate*. Sensors and Actuators B Chemical, Vol. 46, pp. 174-179.
- [30] **Tiggelaar, R. M. Loeters, P. W. H. van Male, P. Oosterbroek, R. E. Gardeniers, J. G. E. de Croon, M. H. J. M. Schouten, J. C. Elwenspoek, M. C. van den Berg, A.** 2004, *Thermal and Mechanical analysis of a microheater for high temperature catalytic gas phase reactions*. Sensor and Actuators A, Vol. 112, pp. 267-277.
- [31] **van Putten, A.F.P. Middelhoek, S.** 1974, *Integrated Silicon anemometer*. IEEE, Electron Device Letters, Vol. 10, pp. 425-426.
- [32] **Kim, T. H. Kim, S. J.** 2006, *Development of a micro-thermal flow sensor with thin-film thermocouples*. s.l. : Institute of Physics Publishing, Journal of Micromechanics and Microengineering, Vol. 16, pp. 2502-2508.
- [33] **Weiping, Y. Chong, L. Jianhua, L. Lingzhi, M. Defang, N.** 2005, *Thermal distribution microfluidic sensor based on silicon*, s.l. : Elsevier, Sensors and Actuators B, Vol. 108, pp. 943-946.

- [34] **Rodrigues, R. J. Furlan, R.** 2003, *Design of microsensor for gases and liquids flow measurements*. Elsevier, Microelectronics Journal, Vol. 34, pp. 709-711.
- [35] **Hariadi, I. Trieu, .H-K. Vogt, H.** 2002, *Modelling of Microsystem Flow Sensor based on Thermal Time of Flight Mode*. s.l. : Proceedings of SPIE, Design, Test, Integration, and Packaging of MEMS/MOEMS. Vol. 4755, pp. 83-96.
- [36] **Ashauer, M. Glosch, H. Hedrich, F. Hey, N. Sandmaier, H. Lang, W.** 1999, *Thermal Flow Sensor for Liquids and Gases based on combination of two principles*, Sensors and Actuators, Vol. 73, pp. 7-13.
- [37] **Buchner, R. Rohloff, K. Benecke, W. Lang, W.** 2005, *A High Temperature thermopile fabrication process for thermal flow sensors*. Seoul : Transducers, The 13th International conference on Solid-State Sensors, Actuators and Microsystems. pp. 575-578.
- [38] **Bruschi, P. Navarrini, D. Piotto, M.** 2004, *A flow sensor for liquids based on a single temperature sensor operated in pulsed mode*. Sensors and Actuators A, Vol. 110, pp. 269-275.
- [39] **Okulam, N. Henderson, H. T. Chong, A. H.** 2000, *A pulse mode micromachined flow sensor with temperature drift compensation*. IEEE Transactions on electron devices, Vol. 47, pp. 340-347.
- [40] **Wu, J. Sansen, W.** 2002, *Electrochemical time of flight flow sensor*. Sensors and Actuators, A, Vols. 97-98, pp. 68-74.

- [41] **Poghossian, A. Yoshinobu, T. Schoning, M. J.** 2003, *Flow-velocity Microsensors based on semiconductor Field-effect structures* Journal of Sensors, Vol. 3, pp. 202-212.
- [42] **Harnett, C. K. Mosier, B. P. Caton, P. F. Wiedenman, B. Crocker, R. W.** 2003 *Conductivity Pulse Time-of-flight Flow sensor for sub-microliter/minute flow rates*. California USA : 7th International Conference on Minaturized Chemical and Biochemical Analysis Systems. pp. 139-142.
- [43] **Mosier, B. P. Crocker, R. W. Harnett, C. K.** 2004, *Composition pulse time of flight mass flow sensor*. US Patent 6675660.
- [44] **Szekely, L. Reichert, J. Freitag, R.** 2004, *Non-invasive nano-flow sensor for application in microfluidic systems*. Sensors and Actuators A, Vol. 113, pp. 48-53.
- [45] **Incropera, F.P DeWitt, D.P.** 2002, Introduction to Heat Transfer, Ed. 4
- [46] **Lienhard, J. H.** 2006 *A Heat transfer textbook*. 3rd ed. Cambridge Press
- [47] **McDonald, J. C. Whitesides, G. M.** 2002 *Poly(dimethylsiloxane) as a Material for fabricating microfluidic devices*. American Chemical Society, Accounts of Chemical Research, Vol. 35, pp. 491-499.
- [48] **SUBRAMANI, B. G.** 2008 *Bubble Free electrodes for electroosmotic pumping*. Hamilton, Ontario, Canada : McMaster.

- [49] **Ng, M. K. Gitlin, I. Stroock, A. D. Whitesides, G. M.** 2002, *Components for integrated poly(dimethylsiloxane) microfluidic systems*. *Electrophoresis*, Vol. 23, pp. 3461-3473.
- [50] **Makamba, H. Kim, J. H. Lim, K. Park, N. Hadh, J. H.** 2003, *Surface modification of poly(dimethylsiloxane) microchannels*. *Electrophoresis*, Vol. 24, pp. 3607-3619.
- [51] **Boinovich, L. B. Emelyanenko, A. M.** 2008, *Hydrophobic materials and coatings: principles of design, properties and applications.*: Russian Academy of Sciences and Turpion Ltd, Russian Chemical Reviews, Vol. 77, pp. 583-600.
- [52] **Perry, R. H. Green, D. W.** 1997, *Perry's Chemical Engineers Handbook*. 7th Edition. s.l. : McGraw-Hill.
- [53] **Zangeneh, P.** 2007, *Development of electrohydrodynamic (EHD) liquid micropumps for cooling applications*. [ed.] P Selvaganapathy and C Y Ching. *McMaster University*. [Master Thesis]. Hamilton, Ontario, Canada.
- [54] **Mayer, F. Salis, G. Funk, J. Paul, O. Baltes, H.** 1996 *Scaling of thermal CMOS gas flow microsensors: experiment and simulation*. MEMS pp116 -121.
- [55] **Ross, D. Gaitan, M. Locascio, L. E.** 2001, *Temperature measurement in microfluidic systems using a temperature-dependent fluorescent dye*. *Anal. Chem.*, Vol. 73, pp. 4117-4123.

Appendix A - Manufacturing Process

Micro Pulse Film Fabrication Process

Glass/ Si O₂ Substrate Cleaning

- Rinse with acetone for 15 seconds.
- Rinse with methanol for 15 seconds.
- Rise with de-ionized (DI) water for 5 minutes.
- Dry the sample using compressed nitrogen
- Dehydrate the sample at 110 °C for 2 minutes.

Metal Deposition

- Deposit a 100 Å thick chromium layer.
- Deposit a 900 Å thick gold layer.

Patterning Constantan Mould

- Plasma oxidize the substrate at 80 W for 1 minute.
- Spin AZ 4620 for 30 seconds 3000 rpm ~ thickness 8-9 µm
- Soft Bake @ 100 °C for 4 minutes.
- Expose the substrate using the Mask 1 for 39 seconds at $7.6 \frac{mJ}{cm^2}$
- Develop photoresist in 1:3 AZ400K to DI Water solution for 1 minute 20 seconds.
- Rinse with DI Water for 5 minutes.
- Dry with Compressed nitrogen.
- Dehydrate the sample at 110°C for 2 minutes.

Constantan Electroplating

- Plasma oxidize the sample at 80 W for 5 minutes.
- Mix ingredients presented in Table with DI water for electroplating solution.

- Submerge substrate and a Pt target in the electroplating solution.
- Stir the solution with magnetic stir bar at 500 rpm.
- Heat the solution and adjust the temperature 30 °C.
- Using the DC power supply. Connect cathode (black) to substrate and anode to Pt (Red) target.
- Place the Silver-Silver reference close to the substrates. Set the voltage in order to maintain the Reference voltage at 0.95 V.
- Remove the sample from the solution after 15 minutes.
- Rinse the sample with DI water for 5 minutes
- Rinse the sample with acetone until the photoresist is removed
- Rinse the sample with methanol for 15 seconds.
- Rinse with DI water for 5 minutes.
- Dry the substrate using compressed nitrogen.
- Dehydrate the sample at 110°C for 2 minutes.
- Plasma oxidize the substrate at 80W for 5 minutes in order to completely remove the photoresist residual.

Patterning the Heater

- Spin S 1808 Photoresist for 30 seconds at 3000 rpm.
- Soft bake the sample at 110 °C for 90 seconds.
- Expose the substrate using Mask 2 for 5 seconds at 7.5 mJ/sec.
- Develop photoresist in 1:5 developer 351 to DI Water solution for 25 seconds.
- Rinse with DI water for 5 minutes.
- Dry with compressed nitrogen
- Hard bake the sample at 130 °C for 2 minutes.
- Etch the gold with nickel compatible gold etchant for 10 seconds.
- Etch the chromium with nickel compatible chromium etchant for 2 ¼ minutes

- Rinse with acetone to remove photoresist
- Rinse with methanol for 15 seconds.
- Rinse with DI water for 5 minutes.
- Dehydrate the sample at 110°C for 2 minutes.
- Plasma oxidize the substrate at 80W for 5 minutes in order to completely remove the photoresist residual.

Pt mould Lift Off Process

- Plasma oxidize the substrate at 80 W for 5 minute.
- Spin primer for 30 seconds at 4000 rpm
- Spin S 1808 Photoresist for 30 seconds at 4000 rpm.
- Let sample sit in a dish that is partially covered for 5 minutes.
- Soft bake the sample at 90 °C for 2 minutes.
- Over expose sample using Mask 3 for 5.63 seconds at 7.1 mJ/sec.
- Soak sample in toluene for 6 minutes.
- Blow dry off with nitrogen.
- Over develop photoresist in 1:5 developer 351 to DI Water solution for 90 seconds.
- Rinse with DI water for 5 minutes.
- Dry with compressed nitrogen

Metal Deposition

- Plasma oxidize the substrate at 80 W for 2 minute.
- Deposit a 60 Å thick Cr layer
- Deposit a 1000 Å thick Platinum layer.
- Release upside-down in acetone bath for 15 minutes.
- Rinse with acetone to remove any remaining photoresist
- If photoresist remains place substrate upside in a bath of acetone and place in a ultra sonic cleaner for 1 minutes

- Rinse with acetone to remove any remaining photoresist
- Rinse with methanol for 15 seconds.
- Rinse with DI water for 5 minutes.
- Dehydrate the sample at 100 °C for 2 minutes.
- Dice the sample into individual micro plus sensors.

Microchannel Fabrication

Silicon Substrate Cleaning

- Rinse with acetone for 15 seconds.
- Rinse with methanol for 15 seconds.
- Rise with de-ionized (DI) water for 5 minutes.
- Dry the sample using compressed nitrogen
- Dehydrate the sample at 110 °C for 2 minutes.

Patterning Microchannel Mould

- Plasma oxidize the substrate at 50 W for 1 minute.
- Spin cast SU-8 100 at 3000 rpm for 30 seconds ~ thickness 100 µm
- Soft Bake @ 65 °C for 10 minutes and @ 95 °C for 50 minutes.
- Expose substrate using the microchannel mask for 90 seconds at $7.2 \frac{mJ}{cm^2}$
- Post bake the sample at 65 °C for 1 minutes and at 95 °C for 10 minutes.
- Develop with low heat for 30 minutes in 1:3 SU-8 developer to DI Water solution
- Rinse with DI water for 5 minutes.
- Dry with compressed nitrogen.
- Dehydrate and hard bake the sample at 130°C for 5 minutes.

Casting PDMS micro channel

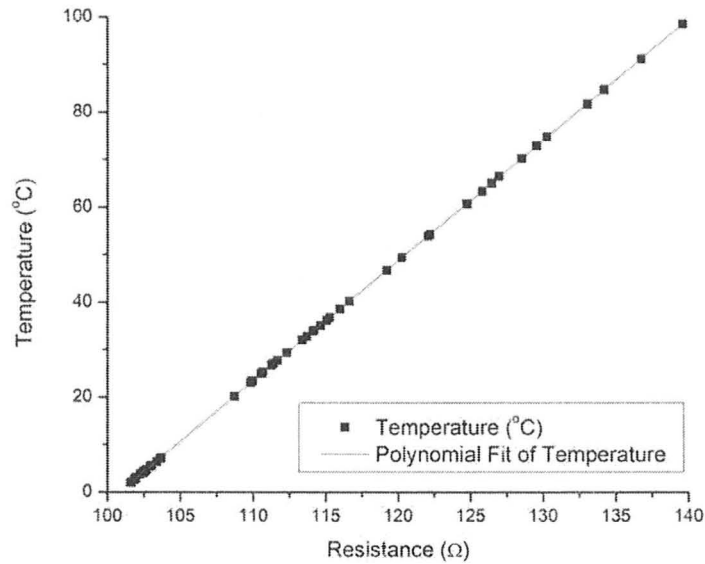
- Mix 10:1 of PDMS to curing agent.
- Degasify the mixture in desiccators for 5 minutes.

- Pour PDMS over microchannel mould and bake it at 65 °C for 60 minutes.
- Peel off PDMS from the silicon substrate
- Cut each microchannel with 2mm rim.
- Punch inlet and outlet using glass micro-pipette

Integrating PDMS microchannel and sensors

- Solder lead wires to the device
- Plasma oxidize the electrode substrate and PDMS microchannel at 50 W for 45 seconds.
- Spin cast 20:1 of PDMS to curing agent at 4000 rpm for 60 seconds.
- Align two macro thermocouples (diameter .003 ") at inlet and outlet.
- Dab PDMS microchannel on spun PDMS glue, be careful not to get glue into channel.
- Align the microchannel on substrate according to thermocouple junctions.
- Mix 20:1 of PDMS with curing agent and apply using a syringe with needle onto the border of PDMS microchannel on glass substrate
- Bake the sample for 3 minutes at 150 °C.
- Plasma oxidize the device and glass tubing at 50 W for 45 seconds.
- Insert glass tubing in inlet and outlet holes.
- Pre-heat the device with glass tubing's on heat plate at 150 °C for 2 minutes.
- Using a syringe with needle pour the PDMS mixture around glass tubing on the PDMS microchannel.
- Bake the sample for 3 minutes at 150 °C

Appendix B – RTD Calibration Curve



Temperature	Resistance	Temperature	Resistance	Temperature	Resistance
°C	Ω	°C	Ω	°C	Ω
2.05	101.606	5.38	102.957	36.20	115.066
2.08	101.615	5.45	102.986	36.76	115.283
2.15	101.657	5.62	103.055	38.57	115.983
2.63	101.851	6.43	103.398	40.21	116.623
2.65	101.858	7.01	103.622	46.74	119.232
2.71	101.881	7.21	103.703	49.40	120.255
2.80	101.918	20.20	108.705	53.93	122.090
2.81	101.924	23.1	109.822	54.28	122.223
2.93	101.972	23.46	109.963	60.68	124.784
3.01	101.976	24.93	110.544	63.40	125.828
3.77	102.267	25.24	110.666	65.07	126.469
4.10	102.443	26.75	111.274	66.46	126.993
4.14	102.464	27.03	111.383	70.23	128.556
4.24	102.501	27.78	111.674	72.91	129.575
4.32	102.534	29.34	112.310	74.83	130.3014
4.39	102.562	32.00	113.388	81.73	133.084
4.52	102.613	32.79	113.695	84.75	134.229
4.66	102.673	33.87	114.112	91.19	136.800
4.69	102.683	34.08	114.195	98.54	139.648
4.74	102.702	35.08	114.636		

Standard deviation of ± 0.05969013 °C

$$y = 54.4567 * 10^{-6}x^3 - 19.8473657 * 10^{-6}x^2 + 4.9304361018x - 351.2264827483$$

Appendix C – Mask Design

